E.O. Paton Electric Welding Institute of the National Academy of Sciences of Ukraine

International Scientific-Technical and Production Journal

The Paton WELDING JOURNAL

Issue
1
2021

Published Monthly Since 2000

English Translation of the Monthly «Avtomatychne Zvaryuvannya»
(Avtomaticheskaya Svarka/Automatic Welding) Journal Published in Ukrainian and Russian Since 1948

Founders
E.O. Paton Electric Welding Institute
International Association «Welding»

Publisher
International Association «Welding»

Translators
A.O. Fomin, I.M. Kutianova
Editor
N.G. Khomenko
Electron galley
D.I. Sereda, T.Yu. Snegiryova

Address
E.O. Paton Electric Welding Institute,
International Association «Welding»
11 Kazymyr Malevych Str. (former Bozhenko),
03150, Kyiv, Ukraine
Tel.:/Fax: (38044) 200 82 77
E-mail: journal@paton.kiev.ua
www://patonpublishinghouse.com/eng/journals/tpwj

State Registration Certificate
KV 4790 of 09.01.2001
ISSN 0957-798X
DOI: http://dx.doi.org/10.37434/tpwj

Subscriptions
12 issues per year, back issues available.
$384, subscriptions for the printed (hard copy) version,
air postage and packaging included.
$312, subscriptions for the electronic version
(sending issues of Journal in pdf format
or providing access to IP addresses).
Institutions with current subscriptions on printed version
can purchase online access to the electronic versions
of any back issues that they have not subscribed to.
Issues of the Journal (more than two years old)
are available at a substantially reduced price.

CONTENT

Plenary reports of the X International Conference «Mathematical Modelling and Information Technologies in Welding and Related Processes»[*]

Odesa, September 14–18, 2020

---

[*] Archive of Conference Proceedings: https://patonpublishinghouse.com/eng/proceedings/mmw

https://doi.org/10.37434/tpwj2021.01.01

PREDICTION OF THE KINETICS OF TEMPERATURE FIELDS AND STRESS-STRAIN STATE OF DISSIMILAR PRODUCTS, MANUFACTURED BY LAYER-BY-LAYER FORMING

O.V. Makhnenko, O.S. Milenin, O.A. Velykoivanenko,
G.P. Rozynka, S.S. Kozlitina, N.I. Pivtorak and **L.I. Dzyubak**
E.O. Paton Electric Welding Institute of the NAS of Ukraine
11 Kazymyr Malevych Str., 03150, Kyiv, Ukraine. E-mail: office@paton.kiev.ua

Layer-by-layer forming of metal structures and elements of various-purpose mechanisms is a promising venue of high technology advance. Broad possibilities for optimization of technology parameters and accuracy of positioning the forming layers allow manufacturing thin-wall products of different geometry. Moreover, dissimilar structures can be produced by changing the filler material. Such a technological process requires thorough optimization of the respective technology cycle to guarantee the required quality of the dissimilar structure, depending on product shape, materials and features of a specific technology. This work is a study of the features of the kinetics of temperature field and stress-strain state of dissimilar structures during multilayer surfacing in the case of T-beam structures, made by xBeam 3D Metal Printer technology. 12 Ref., 6 Figures.

Keywords: layer-by-layer forming, dissimilar structure, temperature field, stress-strain state, mathematical modeling

One of the venues for application of modern technologies of layer-by-layer forming is realization of industrial systems of manufacturing dissimilar structural elements and parts of mechanisms. This allows producing complex-shaped structural elements with minimum metal consumption, compared to classical approaches of milling or welding, that causes interest in such technologies in aerospace and power sectors, instrument making, medicine, etc. [1–3]. As regards critical structures from light metals and alloys, for which the key design aspect is minimizing the weight at preservation of the required service properties (strength, corrosion resistance, rigidity, etc.), a rational method is combining different materials by permanent joining of dissimilar parts. It is known that producing dissimilar joints by fusion welding is limited for a large number of metal pairs for the reason of their low mutual solubility and proneness to formation of intermetallic inclusions and respective lowering of structure performance [4, 5]. Therefore, the methods of solid-phase welding, braze-welding, welding through interlayers, etc. are used for dissimilar material joining. One of the required measures at implementation of the respective technology is optimization of technology parameters, in particular based on the results of mathematical and computer modeling of physico-mechanical processes that determine the final product quality.

Manufacturing dissimilar metal structures by the methods of layer-by-layer forming is associated with the same basic technology problems, as fusion welding. However, slight overheating of metal at surfacing, and possibility of technology parameters optimization, allow implementation of the technological schematics of manufacturing sound dissimilar products. For this purpose, it is necessary to take into account the features of temperature field kinetics at layer deposition, as well as the residual stress-strain state (SSS) of the structure.

The objective of this study is numerical analysis of the characteristic features of the kinetics of the fields of temperatures, stresses and strains in dissimilar structures at their layer-by-layer forming for the case of a typical beam-shaped structural element.

Typical problems of technology parameters optimization at layer-by-layer forming of dissimilar structural elements. Depending on specific types of metals, fundamentally different approaches can be realized in the structural element, as regards achieving sound fusion of the layers in the area of dissimilar contact. In the case of continuous mutual solubility of metals, optimization of heat input parameters at forming layer deposition is determined by the same requirements for similar and dissimilar parts of the structures, namely the need for activation of the solid surface of the previous layer at simultaneous prevention of liquid metal overheating. In the previous studies, the authors showed that a rational method for temperature field optimization in such a case is appropriate selection of the delay time between deposition of the forming layers that allows removing excess heat into the substrate or the environment [6, 7].

O.V. Makhnenko — https://orcid.org/0000-0002-8583-0163, O.S. Milenin — https://orcid.org/0000-0002-9465-7710

If a metal pair is characterized by limited mutual solubility, and their melting temperatures differ significantly, fusion of the dissimilar layers can be realized by braze-welding scheme [8]. The essence of this method consists in that under the impact of the heat source the metal with a higher melting temperature remains solid, while the metal with a lower melting temperature stays in the liquid state for some time, forming braze-welding contact. It allows lowering the maximum temperatures of heating of the contact surface of liquid and solid metals, thus reducing the risk of formation of intermetallic inclusions. Formally, the requirements to temperature field optimization in the dissimilar material contact are described by temperature-time dependencies of the latent period of intermetallic formation.

It is known that, in the case of a significant difference of the coefficients of linear thermal expansion, the residual SSS for dissimilar structures is characterized by stress concentration in the area of dissimilar material contact. Such a feature of the residual state should be expected for structural elements, manufactured by the methods of layer-by-layer forming. In view of the fact that higher stresses negatively affect the performance, the influence of manufacturing technology factor on residual SSS and methods for possible lowering of stress concentration in the area of the dissimilar joint should be determined.

Mathematical model of the kinetics of temperature field and stress-strain state at layer-by-layer forming of dissimilar beam structures. The first stage of investigation of the kinetics of the above-mentioned product state during layer-by-layer forming is prediction of temperature field development. The temperature field kinetics is determined by conductive propagation processes, for which the connection between moment of time t and temperature field $T = T(x, y, z)$ is described by 3D equation of heat conductivity:

$$\begin{gathered} c\rho(x,y,z,T)\frac{\partial T(x,y,z)}{\partial t} = \\ = \nabla\left[\lambda(x,y,z,T)\nabla T(x,y,z)\right], \end{gathered} \tag{1}$$

where λ, $c\rho$ are the heat conductivity and volume heat capacity of the structure material in the Cartesian system of coordinates (x, y, z), respectively.

Heat source in the considered case is the electron beam with thermal power q_I, and energy distribution in the heated spot can be described by a normal law. Heat sink from the considered structure surface occurs through radiant heat transfer and heat removal into the technological fixtures. Accordingly, the flow of radiant energy from item surface q_R depends on surface and ambient temperature, as well as reflective properties of the surface, and it can be quantitatively described by Stephan–Boltzmann law:

$$q_R = \varepsilon\sigma_{SB}\left(T^4 - T_C^4\right), \tag{2}$$

where ε is the degree of blackness of the radiating surface, $\sigma_{SB} = 5.67\cdot10^{-8}$ J·s^{-1}·m^{-2}·°C^{-4} is the Stephan-Boltzmann constant.

The thermal energy flow into the load-carrying fixture q_N is described by the Newton law in the following form:

$$q_N = \alpha_T\left(T - T_C\right), \tag{3}$$

α_T is the coefficient of surface heat removal.

Proceeding from the conditions of heat balance, the heat flow to the surface of nonuniformly heated body due to the processes of conductive heat conductivity, is equal to heat sink from the surface that allows formulating the boundary conditions for the problem (1):

$$\lambda(T)\frac{\partial T}{\partial \boldsymbol{n}} + q_I + q_R + q_N = 0, \tag{4}$$

where $\boldsymbol{n}$ is the normal to the surface of the considered area of the structure.

Considering (2)–(3), the boundary condition for equation (1) has the following form:

$$-\lambda(T)\frac{\partial T}{\partial \boldsymbol{n}} = -q_I + \alpha_T\left(T - T_C\right) + \varepsilon\sigma_{SB}\left(T^4 - T_C^4\right). \tag{5}$$

The process of melting and further solidification of metal in welding is accompanied by absorption and evolution of heat of phase transition of the first kind g_{ft}, respectively. This phenomenon occurs in a rather narrow range of metal temperatures, namely its solid-liquid state between the temperatures of liquidus T_L and solidus T_S that complicates mathematical description of the heat balance. In order to take into account the evolution/absorption of the latent heat of phase transition, the effective heat capacity of the material in $T_S - T_L$ temperature range was used in the following form:

$$c\rho(T) = \begin{cases} c\rho\left(T_S\right) + \dfrac{g_{ft}}{T_L - T_S}, T_S < T < T_L \\ c\rho\left(T_L\right), T \ge T_L \end{cases}. \tag{6}$$

In the liquid metal pool the features of heat transfer are due mainly to the processes of convective stirring, which are determined by hydrodynamics of the nonuniformly heated melt. In this work intensification of heat transfer in the liquid metal as a result of convective stirring was taken into account by increasing the coefficient of heat conductivity:

$$\lambda(T) = \begin{cases} \lambda(T), T_S < T < T_L; \\ \lambda\left(T_L\right)n_K, T \ge T_L, \end{cases} \tag{7}$$

where $n_K = 3–5$ is the coefficient that allows for the convective heat transfer in the weld pool liquid metal.

Mathematical consideration of the joint problem of the temperature field kinetics and SSS development is based on finite-element description, using eight-node finite elements (FE). Increment of strain tensor was represented as follows [9]:

$$d\varepsilon_{ij} = d\varepsilon^e_{ij} + d\varepsilon^p_{ij} + \delta_{ij} d\varepsilon_T, \tag{8}$$

where $d\varepsilon^e_{ij}$, $d\varepsilon^p_{ij}$, $\delta_{ij} d\varepsilon_T$ are the components of tensor increment due to elastic deformation mechanism, instantaneous plasticity deformations, and kinetics of a non-uniform temperature field, respectively, $i, j = (x, y, z)$.

Tensors of mechanical stresses σ_{ij} and elastic strains $d\varepsilon^p_{ij}$ are interrelated by the generalized Hooke's law, i.e.

$$\varepsilon^e_{ij} = \frac{\sigma_{ij} - \delta_{ij}\sigma}{2G} + \delta_{ij}(K\sigma + \varphi), \tag{9}$$

where σ is the mean value of the normal components of stress tensor σ_{ij}, i.e. $\sigma = \sigma_{ii}/3$, $K = (1 - 2\nu)/E$ is the bulk modulus.

Increment of instantaneous plasticity deformations $d\varepsilon^p_{ij}$ from the stressed state in a certain FE can be calculated using linear dependence of scalar function Λ and deviator component of the stress tensor as follows:

$$d\varepsilon^p_{ij} = d\Lambda(\sigma_{ij} - \delta_{ij}\sigma). \tag{10}$$

The specific value of function Λ depends on the stressed state in the considered area of the structure, as well as on the shape of material yield surface. Proceeding from the above, the increments of the strain tensor can be represented in the form of superposition of the increment of the respective components [10]:

$$\Delta\varepsilon_{ij} = \Psi\left(\sigma_{ij} - \delta_{ij}\sigma\right) + \delta_{ij}\left(K\sigma + \Delta\varepsilon_T\right) - \\ - \frac{1}{2G}\left(\sigma_{ij} - \delta_{ij}\sigma\right)^* - \left(K\sigma\right)^*, \tag{11}$$

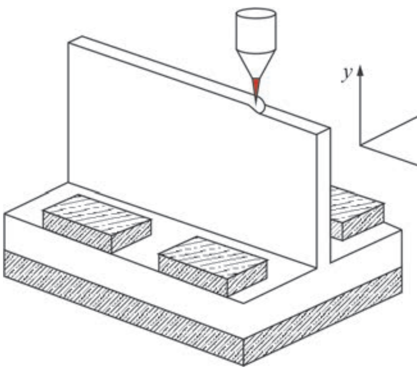

Figure 1. Scheme of layer-by layer forming of a T-beam structure using xBeam 3D metal printer technology

where symbol «*» refers the variable to the previous tracing step; Ψ is the function of material state that determines the condition of plastic flow, in keeping with Mises criterion:

$$\begin{gathered} \Psi = \frac{1}{2G}, \text{ if } \sigma_i < \sigma_T, \\ \Psi > \frac{1}{2G}, \text{ if } \sigma_i = \sigma_T, \\ \text{state } \sigma_i > \sigma_T \text{ invalid.} \end{gathered} \tag{12}$$

Function Ψ is determined by iteration at each step of numerical tracing within the boundary problem of nonstationary thermoplasticity that allows solving the nonlinearity problem in plastic flow of the material.

The proposed approaches were implemented in software, using highly efficient algorithms for parallel solving of the boundary problem of nonstationary thermoplasticity [11]. It allowed conducting the respective studies of the influence of technology parameters of layer-by-layer forming on the current and residual states of various T-beam structures.

Results and their discussion. A complex of studies in the context of the above problems was conducted for the case of layer-by-layer forming of T-beam structure, using xBeam 3D Printer technology (Figure 1) from the following combinations of alloys: similar structure from titanium alloy VT6; dissimilar structure from titanium alloys VT6 and VT1; dissimilar structure from titanium alloy VT6 and commercially pure aluminium. It should be noted that both the similar structure (VT6), and dissimilar titanium structure (VT6–VT1) have no features of layer fusion caused by metallurgical incompatibility so that a common criterion can be used for temperature field optimization. Simultaneous fulfillment of the following conditions was selected as such a criterion [6]:

- absence of previous bead remelting;
- ensuring inter-bead fusion.

Thus, on the base of numerical study of the temperature field kinetics it is necessary to determine the optimum time intervals between deposition of dissimilar structure beads *dt* that allow satisfying the above conditions and producing sound fusion of the layers, depending on their ordinal number *N*.

For a dissimilar titanium-aluminium structure (VT6–Al), direct application of the above criterion will not guarantee producing a sound product that is related to limited solubility of aluminium in titanium. Therefore, at deposition of an aluminium bead on titanium it is necessary to prevent mixing of their liquid phases. It is known, however, that titanium alloy VT6 has a considerably higher melting temperature than aluminium (1640 °C, compared to 660 °C) that allows application of braze-welding principle for joining them. As was noted above, here a short time of contact with liquid al-

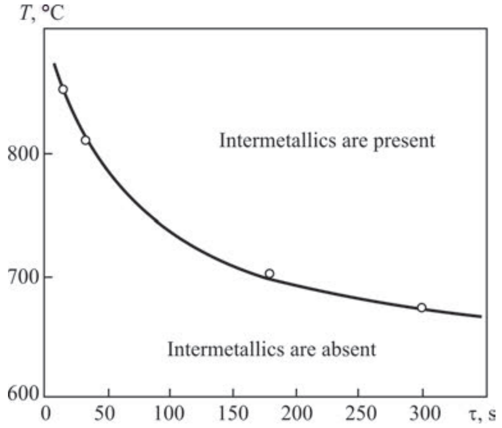

Figure 2. Temperature dependence of the duration of latent period of intermetallic formation at surface contact of titanium and aluminium [12]

uminium should be guaranteed, which depends on contact surface temperature that is related to the presence of the so-called latent period of intermetallic formation [12], the temperature dependence of which is given in Figure 2. Therefore, in addition to the conditions of optimization of the temperature field of the similar part of the structure at contact of dissimilar beads it is necessary to take into account the time of molten aluminium contact with solid titanium.

As shown by calculation results, at layer-by-layer forming of dissimilar beam structure from titanium alloys VT6 and VT1, the relatively small difference in physical properties of these materials and continuous solubility result in the presence of the dissimilar transition only slightly influencing the structure state. So, dependence of optimum time interval of delay between layer deposition *dt* that ensures sufficient dissipation of excess thermal energy in the item, practically does not change its nature after the 20th bead, when material change occurs (Figure 3, *a*)

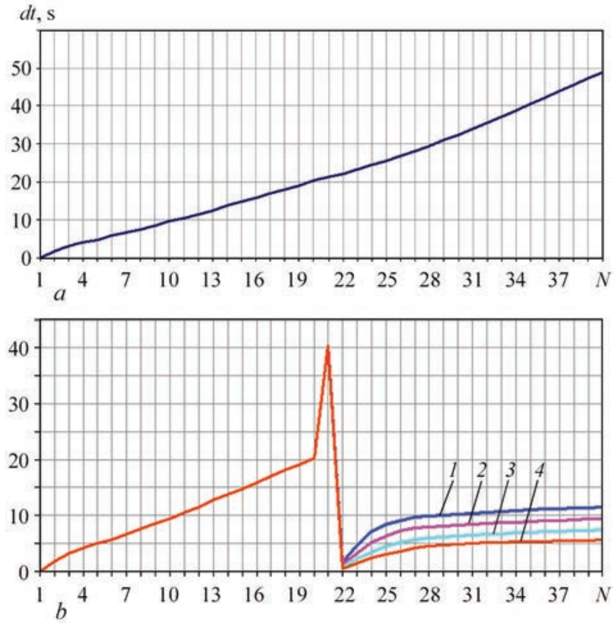

Figure 3. Dependence of time intervals between deposition of dissimilar structure beads *dt*, that allows obtaining sound fusion of the layers, from the bead ordinal number *N*: *a* — VT6 — VT1; *b* — VT6 — Al (*1* — *q*; *2* — 0,9 *q* ; *3* — 0,8 *q*; *4* — 0,7 *q*)

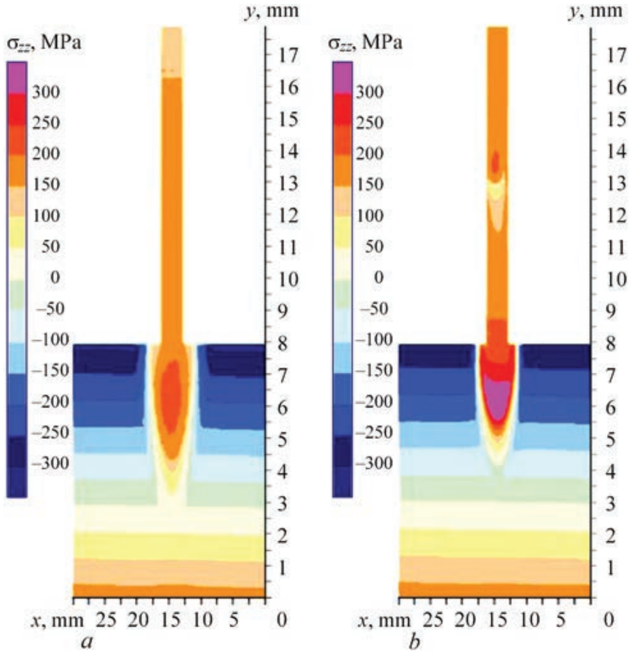

Figure 4. Field of residual stresses σ_{zz} in the cross-sections of a similar (VT6) (*a*) and dissimilar structures (VT6–Al) (*b*)

In the case of a significant difference in physico-mechanical properties of the materials, as is the case in VT6–Al pair, transition to another material (in this case, from titanium alloy to aluminium) requires considerable changes of heat input parameters and delay interval *dt*. So, transition from titanium layer deposition to the aluminium part of the item should be accompanied by a certain cooling of the titanium part with the purpose of lowering the surface temperature

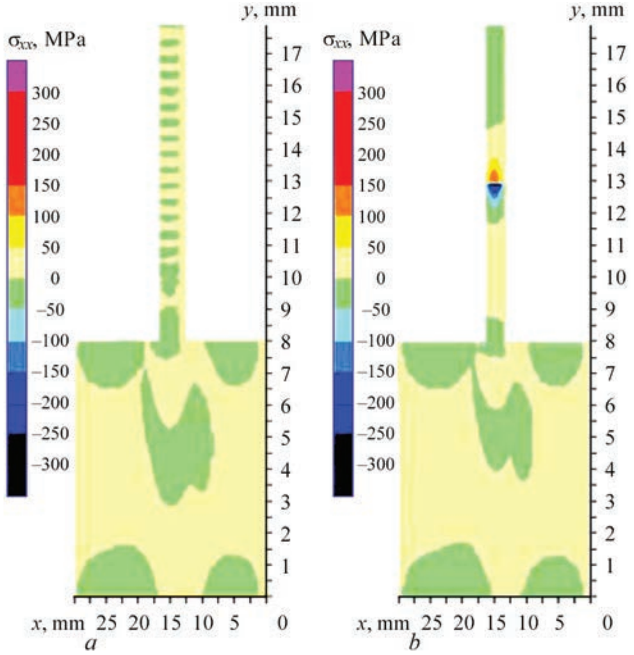

Figure 5. Field of residual stresses σ_{xx} in the cross-sections of a similar (VT6) (*a*) and dissimilar structures (VT6–Al) (*b*)

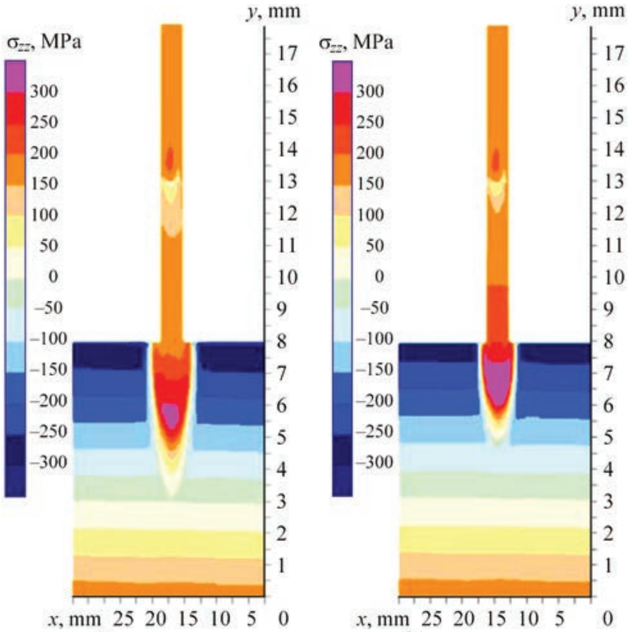

a *b*

Figure 6. Impact of heat input q_1 on the field of residual longitudinal stresses σ_{zz} in the cross-section of a dissimilar (VT6–Al) structure: *a* — 5; *b* — 4 kW

before deposition of a lower melting metal (Figure 3, *b*). Further deposition occurs by the modes characteristic for aluminium structure fabrication.

The difference between mechanical properties of titanium and aluminium results in formation of local stress concentrations. As shown by numerical modeling results, the most marked stress increase in the area of the dissimilar joint occurs in the longitudinal direction (σ_{zz} stresses, Figure 4), as well as in the transverse direction (σ_{xx}, Figure 5). Moreover, the nonuniformity of cooling by the surfaced structure height, caused by the need to stop the process at transition from the titanium to the aluminium part, leads to σ_{zz} increase in the substrate area, compared to the similar structure. Here, the change of heat input power only slightly affects the stress raiser in the dissimilar transition area, but it allows redistributing the residual stresses to certain extent in the area of tee flange transition to the web (Figure 6).

Conclusions

1. A package of mathematical models and computer programs was developed for numerical prediction of the temperature field kinetics and stress-strain state of typical structural elements during layer-by-layer forming by xBeam 3D Printer technology.

2. Criteria of selection of the optimum time between deposition of the forming beads are proposed. For dissimilar contact of metals with an essential difference in the melting temperatures, the temperature mode should ensure the condition of non-melting of the refractory part of the structure by braze-welding principle.

3. The features of residual fields of stresses and strains in the cross-section of a dissimilar structure (VT6-Al), compared to similar structure (VT6), were studied in the case of layer-by-layer forming of T-beam structures by xBeam 3D Printer technology. It is shown that presence of a dissimilar transition and the need for a significant cooling of the last titanium bead before aluminium bead deposition determines formation of a local stress raiser (of longitudinal and transverse stresses). Here, the change of the heat source power has an only slight impact on maximum stresses in the area of the dissimilar transition, largely determining the local stress-strain state in the area of tee flange transition to the web.

1. Wang, Y., Zhou, Y., Lin, et al. (2020) Overview of 3D additive manufacturing (AM) and corresponding AM composites. Composites Pt A. *Applied Science and Manufacturing*, **139**, 106–114, https://doi.org/10.1016/j.compositesa.2020.106114
2. Ryan, K.R., Down, M.P., Banks, C.E. (2021) Future of additive manufacturing: Overview of 4D and 3D printed smart and advanced materials and their applications. *Chemical Engineering J.*, **403**, 126–162, https://doi.org/10.1016/j.cej.2020.126162
3. Ngo, T.D., Kashani, A., Imbalzano, G. et al. (2018) Additive manufacturing (3D printing): A review of materials, methods, applications and challenges. Composites Pt B. *Engineering*, **143**, 172–196, https://doi.org/10.1016/j.compositesb.2018.02.012
4. Dak, G., Pandey, C. (2020) A critical review on dissimilar welds joint between martensitic and austenitic steel for power plant application. *J. of Manufacturing Processes*, **58**, 377–406, https://doi.org/10.1016/j.jmapro.2020.08.019
5. Darwish, S.M. (2004) Analysis of weld-bonded dissimilar materials. *Int. J. of Adhesion & Adhesives*, 24, 347–354. https://doi.org/10.1016/j.ijadhadh.2003.11.007
6. Milenin, O.S., Velikoivanenko, O.A., Kozlitina, S.S. et al. (2020) Numerical prediction of the state of beam products of different thickness during layer-by-layer electron beam surfacing. *The Paton Welding J*. **1**, 14–23, https://doi.org/10.37434/tpwj2020.01.02
7. Makhnenko, O.V., Milenin, A.S., Velikoivanenko, E.A. et al. (2017) Modelling of temperature fields and stress-strain state of small 3D sample in its layer-by-layer forming. *Ibid*., **3**, 7–14, https://doi.org/10.15407/tpwj2017.03.02
8. Milenin, A.S. (2008) Physical and technological aspects of braze-welding of titanium-aluminium joints (Review). *Ibid*., **4**, 16–19.
9. Makhnenko, V.I. (1976) *Computational methods for investigation of kinetics of welding stresses and strains*. Kiev, Naukova Dumka [in Russian].
10. Makhnenko V.I. (2006) *Safe service life of welded joints and assemblies of modern structures*. Kiev, Naukova Dumka [in Russian].
11. Velikoivanenko, E.A., Milenin, A.S., Popov, A.V. et al. (2019) Methods of numerical forecasting of the working performance of welded structures on computers of hybrid architecture. *Cybernetics and Systems Analysis*, 55(**1**), 117–127.
12. (1986) *Metallurgy and technology of welding of titanium and its alloys*. Ed. by V.N. Zamkov. Kiev, Naukova Dumka [in Russian].

Received 30.11.2021

https://doi.org/10.37434/tpwj2021.01.02

INFLUENCE OF IRREGULAR CYCLIC LOAD ON FATIGUE RESISTANCE OF THIN-SHEET WELDED JOINTS OF HEAT-STRENGTHENED ALUMINIUM ALLOYS

V.V. Knysh, I.M. Klochkov, S.I. Motrunich and **A.G. Poklyatskyi**
E.O. Paton Electric Welding Institute of the NAS of Ukraine
11 Kazymyr Malevych Str., 03150, Kyiv, Ukraine. E-mail: office@paton.kiev.ua

The influence of irregular narrow band cyclic load on fatigue resistance of welded joints of heat-strengthened aluminium alloys with a thickness of 1.8–2.0 mm produced by argon arc welding using nonconsumable electrode (AAWNCE) and friction stir welding (FSW) was studied. The basic mechanical properties of the produced welded joints of aluminium D16, 1420 and 1460 alloys were determined. The fatigue curves of the investigated welded joints at narrow band cyclic block-program load with close to normal (Gaussian) and exponential distribution of stress amplitude value were plotted. It is shown that strength and fatigue resistance of welded joints of the investigated aluminium alloys produced by FSW exceed the corresponding values for the joints produced by AAWNCE in the whole range of service life of 10^5–$2\cdot10^6$ cycles of stress variation. 15 Ref., 3 Tables, 8 Figures.

Keywords: aluminium alloys, argon arc welding using nonconsumable electrode, friction stir welding, mechanical properties, fatigue resistance, irregular cyclic loads

Reducing metal consumption of products with high service characteristics and life is an important and challenging direction in development of modern engineering. The solution of this problem is closely connected with the use of aluminium alloys of different alloying systems [1, 2]. Aluminium alloys are widely used for manufacture of units of carrier rockets and spacecrafts, launching sites, air and water vessels, land transport, agricultural machinery, chemical equipment and other welded structures, which are usually operated in the conditions of variable loads [3, 4]. Depending on the peculiarities of variable load of products or structures, aluminium alloys are used, welded joints of which have the required values of fatigue resistance. Designing innovative aerospace products provides mainly for the use of aluminium alloys with a low specific weight, for example, high-strength heat-strengthened alloys of Al–Cu–Mg, Al–Su–Li and Al–Mg–Li systems [4–6]. In most cases, to produce permanent joints during manufacture of different structures from aluminium alloys, fusion welding technologies and also modern welding technologies with a lower heat input, such as solid-phase friction stir welding are used [7, 8].

The vast majority of welded metal structures of long-term use are operated under the action of variable irregular load [9]. Such loads arise, for example, during transportation or movement of loads of different sizes, under the impact of wind and waves, which are constantly changing by their nature and as a result of different types of oscillations and vibrations that appear during operation of structures. In most cases, such a loading process is random and can be described by a certain law of distribution of the random stress amplitude value (e.g., normal Gaussian distribution, Rayleigh distribution, exponential or lognormal distribution) with set parameters of mathematical expectation and mean square deviation [10]. At the same time, the modes of random load differ by a wide variety. For example, in the elements of high-speed vehicles, light metal structures, antenna-mast structures, in the structures of marine deep-water stationary platforms, etc., which can be considered as weakly damping mechanical systems, the change of operating stresses represents a narrow band random process. Therefore, taking into account the features of variable load in designing and calculation of welded element of aluminium metal structure or product for fatigue in the conditions, where they will be operated, is an urgent and important task to provide their reliability and safe operation [11]. That is why the main purpose of the work consists in studying the effect of irregular cyclic load on fatigue resistance of thin-sheet butt welded joints of heat-strengthened aluminium-lithium 1420T1, 1460T1 and duralumin D16T alloys, produced applying the technology of argon arc welding using nonconsumable electrode (AAWNCE) and friction stir welding (FSW).

V.V. Knysh — https://orcid.org/0000-0003-1289-4462, I.M. Klochkov — https://orcid.org/0000-0001-6490-8905,
S.I. Motrunich — https://orcid.org/0000-0002-8841-8609, A.G. Poklyatskyi — https://orcid.org/orcid.org/0000-0002-4101-2206

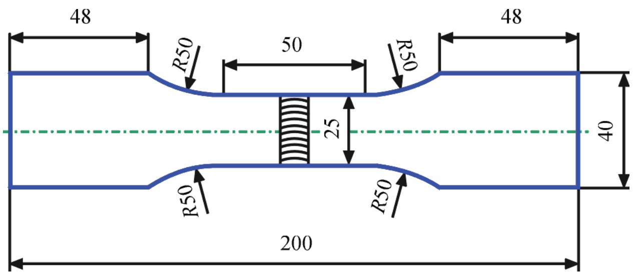

Figure 1. Appearance and geometric sizes of specimen for fatigue tests of butt welded joints

To evaluate the tensile strength and study the effect of irregular cyclic load on fatigue resistance of thin-sheet butt welded joints of aluminium 1420T1 1460T1 and D16T alloys the sheets with a thickness of 1.8–2.0 mm were used, mechanical properties of which are given in Table 1. Friction stir welding was carried out in the laboratory installation designed at the PWI, using a special tool with a conical tip and a clamp of 12 mm diameter [12], the rotation speed of which was 1420 rpm. Aluminium alloys with lithium were welded at a speed of 14 m/h, and D16T alloy at a speed of 10 m/h. For comparison, the same butt joints were produced by non-consumable electrode argon arc welding with the use of MW-450 installation (Fronius, Austria) at a welding speed of 20 m/h. As the filler material for AAWNCE of 1420T1 and D16T alloys the filler wire SvAMg63 was used, and to weld 1460T1 alloy, the filler wire Sv1201 of 1.6 mm diameter. The value of welding current for aluminium alloys with lithium was 145 A, and for D16T alloy — 160 A. The width of the welds produced by AAWNCE was at the level of 6.5 mm, and those produced by friction stir welding was 3.5 mm (at a width of a zone of thermomechanical influence on the facial side of the weld was about 12 mm).

Table 1. Mechanical properties of studied aluminium alloys

Alloy grade	σ_t, MPa	$\sigma_{0.2}$, MPa	δ, %
1420T1	459	322	11
1460T1	565	523	9
D16T	484	347	15

From the produced welded plates in accordance with DSTU ISO 4136, the specimens were made to determine the tensile strength of joints at a uniaxial tension. The width of the working part of the specimens was 15 mm. In this case, in the specimens produced by fusion welding, mechanical cleaning of the reinforcement of the root part of the weld on the level of base material was also performed, as it is common during manufacture of most structures of a critical purpose. The values of tensile strength of the investigated welded joints produced by AAWNCE and FSW technologies are given in Table 2.

Fatigue tests of joint specimens were performed in the universal servo-hydraulic complex MTS 318.25 with a maximum force of 250 kN. The specimens were tested at an axial sinusoidal load at a constant cycle asymmetry and a loading frequency of 10–15 Hz until a complete fracture. Fatigue curves were plotted for a multicycle region of life of 10^5–$2\cdot10^6$ cycles of stress variation.

Tests under irregular load were performed at a narrow band load spectrum with the stress amplitude close to normal (Gaussian) and to exponential distribution of the stress amplitude value (Table 3). The asymmetry of the stress cycle of the load spectra was accepted $R_\sigma = 0.1$, as far as this asymmetry is the most damaging for aircraft and rocket structures.

Specimens for fatigue tests of the base metal and welded joints (Figure 1) of 1420T1, 1460T1 and D16T alloys, produced by AAWNCE and FSW, were manufactured in accordance with acting national and international standards [13, 14].

Table 2. Tensile strength of welded joints of studied aluminium alloys produced by AAWNCE and FSW

Alloy grade	AAWNCE				FSW	
	Specimens with reinforcement		Specimens without reinforcement			
	σ_t, MPa	Location of fracture	σ_t, MPa	Location of fracture	σ_t, MPa	Location of fracture
1420T1	373	FZ	320	Weld	342	FZ
1460T1	311	FZ	257	Weld	309	TMAZ
D16T	330	FZ	295	Weld	425	TMAZ

Table 3. Equivalent load blocks for a narrow band random stresses spectrum

Block degree number	Spectrum No.1 (close to the normal Gaussian distribution)		Spectrum No.2 (close to the exponential distribution	
	Number of cycles	$\sigma_{a.i}/\sigma_{a.max}$	Number of cycles	$\sigma_{a.i}/\sigma_{a.max}$
1	18	1	13	1
2	170	0.96	78	0.9
3	1250	0.92	403	0.8
4	5750	0.88	2028	0.7
5	17500	0.84	10153	0.6
6	37812	0.80	50778	0.5

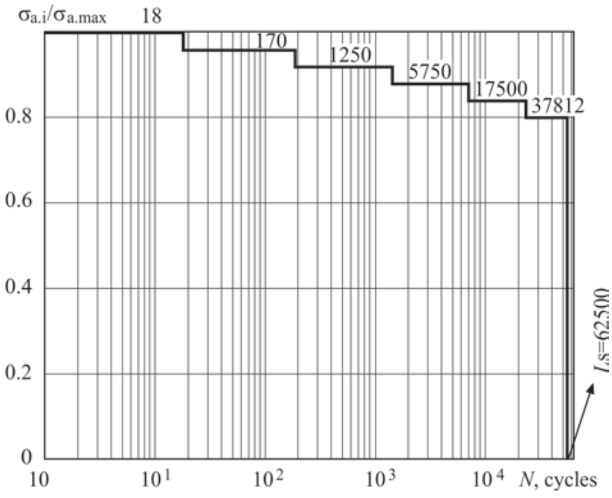

Figure 2. Block No.1 of loading specimens of D16T1 and 1420T1 alloys with the stress amplitude value close to the normal Gaussian distribution

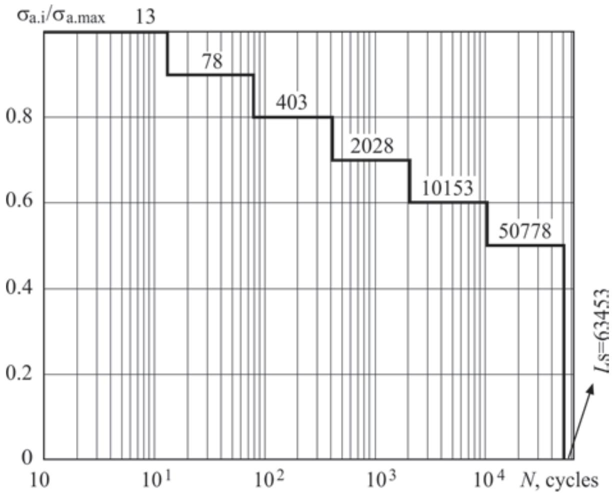

Figure 3. Block of loading specimens of joints of 1460T1 alloy with distribution of stress amplitude value close to the exponential distribution law

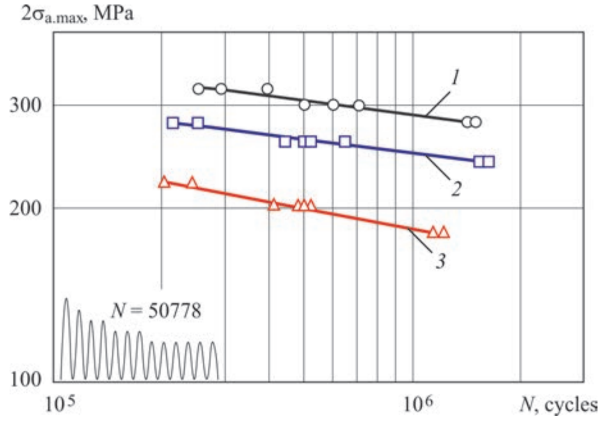

Figure 5. Gassner fatigue curves of base metal and welded joints of aluminium 1460T1 alloy with a thickness of 2 mm at block-program load No.2: *1* — base metal; *2* — welded joints produced by FSW; *3* — welded joints produced by AAWNCE

Under the same conditions, a series of 5–8 specimens of the same type was tested. The experimental data of fatigue tests were processed by the methods of linear regression analysis, generally accepted for this type of investigations [15]. According to the results of fatigue tests for each series of specimens on the basis of the established values of the limits of fatigue strength the corresponding fatigue curves — regression lines in the coordinates $\lg(2\sigma_a^{max})$ were plotted [11].

Specimens of welded joints of 1420T1 and D16T alloy were tested at a block-program load No.1, typical for airframe structures. The length of the load block was 62500 cycles of stress variation (Figure 2).

Specimens of welded joints of 1460T1 alloy were tested at a block-program load No.2, typical for the structures operated under the action of inner pressure, for example, such as cryogenic fuel tanks. Figure 3 presents the block of program load No.2, typical for pressure vessels, the length of which is 63453 cycles of stress variation.

Figure 4 shows the Gassner fatigue curves of the base metal and welded joints of aluminium 1420T1 and D16 alloys welded by AAWNCE and FSW, ob-

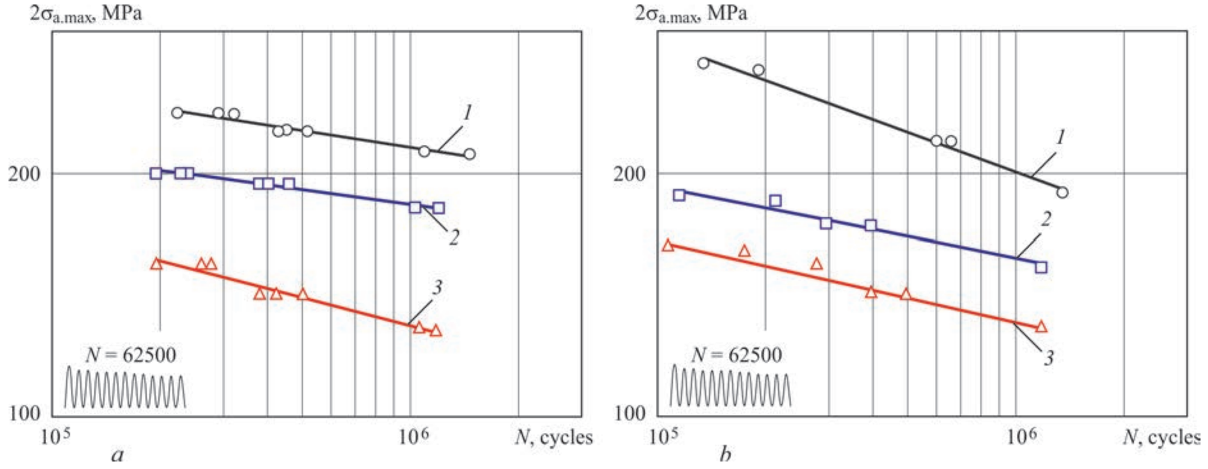

Figure 4. Gassner fatigue curves of base metal and welded joints of aluminium D16T1 (*a*) and 1420T1 (*b*) alloy with a thickness of 1.8 mm at block-program load No.1: *1* — base metal; *2* — welded joints produced by FSW; *3* — welded joints produced by AAWNCE

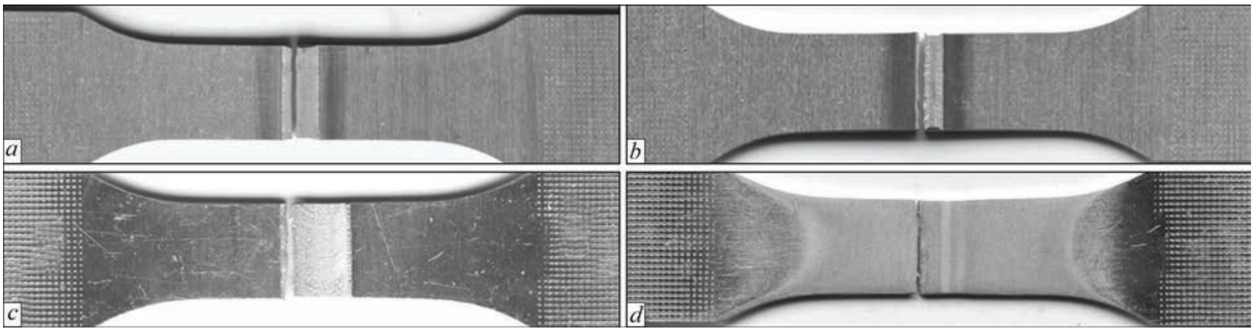

Figure 6. Appearance of facial (*a*, *c*) and lower (*b*, *d*) sides of specimens of butt joints of D16T alloy of 1.8 mm, produced by AAWNCE (*a*, *b*) and by FSW (*c*, *d*) and fractured after cyclic tests

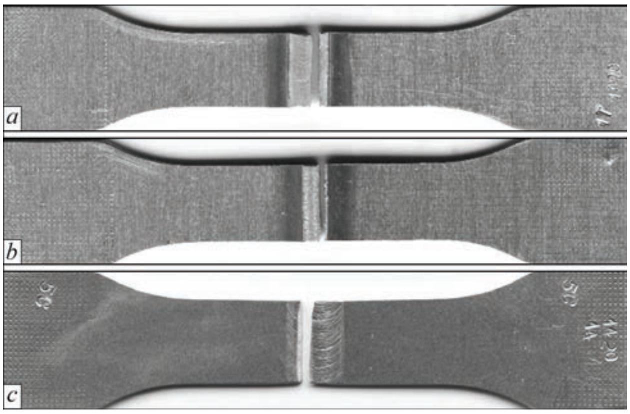

Figure 7. Appearance of facial (*a*, *c*) and lower (*b*) sides of specimens of butt joints of 1420T1 alloy of 1.8 mm, produced by AAWNCE (*a*, *b*) and by FSW (*c*) and fractured after cyclic tests

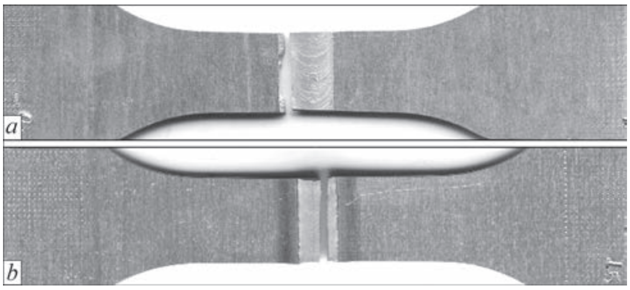

Figure 8. Appearance of facial side of specimens of butt joints of 1420T1 alloy with a thickness of 2.0 mm, produced by FSW (*a*) and by AAWNCE (*b*)

tained at a block-program load No.1. The obtained results show that the fatigue strength based on 10^6 cycles of stress variation for the welded joints of 1420T1 and D16T1 alloys, produced by FSW is by 25 and 18 % higher than the corresponding values for the joints produced by AAWNCE, and by 83 and 79 % of the corresponding values of the base metal.

Figure 5 shows the Gassner fatigue curves at a block load No.2 of the welded joints of 1460T1 alloy, produced by AAWNCE and FSW. It is shown that the value of fatigue strength based on 10^6 cycles amounts to 85 % for the joints produced by FSW, and 63 % for the joints produced by AAWNCE, relative to the corresponding value of the base metal.

Initiation and propagation of fatigue crack in the specimens with the weld reinforcement of the welded joints of aluminium D16T alloy, produced by AAWNCE, occurred in the zone of fusion of the weld with the base metal (Figure 6). This is explained by a substantial concentration of stresses and a significant softening of the metal in the weld and heat-affected-zone. Fracture of the specimens produced by FSW occurred at the boundary of the thermomechanical and heat-affected-zones on the side of the run-on tool, where a significant softening of metal is observed and a structural and slight geometric heterogeneity is formed.

Fracture of the specimens of welded joints of 1420T1 alloy with the reinforcement of the weld, produced by AAWNCE, also occurred in the area of fusion of the weld with the base metal, where a significant concentration of stresses arises during fusion welding (Figure 7). Fracture of the joints produced by FSW occurred in the thermomechanical-affected zone.

The welded joints of 1460 alloy produced by FSW were also fractured at the boundary of thermomechanical and heat-affected zones on the side of the tool, which is predetermined by softening of the metal alloyed by lithium located in the weld and in the zone of thermomechanical affect and the formation of some geometric heterogeneity (Figure 8). The specimens of welded joints with the weld reinforcement, produced by AAWNCE were fractured in the area of fusion of the weld with the base metal, where a significant concentration of stresses and a significant softening of metal arise.

Conclusions

1. Gassner fatigue curves under irregular load of butt welded joints of heat-strengthened aluminium 1420T1 and 1460T1 alloys, produced by FSW and AAWNCE technologies, were experimentally established. It was shown that the value of fatigue strength of such joints in the whole range of life 10^5–$2{\cdot}10^6$ amounts to 70–85 % of the corresponding indices of the base metal.

2. Gassner fatigue curves for a narrow band random load process with a stress amplitude value close to the normal Gaussian distribution for the joints of 1420T1 and D16T alloy produced by AAWNCE and FSW were obtained. It was shown that at such a load the fatigue strength on the basis of 10^6 cycles

for the welded joints produced by FSW, exceeds the corresponding values from the joints produced by AAWNCE by 18–25 %, and amounts to 79–83 % from the fatigue strength of the base metal.

3. It was established that for 1460T1 alloy produced by FSW and AAWNCE, the value of the fatigue strength based on 10^6 cycles in narrow band random loading process with the value of stress amplitude, approximate to the exponential law of distribution, amounts to 85 and 63 % of the corresponding value of the base metal.

4. Initiation and propagation of fatigue crack in the specimens of welded joints of the investigated aluminium alloys produced by AAWNCE occurred in the area of fusion of the weld with the base metal, where in the process of fusion welding a substantial concentration of stresses and a significant softening of metal arise. Fracture of the specimens produced by FSW during cyclic tests occurred at the boundary of thermomechanical and heat-affected zones on the side of the run-on tool, which is predetermined by softening of metal and the formation of structural and slight geometric heterogeneity in this area of the welded joint.

1. Ishchenko, A.Ya., Labur, T.M. (2013) *Welding of modern structures of aluminium alloys*. Kiev, Naukova Dumka [in Russian].
2. Ishchenko, A.Ya. (2003) Aluminium high-strength alloys for welded structures. *Progresyvni Materialy i Tekhnologii*, **1**, 50–82 [in Russian].
3. Adrian, P. (2012) *Mouritz introduction to aerospace materials*. Woodhead Publishing Ltd.
4. Fridlyander, I.N., Sister, V.G., Grushko, O.E. et al. (2002) Aluminum alloys: Promising materials in the automotive industry. *Metal Sci. and Heat Treatment*, Sept. **44**, 365–370.
5. Gureeva, M.A., Grushko, O.E., Ovchinnikov, V.V. (2008) Welded aluminium alloys in structures of transport facilities. Moscow, *VIAM, October,* 51–82 [in Russian].
6. Drits, A.M., Ovchinnikov, V.V. (2003) Comparative investigations of properties of welded joints of Russian and American aluminium-lithium alloys. *Tsvetnye Metally*, **12**, 71–77 [in Russian].
7. Threadgill, P.L., Leonard, A.J., Shercliff, H.R., Withers, P.J. (2009) Friction stir welding of aluminium alloys. *J. Int. Materials Reviews*, 54(**2**), 49–93.
8. Ishchenko, A.Ya. (2004) Specifics in application of aluminium high-strength alloys for welded structures. *The Paton Welding J.*, **9**, 15–25.
9. Schijve, J. (2009) *Fatigue of structures and materials*. 2nd Ed. Springer. Berlin.
10. Heuler, P., Bruder, T., Klätschke, H. (2005) Standardized loadtime histories a contribution on to durability issuer under spectrum loading. *Mat.-wiss.u. Werkstofftech*., 36(**11**), 669–677.
11. Sonsino, C.M. (2007) Fatigue testing under variable amplitude loading. *Int. J. Fatigue*, **29**, 1080–1089.
12. Ishchenko, A.Ya., Porlyatsky, A.G. (2010) *Tool for friction stir welding of aluminium alloys*. Pat. Ukraine, 54096, Int. Cl. B23K 20/12. Fill. 30.04.2010, Publ. 25.10.2010 [in Ukrainian].
13. (1979) GOST 25.502–79: *Strength analysis and testing in machine building. Methods of metals mechanical testing. Methods of fatigue testing* [in Russian].
14. (2017) ISO 1099:2017: *Metallic materials. Fatigue testing. Axial force-controlled method* [in Russian].
15. Drejper, N., Smit, G. (1986) *Applied regression analysis*. Book 1. In: 2 Books. Moscow, Finansy i Statistica [in Russian].

Received 28.12.2020

https://doi.org/10.37434/tpwj2021.01.03

PREDICTION OF RESIDUAL STRESSES AFTER WELDING OF DUPLEX STEEL TAKING INTO ACCOUNT PHASE TRANSFORMATIONS

O.S. Kostenevych[1] and **JR en**[2]
[1]The Experimental Design and Technological Bureau of the E.O. Paton Electric Welding Institute
of the NAS of Ukraine
15 Kazymyr Malevych Str., 03150, Kyiv, Ukraine. E-mail: alenakostenevich@gmail.com
[2]School of Engineering, Liverpool John Moores University
3 Byron Str., United Kingdom. E-mail: x.j.ren@ljmu.ac.uk

The presented study involved mathematical modelling of single pass TIG welding of duplex stainless steel S32205. The temperature fields, the fusion zone and HAZ dimension, the cooling rate fields, residual stresses taking into account kinetics of dissolution of austenite during heating and kinetics of precipitation of austenite during cooling were obtained. The comparative analysis of residual stresses with/without phase transformations showed the difference of residual stresses distribution due to different amounts of austenite and ferrite and due to volumetric changes during phase transformations. 24 Ref, 1 Table, 9 Figures.

Keywords: duplex stainless steel, TIG welding, phase transformations, austenite, ferrite, residual stresses

Duplex stainless steels (DSSs) contain approximately equal amounts of austenite (γ) and ferrite (α), which offer many advantages over other single phased stainless steels. DSSs have higher strength than austenitic steels, higher impact value and higher resistance against hydrogen embrittlement than ferritic steels. DSSs with optimum volume fractions of ferrite and austenite also possess a higher resistance against general corrosion, intergranular, pitting, crevice corrosion and stress-corrosion cracking. The application of DSSs covers a broad range of industries such as the oil and gas, petrochemical, chemical industries, energy industry, marine structures, as well as general structures such as architecture, building, construction and mechanical engineering. For most of these applications, the combination of strength and corrosion resistance is a particularly important consideration for the design, manufacturing and structure maintenance. Many of these applications involve welding of similar or dissimilar grades of DSSs with different types of welding [1–5] including tungsten inert gas (TIG) welding.

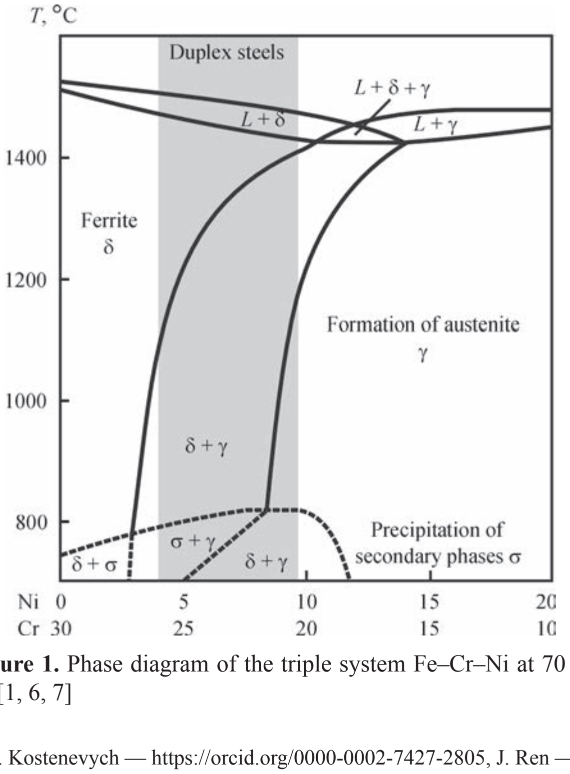

Figure 1. Phase diagram of the triple system Fe–Cr–Ni at 70 % Fe [1, 6, 7]

When welding duplex steels, a general requirement during welding of DSSs is limitation of the welding heat input. The upper temperature limit of heat input is limited by the formation of intermetallic phases, and the lower — by an acceptable ratio of austenite and ferrite. It is recommended to adhere to a heat input of 0.5–2.5 kJ/mm for steels containing 22 % chromium and 0.2–1.5 kJ/mm for super duplex steels with 25 % chromium [1, 2]. One major focus for welding process design is to retain the good combination of properties, which is sensitive to the chemical composition and microstructure of the fusion and heat-affected zones (HAZ). Particular features governing the structural integrity are the volume fractions of the ferrite and austenite phases, the phase transfor-

O.S. Kostenevych — https://orcid.org/0000-0002-7427-2805, J. Ren — https://orcid.org/0000-0001-6132-1228

Chemical composition for 2205 grade stainless steel [4]

Grade	C	Mn	Si	Cr	Mo	Ni	N	P	S
2205 (S32205)	<0.03	<2.0	<1.0	22.0–23.0	3.0–3.5	4.5–6.5	0.14–0.20	<0.03	<0.02

mation over critical temperature-composition ranges (Figure 1) and residual stresses.

Many recent work have reported on the phase volumes changes in welding DSSs, but systematic works on the effect of microstructural phase transformations on residual stresses are still limited [8–12]. Residual stresses in welding are an important factor influencing both the mechanical strength and the corrosion resistance of DSSs, such an issue needs to be addressed with good accuracy taking into account phase transformations.

This work presents a comparative analysis of the distribution of residual stresses after welding of DSS taking into account microstructural transformations. The main mathematical models, numerical procedures and typical results are introduced. The work is applied in analyzing TIG welding of standard duplex steel S32205, the data includes temperature fields, characteristic cooling rates and microstructure composition. The residual stresses distribution with/without phase transformations is presented and discussed.

Modelling approaches of the temperature fields and phase transformations. In this work, the TIG welding process of standard duplex stainless steel S32205 (Table) taking into account microstructural transformations was simulated and temperature fields, characteristic cooling rates, microstructure composition and residual stresses were obtained. The analysis is focused on single pass TIG welding process without preheating: $I = 120$ A, $U = 10$ V, welding speed 1.5 mm/s. The heat input was $H = 600$ J/mm, which is in the recommended range of $512 < H < 2520$ J/mm for welding of duplex steels [2].

The chemical composition of standard duplex steel S32205 is listed in Table. Thermo-physical properties of base material were adapted from literature data [12, 13]. The latent heat of fusion is 300 J/g.

Simulation has been carried out using finite element calculation model (ABAQUS) on a plate of thickness 3 mm with dimension 100×100 mm. As a heat source model, Goldak's double ellipsoid heat source model [14] was used. The heat distribution in a solid is described by the differential heat equation, which in the general case for the Cartesian coordinate system (x, y, z) has the form:

$$c\rho\frac{\partial T}{\partial t}=\frac{\partial}{\partial x}\left(\lambda\frac{\partial T}{\partial x}\right)+\frac{\partial}{\partial y}\left(\lambda\frac{\partial T}{\partial y}\right)+\frac{\partial}{\partial z}\left(\lambda\frac{\partial T}{\partial z}\right)+q, \quad (1)$$

where $c\rho$ — volumetric heat capacity of the material; λ — thermal conductivity; q — power distribution of a volumetric heat source.

Goldak's heat source model is built from two ellipsoids described with equations [14] for front part model q_f and rear part of model q_r:

$$q_f(x,y,z)=\frac{6\sqrt{3}f_fQ}{abc_f\pi\sqrt{\pi}}\exp\left(-3\left(\frac{x^2}{a^2}+\frac{y^2}{b^2}+\frac{z^2}{c_f^{\,2}}\right)\right); \quad (2)$$

$$q_r(x,y,z)=\frac{6\sqrt{3}f_rQ}{abc_r\pi\sqrt{\pi}}\exp\left(-3\left(\frac{x^2}{a^2}+\frac{y^2}{b^2}+\frac{z^2}{c_r^{\,2}}\right)\right). \quad (3)$$

The heat input rate $Q = \eta VI$ is defined by welding operational parameters current (I), voltage (V) and thermal efficiency (η), respectively. The factors f_f and f_r denote the fraction of the heat deposited in the front and rear quadrant respectively, which must satisfy the condition $f_f + f_r = 2$. The a, b_f, b_r and c are source constant parameters that define the size and shape of the ellipses, therefore the heat source distribution.

The cooling boundary conditions between the plate and surrounding environment by convection are calculated by the equation:

$$-\lambda\frac{\partial T}{\partial n}=h(T-T_0), \quad (4)$$

where T_0 (20 °C) is the room temperature and h (20 $\mathrm{W{\cdot}m^{-2}{\cdot}K^{-1}}$) is the natural convective heat coefficient assumed.

Based on the solution of the heat equation by the finite element method, temperature fields of the calculation scheme were obtained. Calculation results of temperature fields for TIG welding process of DSS 2205 are given in Figures 2 and 3. The width of fusion zone ($T_{max} \geq 1450$ °C) is 2.6 mm (at the bottom of the weld)-4.7 mm (at the top of the weld). Since the ferritic-austenitic transformation in duplex steels takes place in the temperature range from 1200 to

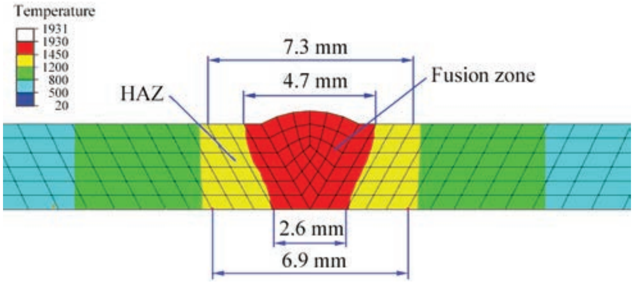

Figure 2. Dimension of the fusion zone and HAZ, mm

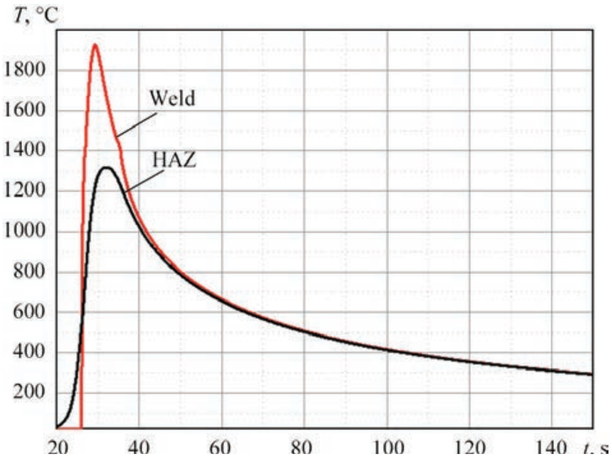

Figure 3. Characteristic thermal cycles in weld zone and HAZ

800 °C, the zone with the maximum heating temperature above 1200 °C was taken as the heat affected zone (HAZ). It`s depth in the base material is up to 1.3–2.15 mm (Figure 2).

An important characteristic during welding duplex steels is the cooling rate in the temperature range 1200–800 °C [15–17]. Since cooling is fast by the single pass welding, the obtained time $\Delta t_{1200/800}$ of the calculation model is equal 10–14s (Figure 3), the cooling rate $w_{1200/800}$ is from 28 to 40 °C/s. Comparison of cooling curve with TTT- and CCT-curve [18] shows, that due to fast speed cooling after welding (the cooling speed $w_{1200/800} = 28–40$ °C/s >> 0.23 °C/s) the σ-phase (sigma phase) will not form. Sigma phase precipitation is possible during aging at high temperatures or in multi-pass welding [19, 20] due to low cooling rates.

The kinetics of the microstructure phase transformation during welding the DSS on the basis of literature data [17, 21] was modelled. Weldments of DSS with a Cr_{eq}/Ni_{eq} ratio above 1.95 (for steel S32205 $Cr_{eq}/Ni_{eq} = 3.5$) can be treated as a single-phase ferrite [22] when solidifying. The dissolution and precipitation kinetics of austenite in duplex stainless steels is followed by the Austin–Rickett type equation [17, 21]:

$$\frac{y}{1-y} = (kt)^n, \tag{5}$$

where y is the fraction transformed, k is the kinetics constant, t is the time and n is the time exponent.

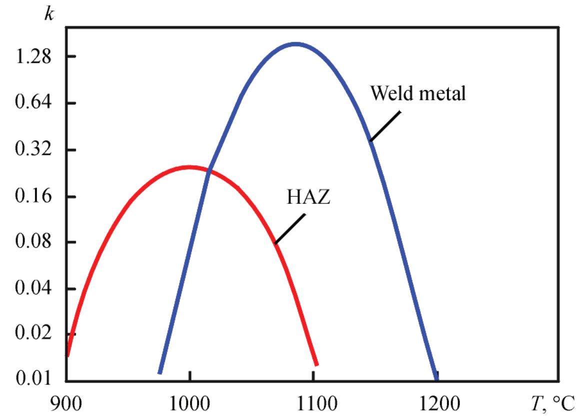

Figure 4. The precipitation kinetics constant $k(T)$ [21]

The temperature dependency of dissolution rate $k(T)$ of austenite phase in DSSs is as follows [21]:

- for HAZ of standard DSSs

$$k(T) = \exp\left(-\frac{4.05\cdot 10^4}{(T+273)} + 25.6\right); \tag{6}$$

- for weld metal of standard DSSs

$$k(T) = \exp\left(-\frac{5.82\cdot 10^4}{(T+273)} + 37.4\right). \tag{7}$$

Temperature dependency of equilibrium austenite phase fraction of standard DSS $F_{eq}(T)$ and precipitation parameters n, $k(T)$ were obtained from work [21] (Figure 4).

Since heating during the welding thermal cycle occurs without aging and cooling continuously with a variable cooling rate, the Austin-Rickett equation was accepted as modified equation taking into account the features of the welding thermal cycle. For this, the heating and cooling curve was divided into steps and the fraction of austenite was determined by the expression below [17]:

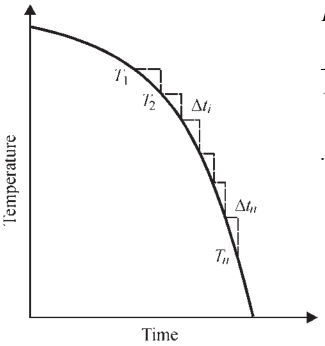

$$\frac{y}{Feq(T)-y} = \left[k(T)t\right]^n$$

$$\frac{y_j}{Feq(T_j)-y_j} = (k(T_1)+k(T_2)+\ldots$$

$$\ldots + k(T_j))^n \Delta t^n = \left[\Delta t \sum_{i=1}^{j} k(T_i)\right]^n$$

$$y_j = \frac{\left[\Delta t^n \sum_{i=1}^{j} k(T_i)^n Feq(T_i)\right]}{1+\left[\Delta t \sum_{i=1}^{j} k(T_i)\right]^n}. \tag{8}$$

The results of the microstructure composition and kinetics of phase transformation in the HAZ and weld metal shown in Figure 5 were obtained using Austin-Rickett equation (8) and precipitation parameters $k(T)$, n from work [21].

On the basis of equation (8) high content of austenite in weld metal and low content of austenite in HAZ was obtained. According to Figure 5 the phase composition in weld metal are 65 % austenite and 35 % ferrite, in the HAZ are 28 % austenite and 72 % ferrite. These data of microstructure composition (Figure 5) were used for the determining of the distribution of residual stresses after welding of DSS 2205.

Modelling of residual stresses, results and analysis

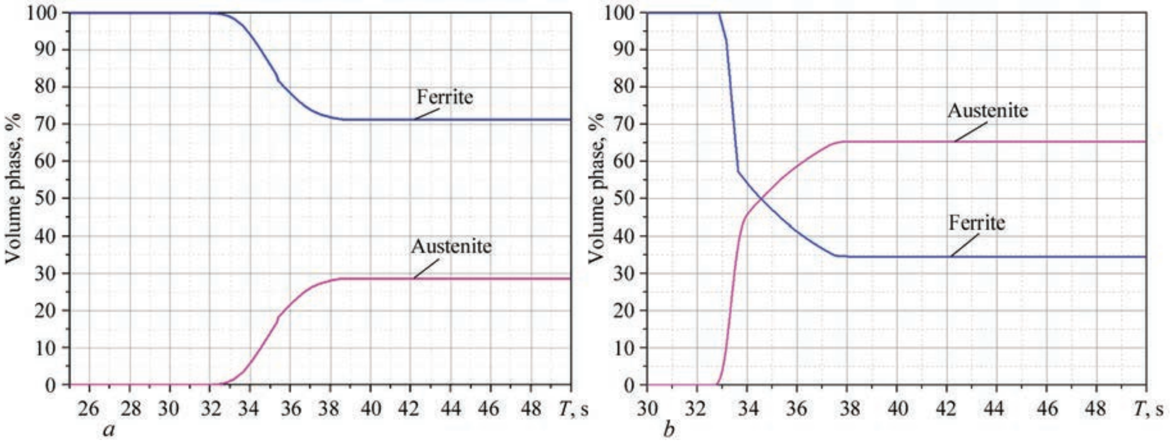

Figure 5. Kinetics of phase transformation during cooling of welding thermal cycle: *a* — point in the HAZ; *b* — point in the weld metal

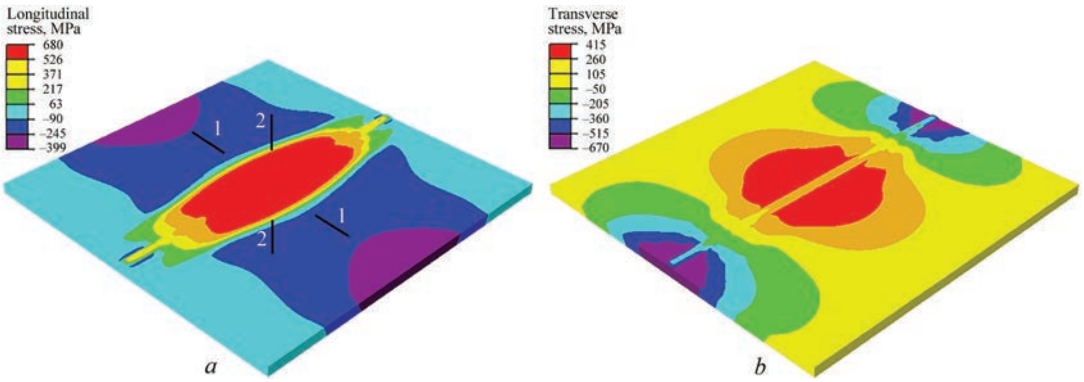

Figure 6. Residual stresses after welding and cooling without taking into account microstructural transformations: *a* — longitudinal stresses, MPa; *b* — transverse stresses, MPa

Phase transformations in steels can occur with significant volumetric changes, which mainly effects on the kinetics of the distribution of residual welding stresses and strains [23, 24].

The temperature and phase volume data presented in the previous section provided a framework to comparatively study the residual stresses with/without taking into account of the microstructural transformations, typical results are shown in Figures 6, 7. Figure 6 is a plot of residual stress without taking into account of the phase changes, while Figure 7 is result incorporated the microstructural transformations in the model. A significant difference could be observed in the distribution pattern and magnitudes of the residual stresses.

Figure 8 compares the profiles of residual stresses along cross-section 1 (transversely to the weld) for model without phase transformations and model taking into account of phase transformations. It clearly shows that residual stresses distribution from these two approaches is different for both the longitudinal and the transverse stresses, with the latter exhibit more significant differences. With a lower austenite content/higher ferrite content in the heat affected zone, a decrease in tensile longitudinal residual stresses is observed.

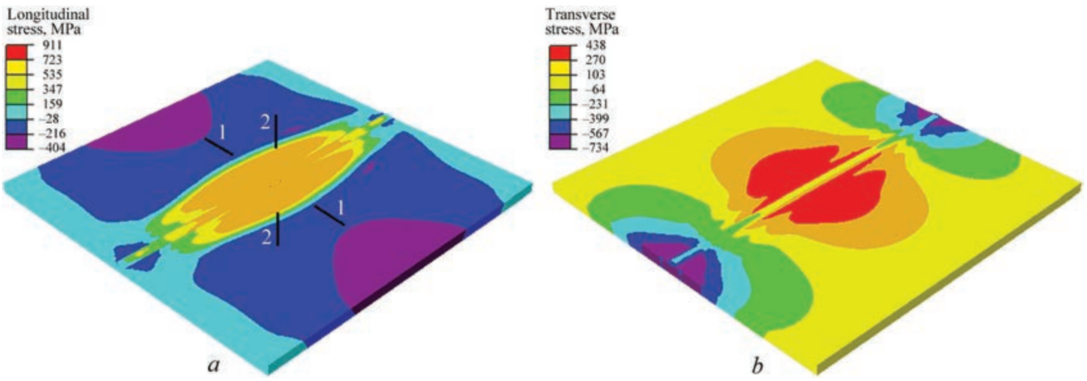

Figure 7. Residual stresses after welding and cooling taking into account the kinetics of austenitic transformation: *a* — longitudinal stresses, MPa; *b* — transverse stresses, MPa

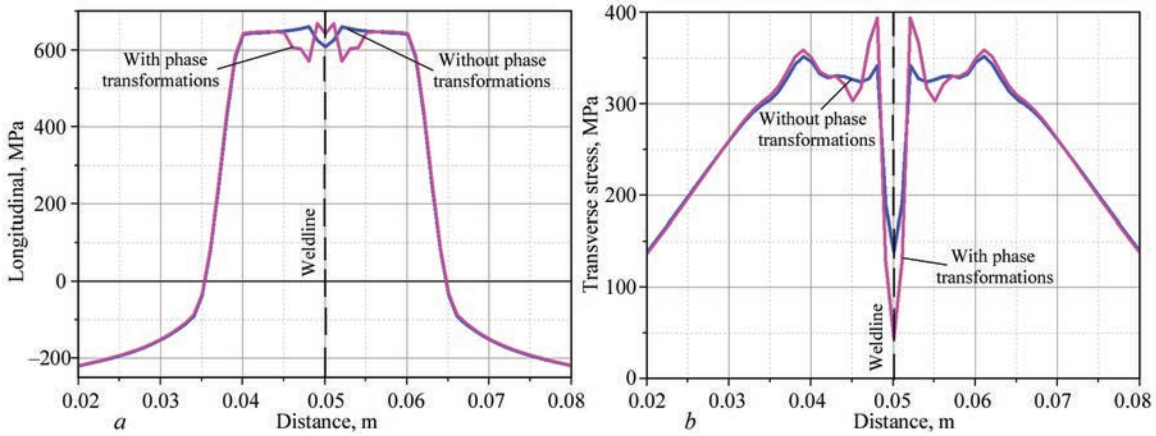

Figure 8. Residual stresses distribution through cross-section 1: *a* — longitudinal stresses; *b* — transverse stresses

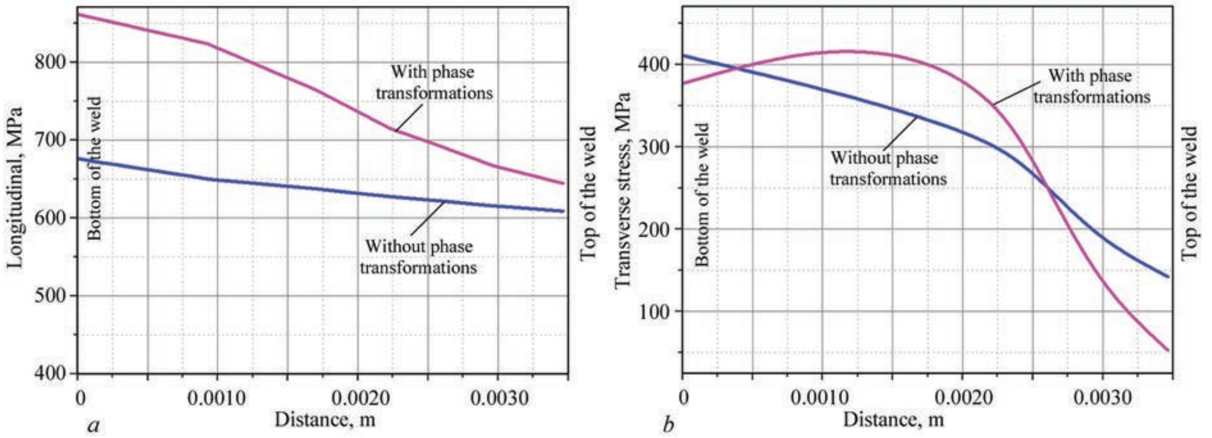

Figure 9. Residual stresses distribution through cross-section 2: *a* – longitudinal stresses; *b* – transverse stresses

Figure 9 compares the distributions of simulated residual stresses along cross-section 2 (through thickness of the weld) for model without phase transformations and model taking into account phase transformations. The longitudinal stresses from both modelling approaches show a gradual reducing trend with the distance (from root to top of the weld) before the difference becoming less significant. In the transverse stress data, the trend in the residual stresses is different between these two modelling approaches. The stresses level gradually decreases from root to top of the weld for the model without considering the phase transformation, while the data from the model considering the phase transformations show an increase in the stress first followed by a decrease trend at the top of the weld.

Compared to the results without phase transformations, the difference in the magnitudes of the residual stresses is up to 50–100 MPa in cross-section 1 and up to 90–185 MPa in cross-section 2. In future works, systematic data with different welding conditions of samples with different dimensions/constraints will be further developed, the effect of the residual stresses on the strength, toughness and corrosion will be studied.

Conclusions

1. In the present study TIG single-pass welding process of duplex stainless steel S32205 taking into account of microstructural transformations was simulated. The obtained cooling rate in the temperature range 1200–800 °C (time $\Delta t_{1200/800}$) is equal 10–14s.

2. Using calculating method on the basis of the Austin-Rickett equation, the predicted data of obtained austenite content 65 % — in the weld and 28 % — in the HAZ.

3. The microstructural transformations showed an influence on the distribution of residual stresses after welding of DSS. In comparison with residual stresses without phase transformations, a higher value of longitudinal residual stresses was obtained in the weld with high amount of austenite. In the case of a lower austenite content (in the HAZ) accounting of phase transformations leads to a decrease in the tensile longitudinal residual stresses value and an increase of transverse tensile residual stresses value.

Acknowledgments. *The present study was financially supported by EU Horizon 2020 MSCA-RISE Project («i-Weld») No. 823786.*

1. (2014) Practical guidelines for the fabrication of duplex stainless steels. *International Molybdenum Association* (IMOA); 3rd Ed.
2. Ammann, T. (2007) Arc welding of duplex steels in a shielding gas environment. *Svetsaren, the ESAB Welding and Cutting Journal*, 62(**1**), 41–45 [in Russian]. ?????
3. (2019) Duplex stainless steels welding guidelines. *Industeel Arcelor Mittal*, June.
4. (2011) *API Technical Report 938-C: Use of Duplex Stainless Steels in the Oil Refining Industry*, Second Ed.
5. Pramanik, A., Littlefair, G., Basak, A.K. (2015) Weldability of duplex stainless steel. *Materials and Manufacturing Processes*, 30(**9**), 1053–1068; DOI: 10.1080/10426914.2015.1019126
6. Vahid Hosseini (2018) S*uper duplex stainless steels — microstructure and properties of physically simulated base and weld metal*: PhD Thesis Production Technology, 24. University West, Sweden.
7. Kim, Yoon-Jun (2004) *Phase transformations in cast duplex stainless steels*. Other Information: TH: Thesis (Ph.D.); Submitted to Iowa State Univ., Ames, IA (US); PBD: 19 Dec.
8. Brytan, Z., Niagaj, J., Pakieła, W., Bonek, M. (2015) FEM modeling of lean duplex stainless steel welding. *J. of Achievements in Materials and Manufacturing Engin.*, 70(**1**), 36–44.
9. Gideon, B., Ward, L., Carr, D.G., Muransky, O. (2008) Duplex stainless steel welds: residual stress determination, magnetic force microscopy and susceptibility to intergranular corrosion. In: *Proc. of 6th European Stainless Steels Conf., Helsinki, Finland, 10–13 June 2008*, F-2P, 629–636.
10. Giętka, T., Ciechacki, K., Kik, T. (2016) Numerical simulation of duplex steel multipass welding. *Archives of Metallurgy and Materials*, 61(**4**), 1975–1984, December.
11. Floreka, A., Křížb, A., Vilcsekc, I. (2019) Numerical modelling of welding of duplex steel. In: *AIP Conf. Proceedings* 2189, 020006.
12. Tae-Hwan Um, Chin-Hyung Lee, Kyong-Ho Chang, Vuong Nguyen Van Do (2018) Features of residual stresses in duplex stainless steel butt welds. *IOP Conference Series Earth and Environmental Science,* 143(**1**):012030
13. Leffler, B. (2013) *Stainless steels and their properties*. http://www.hazmetal.com/f/kutu/1236776229.pdf
14. Goldak, J., Chakravart, A., Bibby, M. (1984) A new finite element model for welding heat sources. *Metallurgical Transact. B, Process Metallurgy*, 15(**2**), 299–305. http://dx.doi.org/10.1007/BF02667333.
15. Toshio Kuroda, Kenji Ikeuchi, Yoshihiko Kitagawa (2004) Microstructure control for joining advanced stainless steel. In: *Proc. of the Intern. Symp. on Novel Materials Processing by Advanced Electromagnetic Energy Sources (March 1–2, 2004, Osaka, Japan)*, 419–422.
16. Varbai, B., Adonyi, Y., Baumer, R. et al. (2019) Weldability of duplex stainless steels — thermal cycle and nitrogen effects: Duplex stainless steel weld microstructures were investigated as a function of weld thermal cycles and shielding gas nitrogen content. *Welding J.*, **98**, 78–87.
17. Koichi Yasuda, Robert N. Gunn, Trevor G. Gooch (2002) Prediction of Austenite Phase Fraction in Duplex Stainless Steel Weld Metals. *Qarterly J. of the Japan Welding Society*, 20(**1**), 68–77.
18. Sieurin, H., Sandstrom, R. (2007) Sigma phase precipitation in duplex stainless steel 2205. *Materials Sci. and Engin. A*, **444**, 271–276.
19. Nishimoto, K., Saida, K., Katsuyama, O. (2006) Prediction of sigma phase precipitation in super duplex stainless steel weldments. *Weld World*, **50**, 13–28. https://doi.org/10.1007/BF03263429
20. Makhnenko, V.I., Kozlitina, S.S., Dzyubak, L.I. (2011) Forecasting the content of σ-phase in the HAZ of welded joints of duplex steels in arc welding. *The Paton Welding J.*, **6**, 6–8.
21. Ogura T., Matsumura T., Yu L. et al. (2018) Numerical simulation of ferrite/austenite phase fraction in multipass welds of duplex stainless steels. Mathematical modelling of weld phenomena 12. In: *Proc. of Intern. Sem. Numerical Analysis of Weldability, Graz, Austria*. DOI 10.3217/978-3-85125-615-4-07
22. Ghusoon Ridha Mohammed, Mahadzir Ishak, Syarifah N. Aqida, Hassan A. Abdulhadi (2017) Effects of heat input on microstructure, corrosion and mechanical characteristics of welded austenitic and duplex stainless steels: A *Review. Metals — Open Access Metallurgy J.*, 7(**2**), 39.
23. Makhnenko, V.I., Velikoivanenko, E.A., Pochinok, V.E. et al. (1999) Numerical methods for the prediction of welding stress and distortions. *Welding and Surfacing Reviews*, 13(**1**).
24. Yuriev, S.F. (1950) *Specific volume of phases in the martensitic transformation of austenite*. Moscow, Metallurgizdat [in Russian].

Received 08.12.2020

https://doi.org/10.37434/tpwj2021.01.04

COMPARATIVE ANALYSIS OF THE RESULTS OF COMPUTER SIMULATION OF HEAT TRANSFER AND HYDRODYNAMIC PROCESSES IN THE METAL BEING WELDED BY MEANS OF DIFFERENT SOFTWARE TOOLS

O.P. Semenov[1], **I.V. Krivtsun**[1], **A.V. Lykhoshva**[1], **O.I. Hluchenkyi**[2] and **O.I. Bondar**[2]
[1]E.O. Paton Electric Welding Institute of NAS of Ukraine,
11 Kazymyr Malevych Str., 03150, Kyiv, Ukraine. E-mail: office@paton.kiev.ua
[2]The Institute of Electrodynamics of NAS of Ukraine
56 Peremohy Prosp. 03057, Kyiv, Ukraine

In this work we considered two software tools for the purpose of multiphysics simulation of physical phenomena in weld pool: COMSOL Multiphysics and in-hose finite element (FE) code implemented in Wolfram Mathematica. For validation purpose, two test problems dealing with Marangoni induced convection are solved. Good agreement between benchmark solutions and obtained results is observed. Developed numerical algorithms and computer code can readily be employed for multiphysics simulation in welding. 14 Ref., 1 Table, 8 Figures.

Keywords: marangoni convection, weld pool shape, mathematical modelling, laser beam welding

Convection is the main mechanism of heat transfer in the weld pool during fusion welding and it significantly influences on final penetration of the weld. The driving forces for fluid flow in the weld pool include buoyancy force, electromagnetic force, the shear stress induced by surface tension gradient (Marangoni effect) on the free surface and mechanical interaction with arc plasma [1, 2]. While Lorentz force appears only in arc welding, Marangoni induced convection inherent to all types of fusion welding. By means of methods of physical simulation it was shown that Marangoni force gives rise to appearance of two counter rotating cells in meridional section of the weld pool in the case of spot welding [3]. Simulations performed in [4] confirm suchlike flow pattern. However, surface tension is highly effected by presence of surfactants and non-monotonically depends on temperature [5, 6] that is eventually influences on penetration depth [7]. That fact significantly complicates experimental determination of surface tension of liquid metals in conditions inherent to fusion welding. Influence of Lorentz force on convection in TIG welding is determined by welding current and dimension of anode region. The smaller the anode spot the greater the Lorentz force pushes the liquid metal downward [8, 9], and thereby increasing pool depth. Detailed experimental investigation of each driven force separately deals with considerable technical difficulties. Therefore, methods of Computational Fluid Dynamics (CFD) nowadays remain the most popular tools for the analysis of the coupled physical processes in the weld pool. A lot of possibilities exist to simulate heat transfer, electromagnetic and hydrodynamic processes in the weld pool. However, simulation results obtained by different software tools may differ. Careful verification should proceed the complex multiphysics simulation of the above mentioned phenomena. In current paper we focus on comparative analysis of simulation results of heat and mass transfer processes in weld pool obtained separately by commercial software COMSOL Multiphysics and in-hose FE code. For validation of algorithms and computer codes, we considered two numerical test cases, which are concerned with thermocapillary flow.

Governing equations. Model of hydrodynamic processes is based on Navier-Stokes equations for incompressible fluid, which in the case of axial symmetry can be written as follows

$$\rho\left(\frac{\partial u}{\partial t}+u\frac{\partial u}{\partial r}+v\frac{\partial u}{\partial z}\right)=\frac{1}{r}\frac{\partial}{\partial r}\left(r\sigma_{rr}\right)+\frac{\partial \sigma_{rz}}{\partial z}-$$
$$-\frac{\sigma_{\phi\phi}}{r}-u\frac{C\left(1-f_l\right)^2}{f_l^3+e_0}; \qquad (1)$$

I.V. Krivtsun – https://orcid.org/0000-0001-9818-3383

$$\rho\left(\frac{\partial v}{\partial t}+u\frac{\partial v}{\partial r}+v\frac{\partial v}{\partial z}\right)=\frac{1}{r}\frac{\partial}{\partial r}\left(r\sigma_{rz}\right)+$$
$$+\frac{\partial\sigma_{zz}}{\partial z}-v\frac{C\left(1-f_l\right)^2}{f_l^3+e_0}; \qquad (2)$$

$$\frac{1}{r}\frac{\partial}{\partial r}\left(ru\right)+\frac{\partial v}{\partial z}=0. \qquad (3)$$

Here r, z are the radial and axial coordinates accordingly, u, v, P are the velocity components and pressure respectively, ρ denote density of the fluid, σ_{rr}, σ_{zz}, σ_{rz}, $\sigma_{\phi\phi}$ are the nonzero components of stress tensor. For Newtonian fluid we have relations

$$\sigma_{rr}=-P+2\mu\frac{\partial u}{\partial r},\ \sigma_{zz}=-P+2\mu\frac{\partial v}{\partial z},\sigma_{rz}=$$
$$=\mu\left(\frac{\partial u}{\partial z}+\frac{\partial v}{\partial r}\right),\ \sigma_{\phi\phi}=-P+2\mu\frac{u}{r}. \qquad (4)$$

where μ is dynamic viscosity. Last two terms in the right-hand sides of equations (1), (2) describe fluid deceleration in the mushy zone [10]. Here f_l is a liquid fraction, C is a constant of mushy region, e_0 is a small value constant which prevents division by zero. In solid region these terms totally dominate all the terms in the momentum equations so that velocity vanishes. For description of heat transfer processes we employ energy conservation equation written in enthalpy form

$$\rho\left(\frac{\partial h}{\partial t}+u\frac{\partial h}{\partial r}+v\frac{\partial h}{\partial z}\right)=$$
$$=\frac{1}{r}\frac{\partial}{\partial r}\left(r\lambda\frac{\partial T}{\partial r}\right)+\frac{\partial}{\partial z}\left(\lambda\frac{\partial T}{\partial z}\right), \qquad (5)$$

where λ is thermal conductivity, h and T denote specific enthalpy and temperature, which in turn are related by

$$h\left(T\right)=\int_{T_0}^{T}c\left(\tilde{T}\right)d\tilde{T}+Lf_l\left(\tilde{T}\right). \qquad (6)$$

Variables c and L in (6) denote specific heat and latent heat of fusion accordingly, T_0 is initial temperature of material. Finally, the liquid fraction temperature dependence is chosen by the next way

$$f_l\left(T\right)=\begin{cases}0, & T<T_s\\ (T-T_s)/(T_l-T_s), & T_s\le T\le T_l,\\ 1, & T>T_l\end{cases} \qquad (7)$$

where T_s, T_l are the solidus and liquidus temperatures respectively. Governing equations are solved numerically by means of characteristic-based finite element method [11]. We use quadrilaterals elements along with linear shape functions for pressure approximation and quadratic one for temperature and velocity fields. All the numerical algorithms were implemented in Wolfram Language.

Test problem 1. Marangoni convection in a thin liquid layer. The first test problem presented is a plane Marangoni convection in a thin liquid layer with infinite length (Figure 1). Phase change effects are not included in the model. By assumption the surface tension is quadratically dependent on temperature by $\sigma = \sigma_0 + \alpha(T - T_c)^2/2$, where σ_0, α are the constant values and T_c is a critical temperature at which surface tension reaches a minimum. Boundary conditions to the problem considered are the next

$$y = 0,\ u = v = 0,\ T = T_c + Ax \qquad (8)$$

$$y=H,\ \mu\frac{\partial u}{\partial y}=\frac{d\sigma}{dT}\frac{\partial T}{\partial x},\ v=0,\ \frac{\partial T}{\partial y}=0, \qquad (9)$$

where A = const, H is a layer thickness. The first condition from (9) reflects the balance of thermocapillary force and shear stress on the free surface. An analytical solution of this problem was derived in [12] for small Marangoni number, defined by $Ma = \alpha A^2H^3\rho/\mu^2$. The space coordinates, velocities are made dimensionless by H and $\mu Ma/(H\rho)$ respectively. The temperature is nondimensionalized as $(T - T_c)/(AH)$. For the numerical analysis we chose finite computation region with aspect ratio 1/20. Calculation were carried out by means of in-hose code. Because of sign change in surface tension temperature gradient $\gamma = d\sigma/dT$ at $x = 0$, flow pattern has a symmetrical structure (Figure 1). A good agreement with benchmark solution is observed under $Ma = 1$ (Figure 2). In the case of high Ma numbers the discrepancy between analytical and numerical solutions becomes significant.

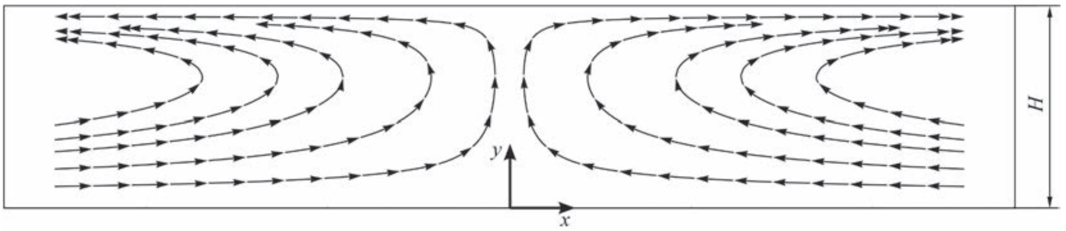

Figure 1. Thermocapillary convection in a thin liquid layer

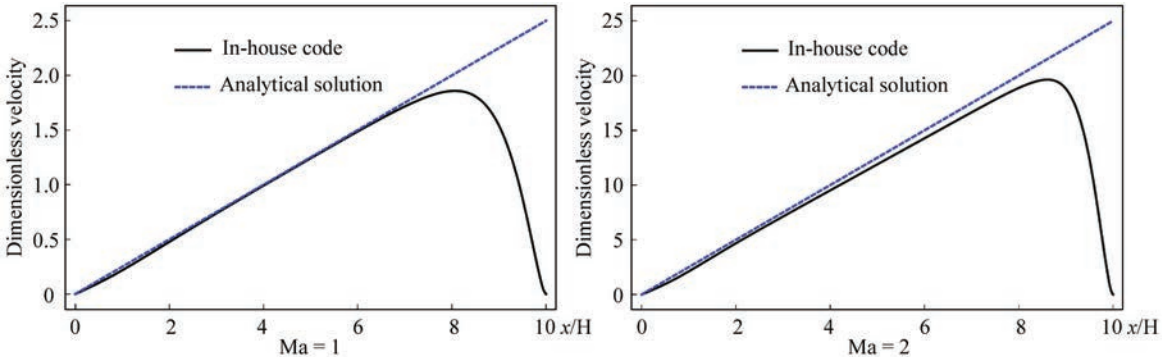

Figure 2. Velocity distribution along free surface of the liquid layer

Test problem 2. Marangoni induced convection in weld pool during laser spot welding. The problem considered in [13] dealing with weld pool dynamics in laser spot welding of the Böhler S705 steel was selected as a second benchmark problem. In paper [14] the same problem was considered. Open source finite volume CFD code OpenFoam was used in work [13] whereas in-house code Argo DG based on FEM was utilized in [14] for calculations. All the physical processes considered are supposed to be axisymmetric. Both thermocapillary and phase change effects are included in the model. Guided by the papers [13, 7] the values of liquid thermal conductivity and dynamic viscosity were increased by a factor of 7. Such an approach aimed at accounting for the enhanced heat and mass transfer caused by the development of hydrodynamic instabilities in the melt. In addition, coefficient γ is supposed to depend on temperature and sulfur content in the metal (Figure 3). Theoretical approach proposed in [5] was used for its description. Boundary conditions to the problem are the next:

$$\mu \left.\frac{\partial u}{\partial r}\right|_{CD} = \frac{d\sigma}{dT}\left.\frac{\partial T}{\partial r}\right|_{CD}; \tag{10}$$

$$v\big|_{CD} = u\big|_{AB} = v\big|_{AB} = u\big|_{BC} = v\big|_{BC} = u\big|_{AD} = 0; \tag{11}$$

$$\lambda \left.\frac{\partial T}{\partial z}\right|_{CD} = \begin{cases} \dfrac{\eta Q}{\pi r_q^2}, r \le r_q \\ 0, r > r_q \end{cases}; \tag{12}$$

$$\left.\frac{\partial T}{\partial z}\right|_{AB} = \left.\frac{\partial T}{\partial r}\right|_{BC} = \left.\frac{\partial T}{\partial r}\right|_{AD} = 0. \tag{13}$$

Here Q, r_q are the laser power and beam radius respectively, η is the absorptivity coefficient. Computation region is a cylinder of radius L_r = 15 mm and of height L_z = 15 mm (Figure 4). Physical properties of the material and heat source parameters are summarized in Table 1. Constants appeared in momentum sink terms were chosen as $e_0 = 10^{-3}$ and $C = 10^6$. Phase change was assumed to occur in the temperature interval from $T_s = T_m - 25$K to $T_l = T_m + 25$K. It was also supposed that sulfur concentration in metal is 20 ppm.

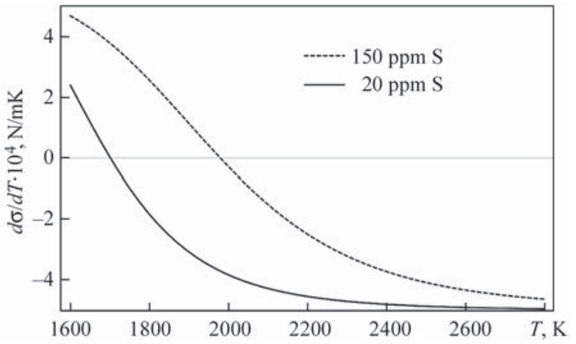

Figure 3. Surface tension temperature gradient for different sulfur contents

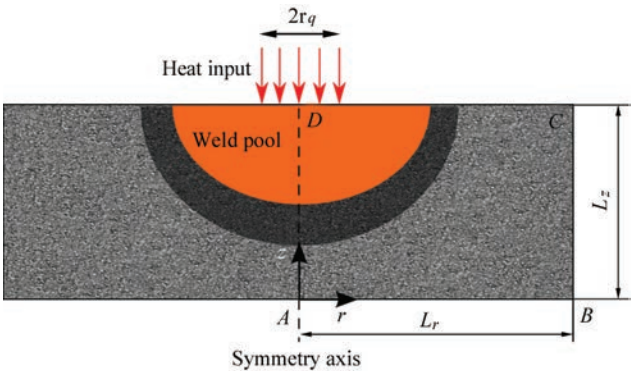

Figure 4. Computational domain

Properties of the Böhler S705 steel and laser beam settings

Density ρ, kg·m^{-3}	7200
Melting temperature T_m, K	1620
Dynamic viscosity μ, Pa·s	$6\cdot10^{-3}$
Heat capacity of liquid c_l, J·(kg·K)$^{-1}$	723.14
Heat capacity of solid c_s, J·(kg K)$^{-1}$	627
Thermal conductivity of solid λ_s, W/mK	22.9
Thermal conductivity of liquid λ_l, W/mK	22.9
Latent heat of fusion L, J·kg^{-1}	$2.508\cdot10^5$
Power of heat source Q, kW	5.2
Laser beam radius r_q, mm	1.4
Laser absorptivity η	0.13
Enhancement factor f,	7

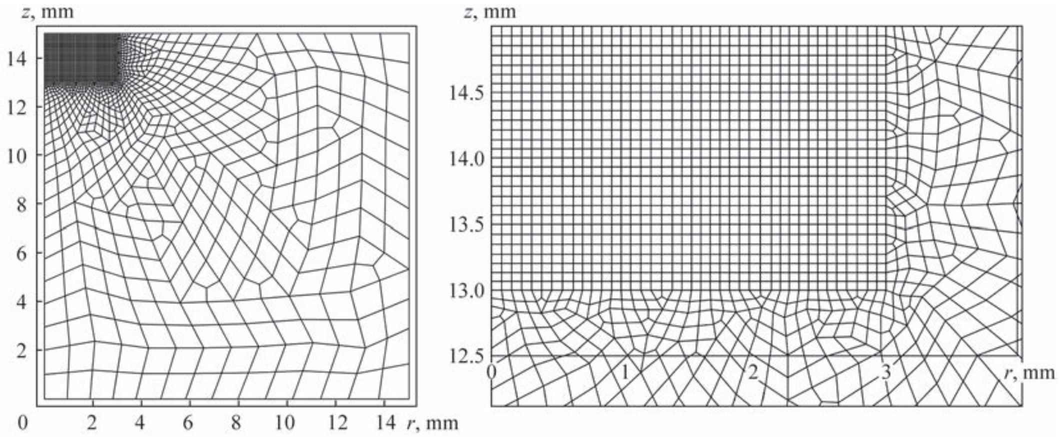

Figure 5. Adaptive finite element tessellation of computational domain

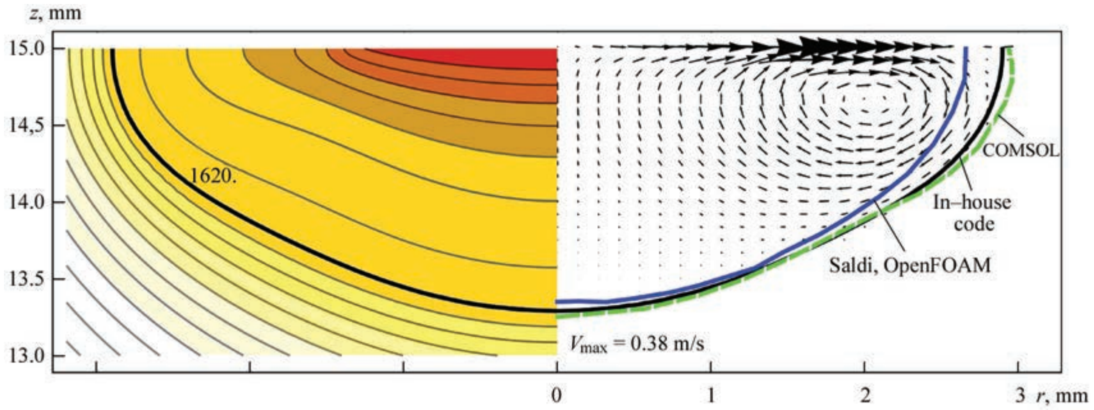

Figure 6. Melting front position and velocity field at t = 5 s

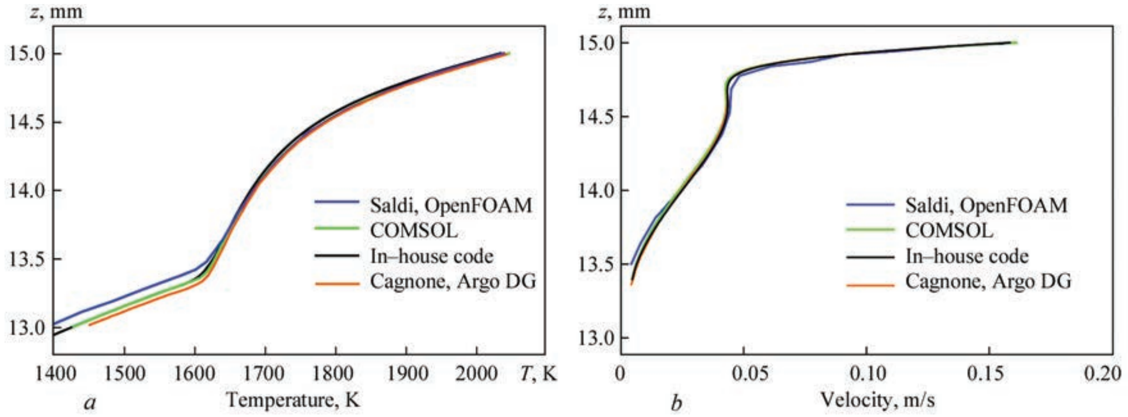

Figure 7. Temperature (a) and absolute velocity (b) distributions in section r = 1 mm at t = 5 s

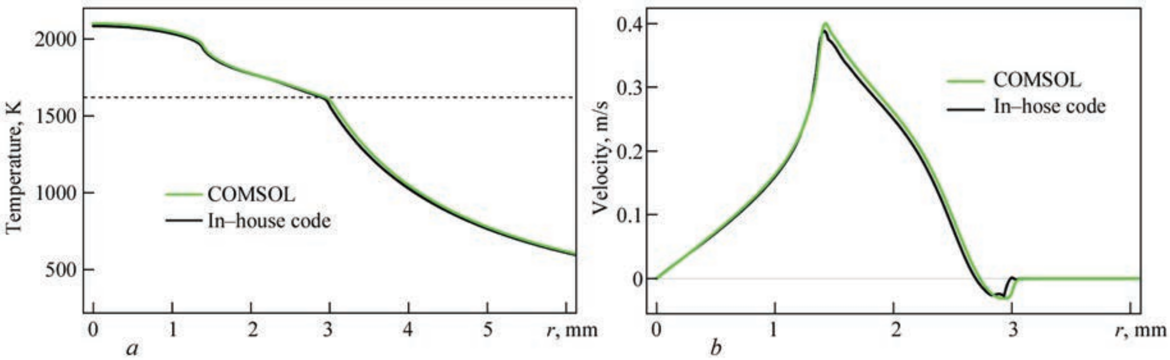

Figure 8. Temperature (a) and velocity (b) distributions along free surface at t = 5 s

Adaptive FE mesh with gradually increasing linear element dimension from 75 μm (in weld pool region) to 1.35 mm (on the periphery of computational region) was employed (Figure 5). We carried out calculations separately by means of two software tools: commercial software COMSOL Multiphysics and in-hose FE code. We fulfilled comparative analysis of calculated results at $t = 5$ s. Comparisons of the melt front shapes, velocity and temperature distributions along line $r = 1$ mm and on weld pool free surface are presented on Figure 6–8 respectively. Slight difference between our results and those obtained in work [13] for melt front position is observed (Figure 6), whereas in the melt region all the calculated results agree well with each other. Flow pattern in the weld pool consists of clockwise vortex in the meridional plane. Velocity in the melt achieves maximum value of 0.38 m/s. Increasing of sulfur content in the metal results in enlargement of the temperature interval where $\gamma > 0$ (Figure 3), which in turn leads to appearance of anti-clockwise vortex on the weld pool periphery under the influence of inward shear stress. Such changes in the flow structure give rise to penetration growth. This phenomenon is well studied and is widely reported in literature [6, 7, 1, 13].

Summary

Two test problems dealing with thermocapillary convection were solved separately by means of commercial software COMSOL Multiphysics and in-hose FE code. Comparison of the calculated results with those published earlier was carried out. Good agreement between results obtained with benchmark solutions is observed. Thus, it can be concluded that FE codes in use can successfully be applied for numerical analysis of multiphysics phenomena in the weld pool.

1. Kou, S. (2002) *Welding metallurgy*. New Jersey, John Wiley&Sons.
2. Messler, Jr., Robert, W. (2008) *Principles of welding: Processes, physics, chemistry, and metallurgy*. New Jersey, John Wiley&Sons.
3. Limmaneevichitr, C., Kou, S. (2000) Visualization of Marangoni convection in simulated weld pools. *Welding J.*, 79(**5**), 126–135.
4. Tsai, M. C., Kou, S. (1989) Marangoni convection in weld pools with a free surface. *Int. J. for Numerical Methods in Fluids*, 9(**12**), 1503–1516.
5. Sahoo, P., Debroy, T., McNallan, M. J. (1988) Surface tension of binary metal–surface active solute systems under conditions relevant to welding metallurgy. *Metallurgical Transact.*, *B*, 19(**3**), 483–491.
6. Heiple, C.R. (1982) Mechanism for minor element effect on GTA fusion zone geometry. *Welding J.*, 61(**4**), 97–102.
7. Pitscheneder, W. et al. (1996) Role of sulfur and processing variables on the temporal evolution of weld pool geometry during multikilowatt laser beam welding of steels. *Ibid.*, 75(**3**), 71–80.
8. Kou, S., Sun, D.K. (1985) Fluid flow and weld penetration in stationary arc welds. *Metallurgical Transact.*, *A* 16, **1**, 203–213.
9. Demchenko, V. F., Krivtsun, I.V., Krikent, I.V., Shuba, I.V. (2017). Force interaction of arc current with self-magnetic field. *The Paton Welding J.*, **3**, 15–24. https://doi.org/10.15407/as2017.03.03
10. Brent, A.D., Vaughan R. Voller, K.T.J. Reid (1988) Enthalpy-porosity technique for modeling convection-diffusion phase change: Application to the melting of a pure metal. *Numerical Heat Transfer*, *Pt A: Applications*, 13(**3**), 297–318.
11. Zienkiewicz, O.C., Taylor, R.L. (2000) *The finite element method*. Vol. 3: Fluid dynamics. Oxford, Butterworth-Heinemann.
12. Gupalo, Yu P., Ryazantsev. Yu. S. (1988) Thermocapillary motion of a liquid with a free surface with nonlinear dependence of the surface tension on the temperature. *Fluid Dynamics*, 23(**5**), 752–757.
13. Saldi, Z. (2012) *Marangoni driven free surface flows in liquid weld pools*. Ph.D. Thesis, Delft University of Technology.
14. Cagnone, Jean Sébastien, Koen Hillewaert, Nicolas Poletz (2014) A discontinuous Galerkin method for multiphysics welding simulations. *Key Engineering Materials*. **611**. Transact. Tech Publications Ltd.

Received 10.12.2020

https://doi.org/10.37434/tpwj2021.01.05

INFLUENCE OF EXTERNAL ELECTROMAGNETIC FIELD ON PARAMETERS AND DEFECTS OF CRYSTAL LATTICE OF METAL OF WELDED JOINTS DURING UNDERWATER WELDING

S.Yu. Maksymov, O.M. Berdnikova, O.O. Prilipko, T.O. Alekseenko and **E.V. Polovetskyi**
E.O. Paton Electric Welding Institute of the NAS of Ukraine
11 Kazymyr Malevych Str., 03150, Kyiv, Ukraine. E-mail: office@paton.kiev.ua

A study of the influence of external electromagnetic field on the parameters and defects of a crystal lattice (dislocation) in the metal of welded joints of low-alloy steel produced under water was carried out. A mathematical model and software package for calculating density of welding and eddy currents in massive conductors, density of magnetizing currents on the surface of ferromagnetic bodies were developed, mathematical models were used to analyze distribution of electrodynamic forces in arc welding and external electromagnetic influence and evaluation of the developed mathematical models on adequacy and reliability of the obtained results was performed. It was established that an external electromagnetic influence improves the quality of the weld metal, which is very important in welding of critical structures operating in the water environment. It is shown that during underwater welding of joints and applying external electromagnetic influence in the metal of heat-affected-zone, a finer-grained substructure with a general decrease in dislocation density and its uniform distribution is formed. The estimates of the level of local inner stresses taking into account the peculiarities of distribution and dislocation density in structural components show that their maximum level is formed during welding without external electromagnetic influence along the boundaries of upper bainite laths in the places of long dislocation clusters — concentrators of local inner stresses. A low level of local inner stresses is observed in the metal of the welded joints produced on the conditions at application of external electromagnetic influence. This is facilitated by a general decrease in the dislocation density and their uniform distribution in the structural components of a lower bainite, which should provide crack resistance of welded joints. 19 Ref., 1 Table, 5 Figures.

Keywords: underwater welding, welded joints, external electromagnetic influence, microstructure, dislocation density, dislocation hardening, local inner stresses

Currently, underwater electric arc welding is an integral part of any repair or assembly works of metal structures in the water environment. As to the level of mechanical properties, the welds of modern underwater metal structures of critical purpose often should not be inferior to the welds produced on land. At the same time, physicochemical and metallurgical processes during underwater welding proceed in difficult, extreme conditions, which makes it difficult to produce high-quality joints.

One of the relevant and promising methods of improving the quality of welds under water is forced degassing of liquid metal in welding pool, for which external electromagnetic influence (EEI) is used. With the use of EEI the control of movement of liquid metal in the welding pool can significantly improve mechanical and physicochemical properties of welds, increase their corrosion resistance and reduce the level of porosity [1]. The analysis of literature data shows that regardless of the methods and conditions of welding, a certain range of parameters of electromagnetic influence on liquid metal exists, at which the maximum increase in technological and physicochemical properties of welded joints is achieved. Thus, in this range the regularities are revealed, that determine the conditions of EEI optimality.

The need in the technologies of using EEI for liquid metals and alloys determines the necessity of appropriate development of calculation methods and mathematical modeling. Currently, there are different approaches and methods of mathematical modeling for calculation of electromagnetic fields: finite difference method, finite element method, method of integral equations and other that are effeciently used applying computer technologies [2–5].

When modeling the processes that proceed during arc welding using EEI, one of the most important values is the density of eddy currents in massive bodies. These currents significantly affect the magnetic field of the inductor and, as a consequence, distribution of electrodynamic forces in the flows of the pool melt. The arc represents a conical shape conductor, in the

S.Yu. Maksymov — https://orcid.org/0000-0002-5788-0753, O.M. Berdnikova — https://orcid.org/0000-0001-9754-9478,
T.O. Alekseenko — https://orcid.org/0000-0001-8492-753X, E.V. Polovetskyi — https://orcid.org/0000-0002-8113-0434

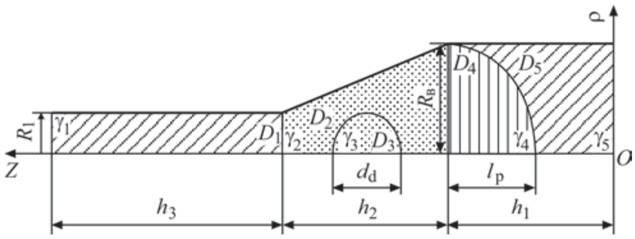

Figure 1. Scheme for calculation (h_1 — material thickness; h_2 — arc height; h_3 — electrode height; R_1 — electrode radius; R_p — pool radius; l_p — pool depth; d_d — drop diameter; D_1 — electrode diameter; D_2 — arc diameter; D_3 — drop diameter; D_4 — pool diameter; D_5 — material diameter; γ_1 — electrical conductivity of the electrode; γ_2 — electrical conductivity of the arc; γ_3 — electrical conductivity of the drop; γ_4 — electrical conductivity of the pool; γ_5 — electrical conductivity of the material)

volume of which there are drops of molten electrode metal. The following parameters are considered to be set: conductivity and shape of plasma, sizes and number of drops, conductivity of drop material and distance between them. The following assumptions were accepted: drops have a spherical shape and welding pool has a hemispherical shape [6–10].

The calculation model is presented in Figure 1.

Based on the model, an algorithm for mathematical modeling of magnetohydrodynamic processes in a liquid metal pool using EEI was developed, which simplifies the calculation process to optimize the technological process.

Moreover, there are several stages of modeling: it is necessary to develop a mathematical model and software package for calculating density of welding and eddy currents in massive conductors, density of magnetizing currents on the surface of ferromagnetic bodies, to apply the developed mathematical models for analyzing distribution of electrodynamic forces in arc welding at EEI, to carry out estimation of the developed mathematical models on adequacy and reliability of the obtained results.

The sequence of all stages of modeling according to the developed algorithm is the following:

1. We set geometric dimensions and electrophysical properties of the system.
2. We set welding current and current in the inductor of external magnetic influence.
3. We solve the system of integral equations and find the distribution of charges.
4. Based on the found we find the components of the field and density of the welding current.
5. We solve the system of integral equations and find eddy and magnetizing currents.
6. Based on the found we find the induction of EEI.
7. We determine the average density of electrodynamic forces for the period.
8. We evaluate the speed of the melt movement and the model correctness.

Based on the proposed algorithm, a special software in Delphi 7 language was developed.

Using the proposed model, it is possible to model different cases of thermophysical parameters of underwater welding. At the same time there is an opportunity to model a variety of options without a large number of options of experimental welding which are rather difficult to be carried out in laboratory conditions.

By conducting a series of numerical experiments, an optimized EEI mode was revealed and a series of experimental welds in real conditions of water environment were performed. The metal structure of welded joints with the use of EEI and without its use was further investigated and X-ray diffraction phase analysis was performed in DRON-1 diffractometer in a cobalt radiation. It was shown that during welding with EEI, in the weld metal and heat-affected-zone (HAZ) there is a BCC-solid solution of α-Fe.

Figure 2 shows the dependence of the parameters of a crystal lattice of solid solutions, which were revealed in the studied areas of the metal of welded joints. The difference between the values of the experimental parameters of a crystal lattice of BCC-solid solutions of the weld metal (Figure 2, *a*) and HAZ (Figure 2, *b*), produced after underwater welding

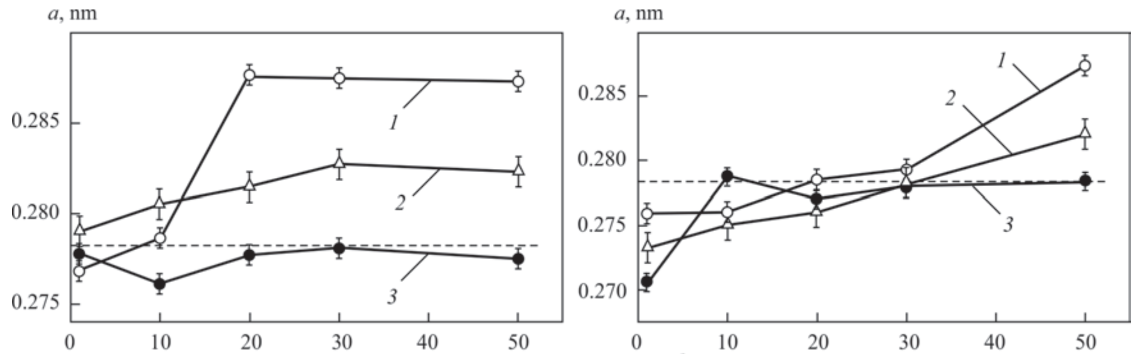

Figure 2. Change in the parameter of a crystal lattice α of BCC-solid solutions of weld metal (*a*) and HAZ (*b*) depending on the depth of underwater welding: *1* — experiment without EEI; *2* — experiment with EEI; *3* — calculation. Dashed line shows the value of a crystal lattice parameter of the weld metal

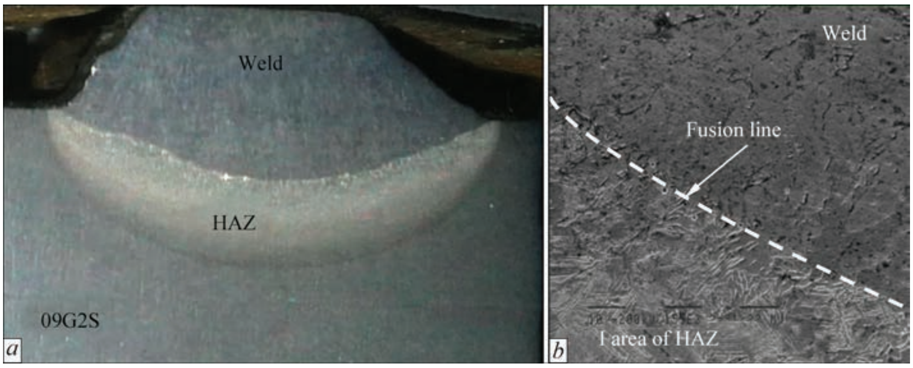

Figure 3. Macrostructure of welded joint (*a*) and microstructure of metal in the area of fusion line and I area of HAZ (*b*, ×1550)

without and with the use of EEI, confirms its effect on formation of the structure.

With an increase in welding depth to 50 m, the parameter of a crystal lattice (*a*) of the weld metal under the condition of using EEI increases slightly (up to 1 %) as compared to the specimens without the use of EEI, where the parameter of a crystal lattice changes more significantly (up to 4 %). In the HAZ (Figure 2, *b*) up to a depth of 30 m, the parameter of a crystal lattice for all cases remains almost the same, but without the use of EEI with an increase in the depth of welding to 50 m, the parameter α increases.

Thus, EEI, which is used in underwater welding, helps to homogenize the metal structure of a welded joint, namely, to reduce the difference as to the parameter of a crystal lattice both between the zones of the welded joint itself as well as between the base material and welded joint. This should provide a uniform level of mechanical properties on the areas of welded joints and its crack resistance [11–16].

The obtained results indicate that the use of EEI reduces the degree of degradation of the weld metal and HAZ structure under the action of water environment and hydrostatic pressure.

It is known that one of the important imperfections of a crystal lattice is its defects — dislocations, around which elastic zones of curvature of a crystal lattice are formed [11–14]. The distribution of dislocations, their density and nature of dislocation structure have an impact on mechanical properties of the metal [5, 12, 17]. When a magnetic field is applied, the dislocation system becomes unstable, which leads to a redistribution of crystal lattice defects and can lead to a mutual annihilation of dislocations and a decrease in inner stresses. Also, point defects can interact with each other. If the vacancy and interstitial atom are joined, then both defects are annihilated, and the atom that was previously interstitial, occupies a normal position in the lattice [18, 19]. Based on the abovementioned, the furhter analysis of processes occurring in the specimens at EEI on the level of fine structure was carried out.

Investigations of the dislocation structure were performed by the methods of transmission electron microscopy (TEM, JEM-200CX microscope of JEOL Company, Japan). As a result of the carried out work, experimental data on the complex of structural parameters formed in HAZ of welded joints of steel 09G2S in the area of overheating were obtained (Figure 3, I area of HAZ). During TEM investigations, the following structures were studied: lower bainite (B_l), upper bainite (B_u) and their parameters — width of lath structures and distribution of dislocation density (ρ) in the structural components.

Detailed studies of the metal microstructure of HAZ overheating area of the specimen using TEM method without the use of EEI showed that the size (width) of laths of an upper bainite (B_u) is 0.2–1.0 μm (Figure 4, *a*, *b*). In the inner volumes of the lath structure of an upper bainite, the distribution of dislocation density is nonuniform. The dislocation density varies from $\rho = (2–4)\cdot10^{10}$ cm^{-2} to $\rho = (5–6)\cdot10^{10}$ cm^{-2} at the maximum values $\rho = (8–10)\cdot10^{10}$ cm^{-2} (Figure 4, *b*). Such dislocation clusters-zones of deformation localization with a higher dislocation density are formed along the coarse-lamellar structures of an upper bainite with a lath size of 0.5–1.0 μm, which are formed in the overheating area at a distance of up to 200 μm from the fusion line. The width of the localized deformation zones is 0.15–0.25 μm. The structure of a lower bainite is more dispersed with a lath size of 0.1–0.4 μm (Figure 4, *c*). The distribution of dislocation density in the inner volumes of the lath structure of B_l has a gradient-free nature at $\rho = (1–4)\cdot10^{10}$ cm^{-2}.

The studies of the specimen with the use of EEI showed that the width of laths of an upper bainite is mainly 0.4–0.8 μm and more dispersed is 0.1–0.3 μm (Figure 4, *d*). In the inner volumes of an upper bainite structure, the dislocation density varies from $\rho = (1.8–2.8)\cdot10^{10}$ cm^{-2} to $\rho = 3\cdot10^{10}$ cm^{-2} (Figure 4, *d*). The structure of a lower bainite (as well as in the specimen without EEI) of more dispersed sizes is 0.1–0.4 μm. The distribution of dislocation density in

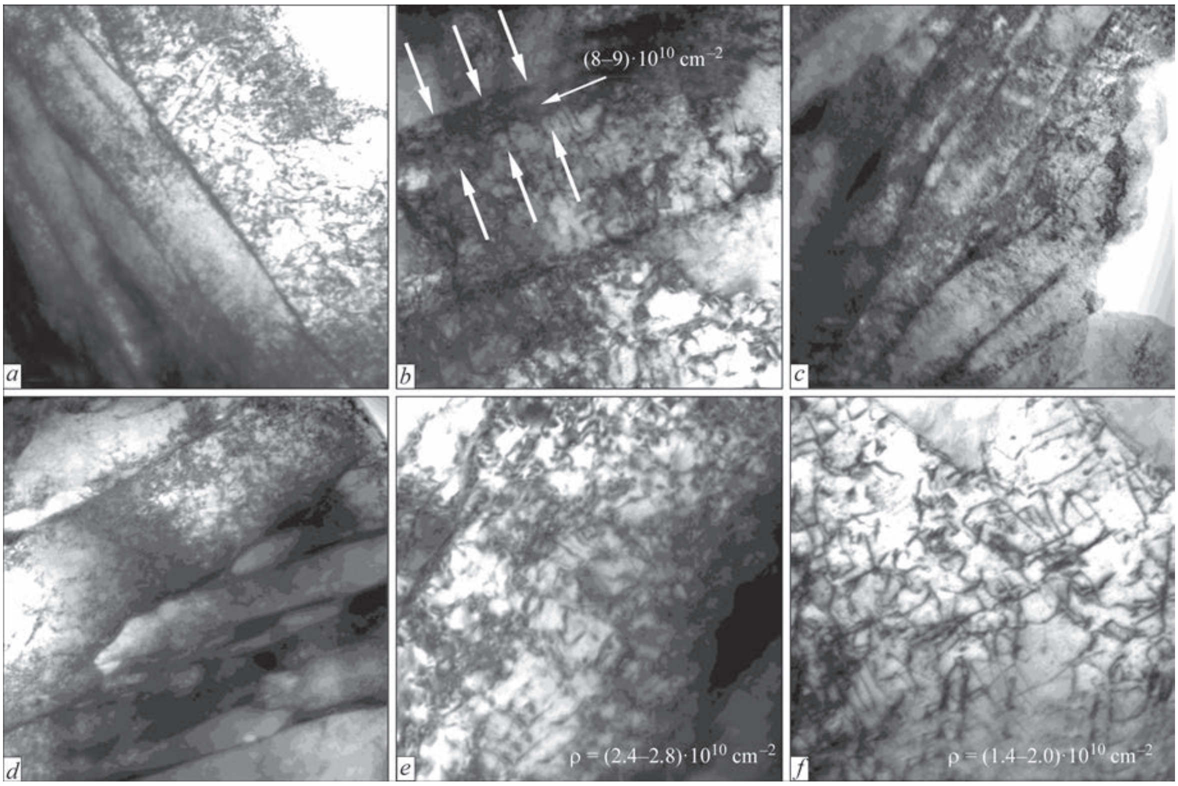

Figure 4. Fine structure of upper (*a*, ×52000; *b*, ×52000; *d*, ×25000; *e*, ×70000) and lower bainite (*c*, ×52000; *f*, ×70000) in the area of overheating of HAZ of welded joints during underwater welding: *a–c* — without the use of EEI; *d–f* — with the use of EEI

the inner volumes of B_l is uniform and varies from $\rho = (1–2)\cdot 10^{10}$ cm^{-2} to $\rho = 3\cdot 10^{10}$ cm^{-2} (Figure 4, *e*).

Comparing the parameters of the fine structure of the studied specimens, it was found that in the metal without the use of EEI the largest gradients in the size of lath structures of upper bainite and dislocation density are observed, which will lead to a nonuniform level of mechanical properties of the metal, increase local inner stresses and accordingly, reduce crack resistance. In the metal at application of EEI, refinement of the structure at the general decrease and uniform distribution of dislocation density in the volume of structural components is observed that will provide strength and crack resistance of metal.

Therefore, in view of the abovementioned, it appears to be advisable to analyze the dislocation strengthening ($\Delta\sigma_d$) predetermined by interdislocation interaction in the structure of an upper (B_u) and lower bainite (B_l). Quantitative evaluation of dislocation strengthening, according to the theories of deformation strengthening [12–14], was performed according to the following dependence: $\Delta\sigma_d = \alpha G b \rho^{1/2}$, MPa, [15], where α is the coefficient for steel — 0.5; b is the Burgers vector for steel — $2.5\cdot 10^{-7}$ mm [12].

Analytical estimates of dislocation strengthening in the structure of B_u show that in the metal of HAZ overheating area during underwater welding without the use of EEI, the following is observed: the largest gradients in dislocation density in volume and along the boundaries of B_u, which lead to 2–3 times increase in a local level of dislocation strengthening from $\Delta\sigma_d = 101$ MPa to $\Delta\sigma_d = 300$ MPa (Figure 5, *a*, Table).

In the metal of the area of HAZ overheating with the use of EEI a uniform distribution of dislocation density is observed, gradients on the dislocation density are absent and, accordingly, the level of dislocation strengthening is uniform ($\Delta\sigma_d = 136–175$ MPa) (Figure 5, *b*, Table).

The next step in the study of the influence of structure on the properties of welded joints metal was to identify a true real picture of the zones of distributing local inner stresses ($\tau_{i.s.}$), i.e. stress concentrators, the values of these characteristics of the metal state, and the dynamics of their change during underwater welding and the use of EEI. The set problem is of key importance, because the processes of delayed fracture, formation of the source of crack initiation and propagation begin directly from the initiation of inner stress concentrators [16–19].

As far as the distribution and level of local inner stresses and strains can be determined only on the basis of true pictures of the dislocation density distribution, namely this information was provided using the TEM method. Estimation of the level of local inner stresses depending on structural factors was determined on density and distribution of dislocations according to the known dependence for $\tau_{i.s.}$ [19]: $\tau_{i.s.} = Gbh\rho/\pi(1 - \nu)$, where G is the shear modulus;

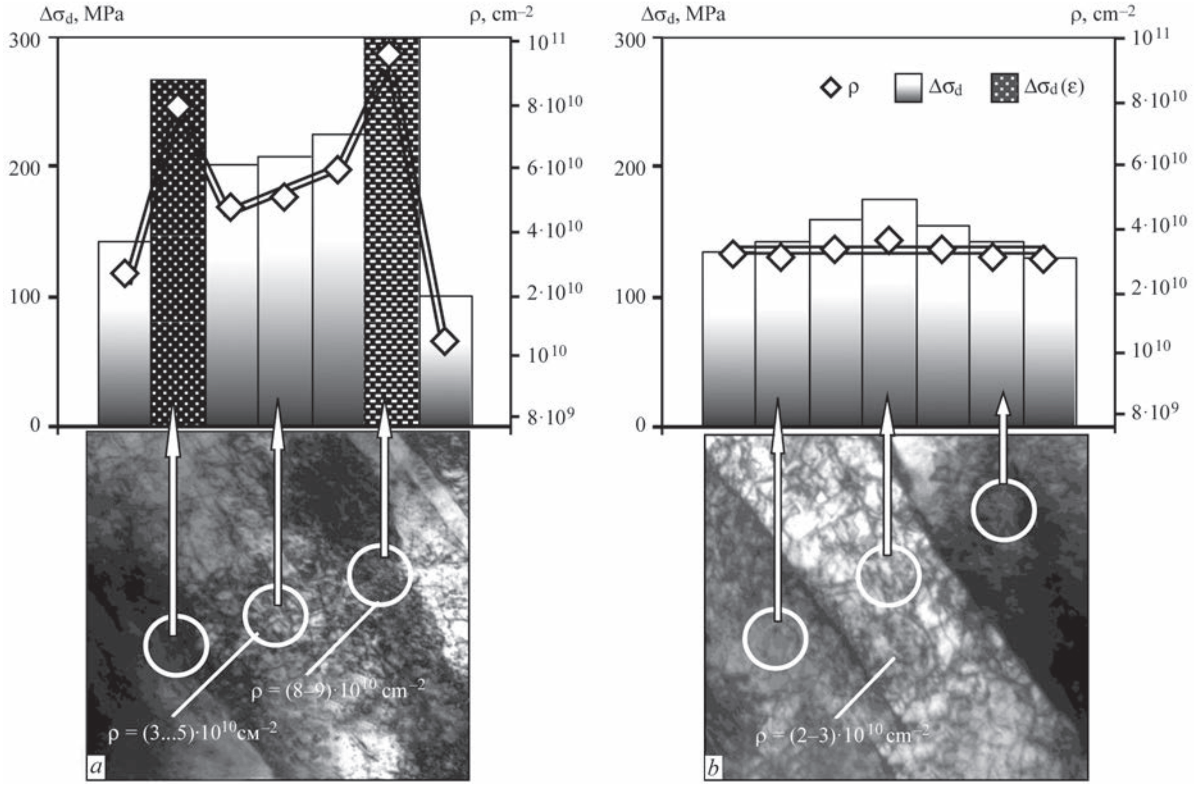

Figure 5. Fine structure of upper (*a*, ×70000) and lower bainite (*b*, ×70000) and, accordingly, change in dislocation density (ρ), dislocation strengthening ($\Delta\sigma_d$) in inner volumes and in the zones of deformation localization (ε): *a* — without the use of EEI; *b* — with the use of EEI

Parameters of fine structure of HAZ metal of welded joints

Parameters	Presence of EEI			
	Without the use of EEI		With the use of EEI	
	Structure			
	B_l	B_u	B_l	B_u
ρ (min), cm^{-2}	$(1–2)\cdot10^{10}$	$(2–4)\cdot10^{10}$	$(1–2)\cdot10^{10}$	$(1.8–2.4)\cdot10^{10}$
ρ (max), cm^{-2}	$(3–4)\cdot10^{10}$	$(4.5–6)\cdot10^{10}$ $(8–9)\cdot10^{10*}$	$3\cdot10^{10}$	$3\cdot10^{10}$
$\Delta\sigma_d$ (min), MPa	101–141	141–200*	101–141	136–155
$\Delta\sigma_d$ (max), MPa	175–200	212–245 282–300*	175	175
*In the areas of deformation localization (ε).				

b is the Burgers vector; h is the thickness of the foil ($2\cdot10^{-5}$ cm); ν is the Poisson's ratio; ρ is the dislocation density.

Analytical estimates of the level of local inner stresses show that the maximum values of $\tau_{i.s.}$ = = 1294–1665 MPa = $(0.15–0.2)\cdot\tau_{theor}$ (from the theoretical strength) are formed in places of long dislocation clusters — along the boundaries of B_u during welding under water without the use of EEI. This can lead to a decrease in crack resistance and brittle fracture of welded joints throughout the metal of the overheating area of HAZ of welded joints.

Low values of $\tau_{i.s.}$ = 185–554 MPa = $(0.02–0.07)\cdot\tau_{theor}$ are typical for welded joints produced under the conditions with the use of EEI. This is facilitated by the reduction in dislocation density with its uniform distribution, which, accordingly, will provide crack resistance of welded joints.

Conclusions

1. Mathematical model and software package for calculating density of welding and eddy currents in massive conductors to optimize the conditions of external electromagnetic influence were developed.

2. The use of external electromagnetic influence reduces the degree of degradation of the metal structure of welded joints under the action of water environment and hydrostatic pressure.

3. In underwater welding, external electromagnetic influence helps to reduce the difference in the parameter of a crystal lattice (α) of the metal along the areas of the welded joint and relative to the base metal.

4. Applying the method of transmission electron microscopy, the structural-phase changes in the metal of the HAZ overheating area of low-alloy steel joints during underwater welding without the use of external electromagnetic influence and during its application were studied. It was established that the structure of a lower and upper bainite, formed in the metal of the HAZ overheating area differs in the parameters of such structural components as sizes of the lath substructure, distribution and dislocation density.

5. During underwater welding without the use of external electromagnetic influence, the structure of an upper bainite has mainly a coarse-lamellar nature at a general increase in the dislocation density and its nonuniform distribution both in the volume as well as along the boundaries of the laths in the zones of a localized deformation. This leads to an increase in dislocation strengthening in the local areas of the structure in the location of long dislocation clusters, and, accordingly, a nonuniform level of mechanical properties and the formation of concentrators of local inner stresses.

6. At external electromagnetic influence in the metal of a heat-affected-zone, substructure refinement, redistribution of defects of a crystal lattice (dislocations) at a general decrease in dislocation density and its uniform distribution is observed. This contributes to a uniform level of strengthening, decrease in the level of local inner stresses in the volume of structural-phase components of the metal and along their boundaries and provides crack resistance of welded joints during underwater welding.

1. Ryzhov, R.N., Kozhukhar, V.I., Maksimov, S.Yu., Prilipko, E.A., (2004) Application of external electromagnetic actions for improvement of mechanical properties of welds in underwater wet welding. *The Paton Welding J.*, **11**, 49–51.
2. Grinberg, G.A. (1948) *Selected problems of mathematical theory of electric and magnetic phenomena.* Moscow, AN SSSR [in Russian].
3. Tozoni, O.V. (1964) *Mathematical models for calculation of electric and magnetic fields.* Kiev, Naukova Dumka [in Russian].
4. Tozoni, O.V., Fedchun, L.V. (1964) Calculation of magnetic field of nonsaturated machines by method of integral equations. *Izv. Vuzov. Elektromekhanika*, **5**, 471–478 [in Russian].
5. Gulyaev, A.P. (1986) *Metals science*. Moscow, Metallurgiya [in Russian].
6. Savich, I.M., Kareta, N.L., Grishanov, A.A., Sladkova, V.N. (1982) Influence of cooling rate on distortion of crystal lattice in welding under water and in air. *Avtomatich. Svarka*, **5**, 8–9 [in Russian].
7. Larikov, L.N., Falchenko, V.M., Gertsriken, D.S., Khrenov, K.K. (1978) On mechanism of influence of pulsed magnetic field on atomic mobility in iron and aluminium. *Dokl. AN SSSR*, 239(**2**), 312–314 [in Russian].
8. Larikov, L.N. (1980) *Healing of defects in metals*. Kiev, Naukova Dumka [in Russian].
9. Gertsriken, D.S., Dekhtyar, I.Ya. (1960) *Diffusion in metals and alloys in solid phase*. Moscow, Fizmatgiz [in Russian].
10. Larikov, L.N., Falchenko, V.M., Mazanko, V.F. et al. (1975) Anomalous acceleration of diffusion in pulsed loading of metals. *Dokl. AN SSSR*, 221(**5**), 1073–1075 [in Russian].
11. Olemskoj, A.I., Panin, V.E., Petrunin, V.A. (1986) Mixed states and physical mechanics of defects in strongly excited crystals. *Izv. Vuzov. Fizika*, **2**, 20–27 [in Russian].
12. Goldshtejn, M.I., Litvinov, V.S., Bronfin, B.M. (1986) *Physics of metals*. Moscow, Metallurgiya [in Russian].
13. Kozlov, E.V., Koneva, N.A., Popova, N.A. (2009) Grain structure and geometrically required dislocations and particles of secondary phases in polycrystals of micro- and mesolevels. *Fizicheskaya Mezomekhanika*, 12(**4**), 93–106 [in Russian].
14. Farber, V.M., Belenky, B.Z., Goldshtejn, M.I. (1975) Evaluation of strength of low-carbon low-alloyed steels on structural data. *Fizika Metallov i Metallovedenie*, 3(**2**), 403–409 [in Russian].
15. Farber, V.M., Selivanova, O.V. (2001) Classification of stress relaxation processes and their manifestation in plastic deformation of metals. *Metally*, **1**, 110–115 [in Russian].
16. Berdnikova, O., Pozniakov, V., Bernatskyi, A. et al. (2019) Effect of the structure on the mechanical properties and cracking resistance of welded joints of low-alloyed high-strength steels. *Procedia Structural Integrity*, **16**, 89–96.
17. Markashova, L.I., Poznyakov, V.D., Berdnikova, E.N. et al. (2017) Structure and service properties of welded joints of high-strength steels, aluminium and titanium alloys. *The Paton Welding J.*, **7**, 6–14. https://doi.org/10.15407/tpwj2017.07.02
18. Markashova, L.I., Poznyakov, V.D., Shelyagin, V.D. et al. (2018) Effect of metal structure on service properties of high-strength steel welded joints produced using different methods of welding. *The Paton Welding J.*, **2**, 7–13. DOI: https://doi.org/10.15407/tpwj2018.02.02
19. Markashova, L.I., Poznyakov, V.D., Gaivoronskii, A.A. et al. (2011) Estimation of the strength and crack resistance of the metal of railway wheels after long-term operation. *Fiz.-Khim. Mekh. Mater.*, 47(**6**), 73–79 [in Russian].

Received 16.12.2020

https://doi.org/10.37434/tpwj2021.01.06

NUMERICAL ANALYSIS OF THE FEATURES OF LIMITING STATE OF WELDED PIPELINE ELEMENTS UNDER ULTRA-LOW-CYCLE LOADING CONDITIONS

O.V. Makhnenko, O.S. Milenin, O.A. Velykoivanenko, G.P. Rozynka and **N.I. Pivtorak**
E.O. Paton Electric Welding Institute of the NAS of Ukraine
11 Kazymyr Malevych Str., 03150, Kyiv, Ukraine. E-mail: office@paton.kiev.ua

Expert analysis of the reliability and performance of welded pipelines with detected corrosion-erosion damage under ultra-low-cycle loading requires taking into account several interrelated physicomechanical phenomena, which determine the limiting state of a specific structure. For this purpose, integrated numerical procedure was developed in this study for finite-element assessment of subcritical fracture accumulation and prediction of the limiting state of typical pipelines with 3D defects of wall thinning. The ductile mechanism of subcritical fracture was considered as the main one. Moreover, material hardening and softening at plastic deformation (strain hardening, Bauschinger effect) was taken into account. This integrated approach allowed revealing the main regularities of failure of a typical pipeline element, depending on external loading. 14 Ref., 7 Figures.

Keywords: welded pipeline, corrosion-erosion defect, ultra-low-cycle loading, Bauschinger effect, ductile fracture, limiting state

Numerical assessment of residual strength of pipeline elements (PE) with detected corrosion-erosion losses of metal is a characteristic problem at expert analysis of the reliability of various industrial systems. A generally accepted approach to solution of this problem is evaluation of the limiting state of a specific structure at nominal service load. As the majority of pipelines are welded, the impact of the residual stress-strain state (SSS) should be taken into account, if metal losses are in the welding zone. This problem is well studied for static loading (for instance, by internal pressure) [1–3], whereas for cyclic force impact the spatial inhomogeneity and interrelation of physicomechanical processes, which cause subcritical damage and failure of material, require a considerable conservatism of the respective analytical methods. In particular, ultra-low-cycle fatigue differs by considerable plastic flow of the material that requires taking into account its strain hardening, softening by Bauschinger effect and initiation of ductile fracture pores [4]. Presence of the welded joint and local geometrical anomalies of the structure (service defects of corrosion-erosion loss of metal) determines the features of the stress-strain state of pipeline elements under the impact of internal pressure and/or bending moment and influences the fracture resistance.

In this work the characteristic features of subcritical damage accumulation and limiting state of welded pipelines with corrosion-erosion metal loss at ultra-low-cycle loading were studied on the base of finite-element prediction.

Mathematical model of the kinetics of welded PE state under the impact of static and cyclic loading. Limiting state of corroded (eroded) PE depends on a range of physicomechanical processes, initiated by operational and technology impact. In the case of a significant deformation under cyclic loading (for instance, earthquake, landslide, overload, stability loss, etc.) the limiting state of the pipeline is determined by development of plastic strains and respective accumulation of subcritical damage right up to initiation of a macrodefect. Local metal losses and respective mechanical stress raisers lead to a certain lowering of PE load-carrying capacity under pressure. Their admissibility is determined by the respective standard norms for design operation conditions. However, ultra-low-cycle loading (number of cycles from 10 to 100) leads to extraordinary modes of pipeline operation that complicates expert analysis of their compliance with design requirements. The main complexity consists in the nonlinear reaction of the material to cyclic plastic deformation and development of its properties. Thus, alongside the characteristic strain hardening two possible mechanisms of material softening can be singled out: Bauschinger effect due to a change in plastic strain direction and accumulation of ductile fracture porosity with concurrent reduction of the load-carrying net cross-section of the structure [5]. Presence of welds causes spatial heterogeneity of

O.V. Makhnenko — https://orcid.org/0000-0002-8583-0163, O.S. Milenin — https://orcid.org/0000-0002-9465-7710

SSS and complex interaction of operational and residual stresses. This should be also taken into account, particularly in the case of close proximity of metal loss area and weld.

In the absence of sharp-angled geometrical stress raisers, the prevailing mechanism of violation of material integrity is ductile failure, which consists in initiation of uniformly distributed pores [6]. In order to predict their initiation at plastic flow of material in nonisothermal cases, it is proposed to use the deformation criterion, in keeping with which initial porosity with bulk concentration f_0 appears in a certain volume of metal at fulfillment of the following condition:

$$\int \frac{d\varepsilon_i^p}{\varepsilon_c(T)} > 1, \tag{1}$$

where $d\varepsilon_i^p = \sqrt{2}\big/3\sqrt{d\varepsilon_{ij}^p d\varepsilon_{ij}^p}$ is the intensity of plastic strain increment; $\varepsilon_c(T)$ is the critical value of plastic strains; $i, j = r, \beta, z$ are the coordinates in the cylindrical system of coordinates (Figure 1).

Further increase of the concentration of ductile fracture pores during plastic deformation of metal, in particular, at static or cyclic loading in service, corresponds to Rice–Tracey law [7]:

$$df = \begin{cases} 1.28\exp\left(\frac{3}{2}\frac{\sigma}{\sigma_i}\right)d\varepsilon_i^p, \text{ if } \frac{\sigma}{\sigma_i} > 1 \\ 1.28\left(\frac{\sigma}{\sigma_i}\right)^{1/4}\exp\left(\frac{3}{2}\frac{\sigma}{\sigma_i}\right)d\varepsilon_i^p, \text{ if } \frac{1}{3} \le \frac{\sigma}{\sigma_i} \le 1 \end{cases}, \tag{2}$$

Mathematical treatment of the joint problem of temperature field kinetics in welding, SSS development and micropore formation is based on finite-element description using eight-node finite elements (FE). Increment of strain tensor was presented as a sum of the respective components [8]:

$$d\varepsilon_{ij} = d\varepsilon_{ij}^e + d\varepsilon_{ij}^p + \delta_{ij}\left(d\varepsilon_T + df/3\right), \tag{3}$$

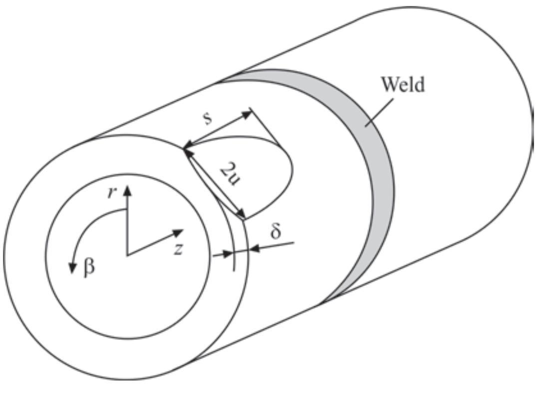

Figure 1. Scheme of a section of defective pipeline in the cylindrical system of coordinates

where $d\varepsilon_{ij}^e$, $d\varepsilon_{ij}^p$, $\delta_{ij}d\varepsilon_T$, $\delta_{ij}df/3$ are the components of increment of strain tensor due to elastic deformation mechanism, deformations of instantaneous plasticity, kinetics of heterogeneous temperature field and porosity, respectively.

Proceeding from the above-said, the strain tensor increments can be represented in the form of superposition of increments of the respective components:

$$\Delta\varepsilon_{ij} = \Psi\left(\sigma_{ij} - \delta_{ij}\sigma\right) + \delta_{ij}\left(K\sigma + \Delta\varepsilon_T + \Delta f/3\right) - \frac{1}{2G}\left(\sigma_{ij} - \delta_{ij}\sigma\right)^* - \left(K\sigma\right)^*, \tag{4}$$

where «*» symbol refers the respective variable to the previous tracing step; Ψ is the material state function, which determines the plastic flow conditions according to Mises criterion, additionally taking into account the reduction of the load-carrying net cross-section of the finite element as a result of discontinuity formation within Gurson–Tvergaarten–Needleman model [9]:

$$\begin{gathered} \Psi = \frac{1}{2G}, \text{ if } \sigma_i < \sigma_s = \\ = \sigma_y\sqrt{1 + \left(q_3 f'\right)^2 - 2q_1 f'\cosh\left(q_2\frac{3\sigma}{2\sigma_y}\right)}, \\ \Psi > \frac{1}{2G}, \text{ if } \sigma_i = \sigma_s, \\ \text{state } \sigma_i > \sigma_s \text{ is invalid.} \end{gathered} \tag{5}$$

Determination of Ψ function is performed by iteration at each step of numerical tracing (by time or load increment) within the finite-element solution of the boundary problem of nonstationary thermoplasticity that allows solving the nonlinearity problem by the material plastic flow, allowing for its subcritical damage [10]. The main difficulty in modeling the cyclic loading consists in that small changes in the state of metal in one loading cycle, namely accumulation and increase of subcritical damage, cause a change in the yield surface and a respective change of plastic deformation loop. However, at each loading step it is necessary to determine the equilibrium state of damage and the respective distribution of stresses and strains. For this purpose, proceeding for the assumption that the stationary state is characterized by a negligibly small rate of increase of ductile fracture pore volume, it is proposed to conduct the following iteration process by Ψ_k function:

$$F = \begin{cases} F + dF, \text{ if } f_0 K_1 \exp\left(K_2\frac{\sigma}{\sigma_i}\right)d\varepsilon_i^P = \\ = \Psi_k \le \Psi_k^0 \approx 10^{-5}; \\ F, \text{ if } \Psi_k > \Psi_k^0, \end{cases} \tag{6}$$

where F is the system of external force loads acting on the structure; dF is the increment of force loads during numerical tracing; K_1, K_2 are the constants.

Strain hardening of the metal affects the shape of Mises yield surface, which, depending on the intensity of the accumulated plastic strains, is usually considered in the following form [11]:

$$\sigma_T = \sigma_T^0 \left[1 + c_1 \ln\left(\frac{\dot{\varepsilon}^p}{\dot{\varepsilon}_0}\right) + c_2 \left\{ \ln\left(\frac{\dot{\varepsilon}^p}{\dot{\varepsilon}_0}\right) \right\}^2 \right] \times \left[1 + \left(\frac{\varepsilon^p}{\varepsilon_0}\right) \right]^m, \qquad (7)$$

where $c_1 = 2.149 \cdot 10^{-3}$; $c_2 = 9.112 \cdot 10^{-2}$; $\varepsilon_0 = 1.540 \cdot 10^{-4}$, $m = 0.14$ are the constants; dot above a variable denotes time differentiation.

If it is necessary to take into account the change of plastic deformation direction (for instance, at variable static loading that causes an alternating cycle of plastic deformation), a model of kinetic strengthening of the material was used in the following form [12]:

$$\sqrt{\frac{3}{2}\left(\sigma_{ij} - \delta_{ij}\sigma - \bar{X}\right)\left(\sigma_{ij} - \delta_{ij}\sigma - \bar{X}\right)} - \sigma'_T(f')\left[1 + \left(\varepsilon^p/\varepsilon_0\right)\right]^M \le 0, \qquad (8)$$

where $\sigma'_T(f')$ is the current true yield strength of the damaged material in keeping with (9); M, ε_0 are the material constants; $\bar{X}$ is the shear tensor:

$$\bar{X} = \operatorname{sign}\left(\varepsilon^p\right)\frac{C}{\gamma} + \left[X_0 - \operatorname{sign}\left(\varepsilon^p\right)\frac{C}{\gamma}\right] \times \exp\left[-\operatorname{sign}\left(\varepsilon^p\right)\left(\varepsilon^p - \varepsilon_0^p\right)\right]. \qquad (9)$$

Proceeding from a specific value of Ψ function, the strain field at each loading stage is determined from (5), taking into account $\sigma_s(T, \varepsilon^p)$ dependence. The components of stress tensor satisfy the statics equation for internal FE and boundary conditions for surface FE. In their turn, the components of $\Delta U_i = (\Delta U, \Delta V, \Delta W)$ vector satisfy the respective conditions on the boundary. The solved system of equations in variables of the vector of displacement increments in FE nodes is determined at each step of tracing and iterations by $\Psi(\Psi_k)$ by minimizing the following functional [13]:

$$E_I = -\frac{1}{2}\sum_V \left(\sigma_{ij} + J_{ij}\right)\Delta\varepsilon_{ij} V_{m,n,r} + \sum_{S_P} F_i \Delta U_i \Delta S_P^{m,n,r}, \qquad (10)$$

where $\sum_V$ is the operator of the sum of inner FE; $\sum_{S_P}$ is the operator of the sum of surface FE, on which the components of force vector F_i are assigned.

A criterion for initiation of macrodefectiveness of PE material, is fulfillment of one of the three fracture conditions [14]:

$$\Psi \ge \frac{1}{2G} + \frac{\varepsilon_f - \left(\varepsilon_i^p\right)^*}{1.5\sigma_s\left(\varepsilon_i^p\right)};$$

$$f' \ge f_F = \frac{1}{q_1}\exp\left(-\frac{3q_2\sigma_m}{2\sigma_Y}\right); \qquad (11)$$

$$\frac{\sigma_1}{1 - 2f/3} > S_K,$$

where ε_f is the ultimate strain which, in the general case, depends on the stressed state rigidity; S_K is the microcleavage stress; q_1, q_2 are the constants.

If the above-mentioned process of loss of FE load-carrying capacity proceeds at this loading stage, covering an ever greater number of neighbouring FE, and does not allow moving to the next loading step then this step determines the boundary loading of «spontaneous failure».

Results and discussion. As was noted above, residual SSS in the weld area, kinematic hardening and ductile fracture affect the limiting state of the effective PE at ultra-low-cycle loading by internal pressure and bending moment. One of the main problems, which were to be solved using the developed numerical approach, is determination of the influence of these interrelated phenomena on the load-carrying capacity of a specific welded structure. Considered for this purpose, was a characteristic example of PE of $D \times t$ = 315×10 mm size from stainless steel 316L (E = 193 GPa, $\nu = 0.3$, σ_T = 170 MPa) with local erosion loss of metal of a semi-elliptical shape on the pipe inner surface ($2s \times 2u \times \delta$ = 40×20×5 mm). Examples of stress distribution over the pipe cross-section after welding and under the working conditions are given in Figure 2.

Figure 3, *a* shows the dependencies of local stresses $\sigma_{\beta\beta}$ on strain $\varepsilon_{\beta\beta}$ near the internal defect of erosion thinning, taking and not taking into account plastic damage of the material caused by internal pressure P = 10 MPa and bending moment M from –85 to 85 kN (that corresponds to the range of maximum axial stress range from –120 to 120 MPa). As one can see, accumulation of ductile fracture porosity at plastic deformation of the steel pipe leads to displacement of stress hysteresis loops to higher strains through softening of porous materials and reduction of the load-carrying structure cross-section.

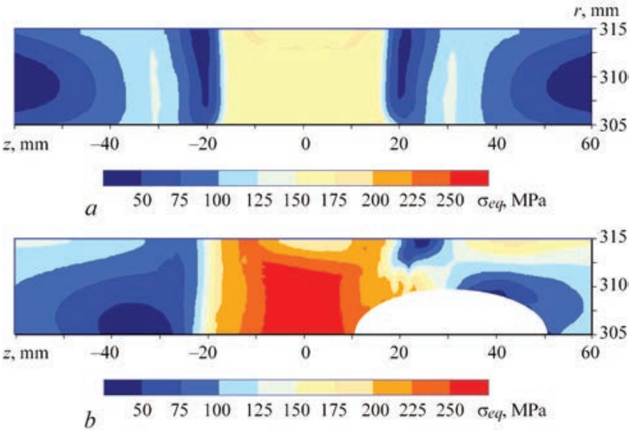

Figure 2. Calculated distributions of intensity of stresses σ_i in the pipeline ($D \times t$ = 315×10 mm, 316L stainless steel): *a* — residual state in the area of a circumferential site weld; *b* — with internal erosion defect ($2s \times 2u \times \delta$ = 40×20×5 mm) at working pressure P = = 8.0 MPa

The intensity of plastic damage accumulation at ultra-low-cycle loading (i.e the rate of increase of porosity volume concentration *f* per cycle number *N*) has three main stages: plastic strain prior to plastic damage initiation; porosity initiation and redistribution of strain and stress fields; stable increase of plastic strains and concentration of porosity volume up to the limiting state. The first two stages correspond to static loading and proceed in the first cycles, while the third stage is related to fatigue fracture of plastically deformed material. Figure 3, *b* shows the results of numerical evaluation of plastic damage accumulation for the considered case of eroded PE at the stable growth stage. As one can see, porosity concentration *f* rises quasilinearly, starting from the second loading cycle by the bending moment at the same internal pressure *P*. It means that increase rate *f* depends mainly on the

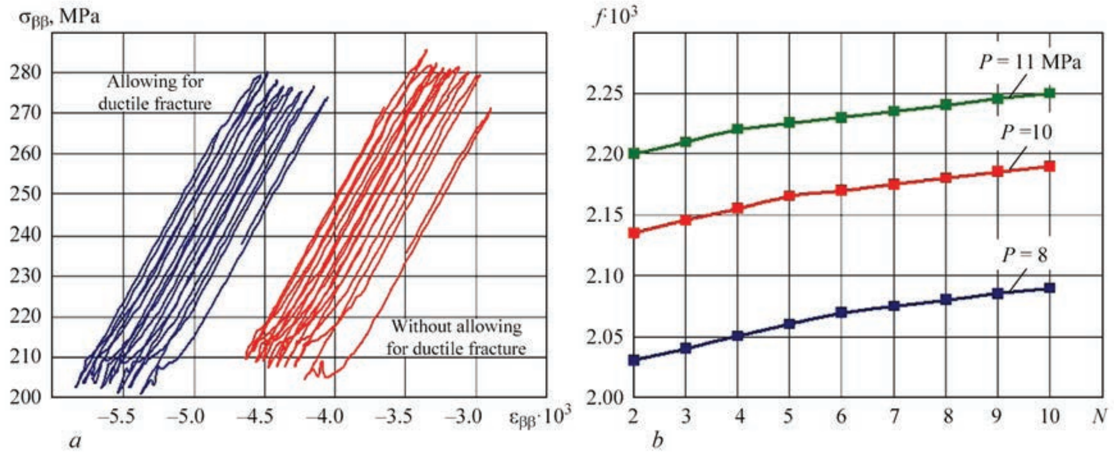

Figure 3. Dependencies of stresses $\sigma_{\beta\beta}$ on stains $\varepsilon_{\beta\beta}$ near an internal defect of erosion wall thinning ($2s \times 2u \times \delta$ = 40×20×5 mm) of pipeline element ($D \times t$ = 315×10 mm, 316L stainless steel), taking and not taking into account the material damage by the ductile mechanism (internal pressure P = 10 MPa and bending moment M = –85–85 kN·m) (*a*) and of maximum volume concentration of pores *f* on cycle number *N* (*b*)

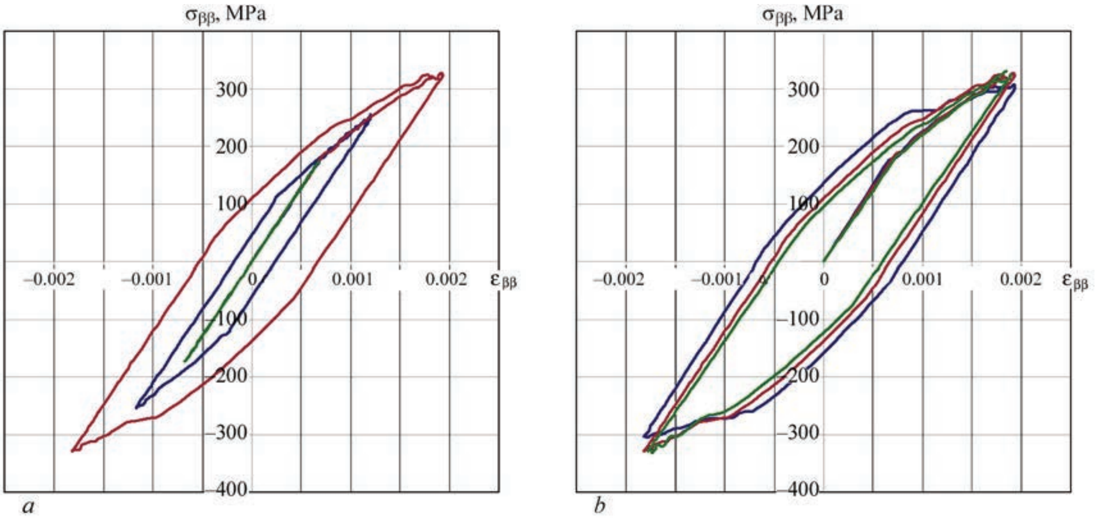

Figure 4. Impact of alternating internal pressure on the kinetics of stress-strain state of defective welded PE ($D \times t$ = 315×10 mm, 316L stainless steel): (*a*) — $2s \times 2u \times \delta$ = 40×20×5 mm, P = –20÷20 MPa, M = 0 kN·m (●), P = –30–30 MPa, M = 0 kN·m (▲), P = = –40–40 MPa, M = 0 kN·m (■); (*b*) — P = –40–40 MPa, M = 0 kN·m, $2s \times 2u \times \delta$ = 40×20×4 mm (●), $2s \times 2u \times \delta$ = 40×20×5 mm (■), $2s \times 2u \times \delta$ = 40×20×6 mm (▲)

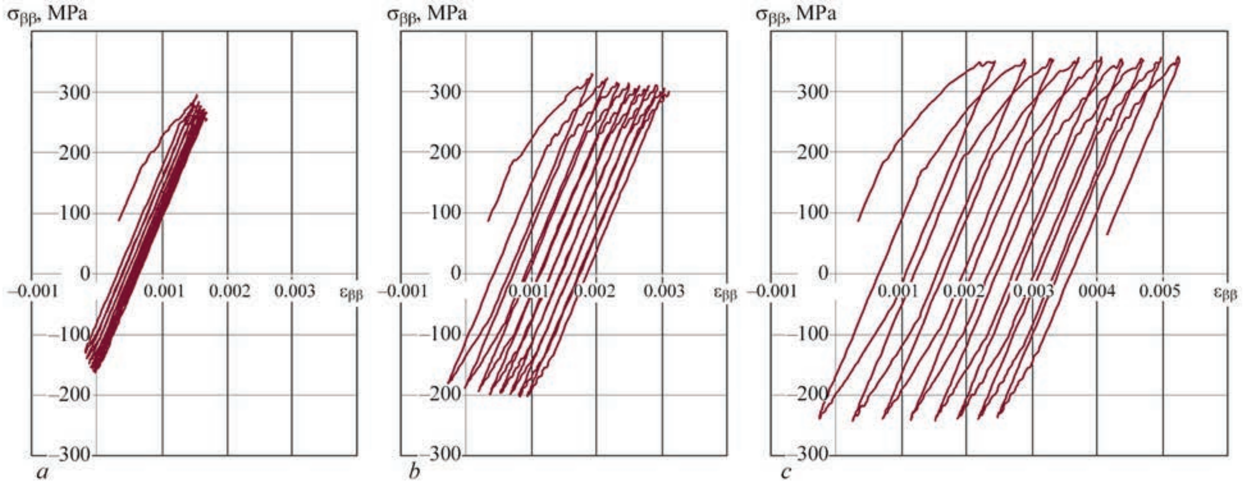

Figure 5. Features of the impact of asymmetry of the cycle of PE (($D \times t$ = 315×10 mm, 316L stainless steel) loading by internal pressure on the kinetics of plastic strain accumulation: *a* — P = –15–35 MPa, M = 0 kN·m; *b* — P = –20–40 MPa, M = 0 kN·m; *c* — P = = –25–45 MPa, M = 0 kN·m

applied range of bending loading, and not on the path of plastic (or general) deformation.

It should be noted that in the case of impact of solely pressure varying by a symmetrical cycle (for instance, in the case of underwater pipelines or complex pressure vessels – carrier rocket tanks, exposed to both internal and external pressure), the dependence of current stresses on strains in the characteristic area of stress raiser of PE with wall thinning defect, has the classical form of a closed hysteresis loop (Figure 4). The size and shape of the loop in such a case depend on the range of pressure values, as well as on the defect size. It means that performance limitation in such a case is due solely to accumulation of subcritical damage by the ductile mechanism, which causes gradual destruction of the material and it reaching the limiting state. At loading cycle asymmetry, the intensities of the positive and negative plastic strains are not balanced that causes gradual displacement of the hysteresis loop along the strain axis (Figure 5). For the mentioned case it is attributable for greater influence of strain hardening, compared to Bauschinger effect.

For practically important cases, such an asymmetry of the cycle is characteristic of pipelines under pressure, which are additionally cyclically loaded by an alternating bending moment. Here, a constant component, which is proportional to internal pressure, is added to bending longitudinal stresses and strains proper, which typically change by a symmetrical cycle, in keeping with the solution of Lame problem. Therefore, it is to be expected that at unchanged cycle of loading by bending moment, increase of internal pressure will have a significant negative impact on the load-carrying capacity of a defective pipeline for the reason of a considerable displacement of the hysteresis loop of the stress-strain state. This is confirmed by calculation results given in Figure 6.

A characteristic feature of the field of bulk concentration of subcritical damage f in the cross-section of a defective pipeline, that is under the impact of both

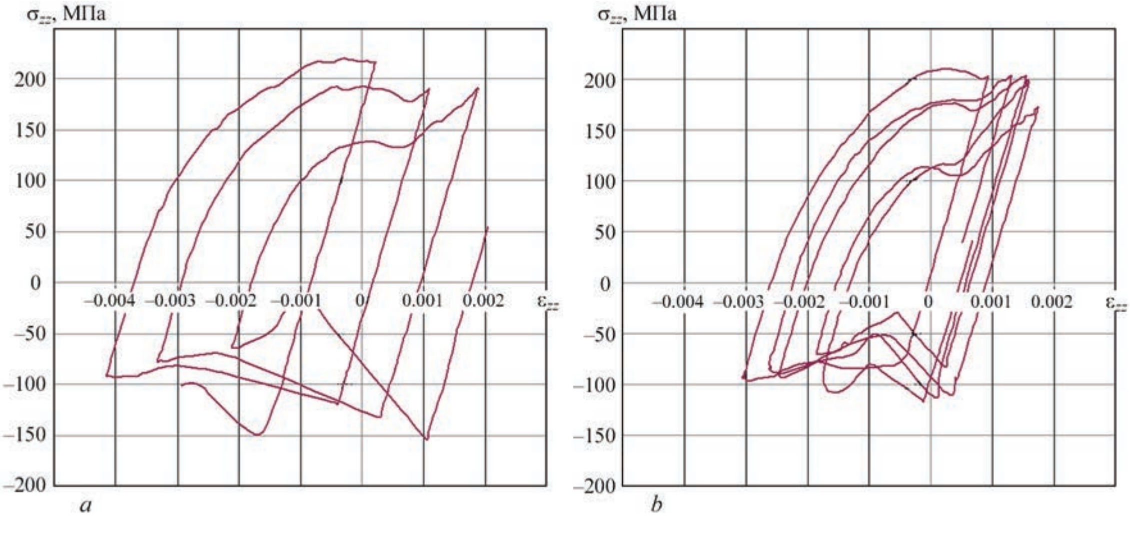

Figure 6. Kinetics of stress-strain state of defective welded PE (($D \times t$ = 315×10 mm, 316L stainless steel) under the impact of cyclic loading by bending moment: *a* — P = 10 MPa, M = –70–70 kN·m; *b* — P = 8 MPa, M = –70–70 kN·m

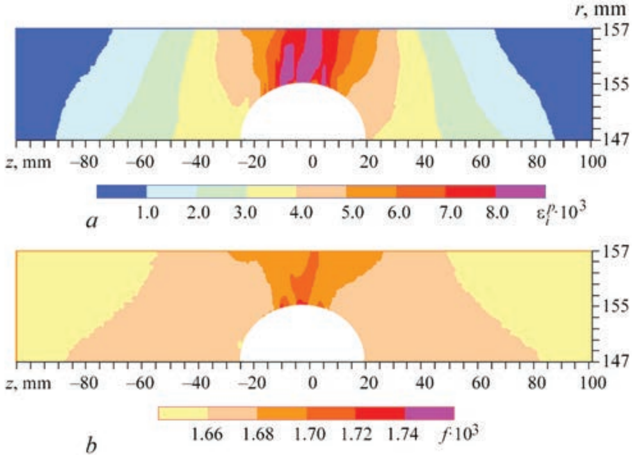

Figure 7. Distribution of plastic strain intensity (*a*) and concentration of ductile fracture pores (*b*) in the cross-section of pipeline element ($D \times t$ = 315×10 mm, 316L stainless steel) with internal wall thinning ($2s \times 2u \times \delta$ = 40×20×5 mm) in the limiting state at internal pressure P = 8 MPa and cyclic bending moment M = = –85–85 kN·m)

internal pressure and alternating bending moment, is a sufficiently narrow area of maximum pore concentration in the current and limiting state of the structure (Figure 7). This is attributable to the fact that depending on deformation direction under cyclic loading conditions, the maximum and minimum stresses form alternatively on different surfaces of the pipe in the geometrical stress raiser area.

Conclusions

1. Mathematical models of the stress-strain and damage state of pipeline elements with detected defects of local wall thinning at ultra-low-cycle loading were constructed. In order to adequately take into account the nonlinearity of material properties at cyclic plastic deformation (Bauschinger effect) and ductile fracture accumulation, an appropriate description of the surface of plastic flow of the material within the conceptual model of elasto-plastic continuum was proposed.

2. A characteristic example of a welded pipeline element ($D \times t$=315×10 mm, 316L stainless steel) with detected internal defect of erosion thinning of the wall was used to show the features of stress-strain kinetics under the conditions of loading by cyclic internal pressure and bending moment. An essential impact of loading cycle asymmetry on plastic damage accumulation is shown: violation of the balance between strain hardening and softening by Bauschinger effect causes a gradual displacement of the stress-strain state loop.

3. It is shown that accumulation of plastic strains during alternating cyclic loading causes initiation and growth of ductile fracture pores in the area of a defect of local wall thinning with formation of a rather narrow area of maximum pore concentration. This is caused by the fact that under the conditions of cyclic loading the maximum and minimum stresses form at different surfaces of the pipe in the area of the geometrical stress raiser (depending on the cycle).

1. (2004) *Recommended practice*, DNV-RP-F101. Corroded Pipelines. Ed. by O. Bjornoy. Hovik, Det Norske Veritas..
2. Hertelé, S., Cosham, A., Roovers, P. (2016) Structural integrity of corroded girth welds in vintage steel pipelines. *Engineering Structures*, **124**, 429–441. DOI: https://doi.org/10.1016/j.engstruct.2016.06.045
3. Milenin, A., Velikoivanenko, E., Rozynka, G., Pivtorak, N. (2019) Probabilistic procedure for numerical assessment of corroded pipeline strength and operability. *Int. J. of Pressure Vessels and Piping*, **171**, 60–68. DOI: https://doi.org/10.1016/j.ijpvp.2019.02.003
4. Morin, L., Michel, J.-C., Leblond, J.-B. (2017) A Gurson-type layer model for ductile porous solids with isotropic and kinematic hardening. *Int. J. of Solids and Structures*, **118–119**, July, 167–178. https://doi.org/10.1016/j.ijsolstr.2017.03.028
5. Chun, B.K., Jinn, J.T., Lee, J.K. (2002) Modeling the Bauschinger effect for sheet metals, Pt I: Theory. *Int. J. of Plasticity*, **18**, 571–595. DOI: https://doi.org/10.1016/S0749-6419(01)00046-8
6. Xue, L. (2008) Constitutive modeling of void shearing effect in ductile fracture of porous materials. *Engineering Fracture Mechanics*, **75**, 3343–3366. DOI: https://doi.org/10.1016/j.engfracmech.2007.07.022
7. Chen, Z., Butcher, C. (2013) *Micromechanics Modelling of Ductile Fracture*. Dordrecht, Springer Netherlands. https://doi.org/10.1007/978-94-007-6098-1
8. Makhnenko, V. (2013) Problems of examination of modern critical welded structures. *The Paton Welding J.*, **5**, 21–28.
9. Zhang, Z.L. (2001) *A complete Gurson model.* Nonlinear fracture and damage mechanics. Ed. by M.H. Alibadi. UK, WIT Press Southampton, 223–248.
10. Velikoivanenko, E., Milenin, A., Popov, A. et al. (2019) Methods of numerical forecasting of the working performance of welded structures on computers of hybrid architecture. *Cybernetics and Systems Analysis*, 55(**1**), 117–127. DOI:https://doi.org/10.1007/s10559-019-00117-8
11. Cowper, G.R., Symonds, P.S. (1958) *Strain hardening and strain rate effects in the impact loading of cantilever beams*. Brown Univ., Applied Mathematics Report.
12. Lemaitre, J., Chaboche, J.-L. (1990) *Mechanics of solid materials.* Cambridge, Cambridge University Press. https://doi.org/10.1017/CBO9781139167970
13. Makhnenko, V.I. (2006) *Safe service life of welded joints and assemblies of modern structures.* Kiev, Naukova Dumka [in Russian].
14. Milenin, O. (2017) Numerical prediction of the current and limiting states of pipelines with detected flaws of corrosion wall thinning. *J. of Hydrocarbon Power Engineering*, 4(**1**), 26–37.

Received 30.11.2021

https://doi.org/10.37434/tpwj2021.01.07

STUDY OF CHANGE IN SPECIFIC ELECTRICAL CONDUCTIVITY OF BIOLOGICAL TISSUES AS A RESULT OF LOCAL COMPRESSION BY ELECTRODES IN BIPOLAR WELDING

Yu.M. Lankin, V.G. Solovyov and **I.Yu. Romanova**
E.O. Paton Electric Welding Institute of the NAS of Ukraine
11 Kazymyr Malevych Str., 03150, Kyiv, Ukraine. E-mail: office@paton.kiev.ua

The paper presents the results of mathematical modeling of anisotropy of specific electrical conductivity (ASEC) of a soft biological tissue and investigates the difference between the results of the process of welding biological tissues produced without and taking into account anisotropy of the specific electroconductivity of a biological tissue. The results of calculations of the tissue resistance, current density and impedance dispersion are compared. 14 Ref., 1 Table, 10 Figures.

Keywords: welding of biological tissues, specific electrical conductivity, mathematical modeling, anisotropy of biological tissues

Soft biological tissues (SBTs) consist of cells, conjunctive tissue and tissue fluid. The basic structural unit of all living things is cells. They consist of a membrane inside which a jelly-like cytoplasm with a large number of organelles is located. The basis of conjunctive tissue consists of collagen and elastin fibres. These fibres together with membranes form a spongy structure of the conjunctive tissue, in the cells of which tissue fluid is located. Due to such a structure, SBTs are much more elastic than any metal and even rubber. During compressing by an electrical welding tool, they are significantly deformed, which leads to significant changes in their electrical and thermophysical properties. Electric welding of SBTs differs from electrocoagulation by an obligatory application of a considerable force of electrodes compression [1, 2]. The electrodes pressure leads to destruction of cell membranes (possibly), transfer of an electroconductive tissue water from the centre of the electrodes to the periphery in the direction of decreasing pressure, increasing vaporization temperature and the maximum temperature of the tissue.

Currently, researchers are paying a considerable attention to improving the quality and reliability of welded joints of SBTs, expanding the range of types and thickness of welded tissues by studying the process of resistance electric welding of SBTs as an object of automatic control. They provide analytical calculations, computer modeling of welding process, experimental studies in laboratory installations, processing and analysis of the obtained results [3–10].

The publications on mathematical modeling of thermal processes in SBTs are known (for example, [11]). But all of them are devoted either to surface heating applying a focused power source such as a laser beam, or with the help of single-electrode electrosurgical instruments. In addition, SBTs are considered in them as solids with constant thermophysical and electrical characteristics. These assumptions can only be used as a first approximation for modeling electrocoagulation, but are not suitable for modeling electric welding.

Biological tissues are electroconductive due to the presence of an intracellular and tissue fluid with the salts dissolved in it. Ions are the main current carriers in them. The proteins, of which cell membranes, organelles, and structural tissues are built, are not electroconductive. Electroconductive of the tissue depends on its internal structure and it changes significantly in the welding process due to a local compression by the electrodes, phase transformations of water in the tissue, coagulation of proteins, thermal effects, etc. Consequently, the specific electroconductivity in each elementary volume of the tissue has a significant anisotropy. Joule heat, which is released in each elementary volume of the tissue during the flow of current, is proportional to the square of current and inversely proportional to its electroconductivity. In this case, in the literature sources the thermal processes are mainly described, the results of which were obtained using the values of the specific conductivity of an uncompressed tissue [12, 13].

Yu.M. Lankin — https://orcid.org/0000-0001-6306-8086, V.G. Solovyov — https://orcid.org/0000-0002-1454-7520,
I.Yu. Romanova — https://orcid.org/0000-0001-7154-1830

Figure 1. Laboratory welding unit: *1* — laser sensor of electrode movement; *2* — electrodes; *3* — weights; *4* — lever axis

Between the electrode clamps, where the tissue is compressed the most and has the greatest deformation, the main processes, characterizing bipolar welding of SBTs, take place. In this regard, the study of the anisotropy of the specific conductivity of a compressed SBT is relevant.

The aim of the work is to show the difference between the values of the parameters of processes of welding SBTs, obtained without taking and taking into account ASEC of biological tissues.

Experimental studies. The study of SBTs compression was performed in a laboratory welding unit (Figure 1). On it, laser sensor is mounted to move the upper electrode relative to the lower one. The movement of the laser point, which glows on the remote screen, corresponds to the movement of the upper electrode with a gain factor of several tens of times. Expansion of the upper electrode displacement measurement system is ±15 μm. At such sensitivity, the accuracy of measuring the thickness of a compressed tissue is already beginning to be affected by the deformation of the entire structure, which leads to some movement of the lower electrode with an increase in the load in the form of a weight. To minimize these errors, the dependence of the movement of the upper electrode on the value of the applied force without the tissue between the electrodes was previously determined. This dependence was used to correct the sensor values while measuring changes in the thickness of the tissue depending on the compression force.

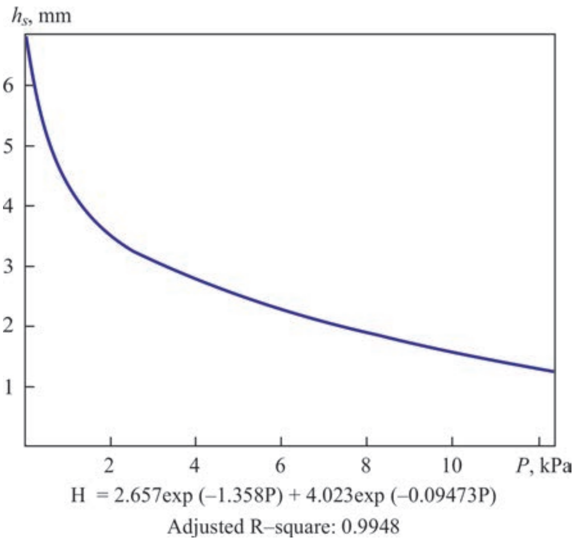

Figure 2. Dependence of thickness of heart muscle between the electrodes of electric welding unit h_s on electrodes pressure P

The range of the set pressure of electrodes P amounts to 15–1100 kPa. Since the actual pressure on the surface of the electrodes is nonuniformly distributed, in our case the average value of the pressure $P = F/S_e$ is meant, where F is the force applied to the electrodes; S_e is the contact surface area of the electrodes.

The cross-section of the electrodes is 3×10 mm, i.e. $S_e = 30$ mm^2. The long sides of the electrodes, rectangular in the cross-section, are perpendicular to the longitudinal axis of the lever. This guarantees a uniform pressure distribution along the larger side of the electrode and a small nonuniformity along the smaller one. In the experiment the heart muscle of a pig was used, taken no later than three hours after slaughter. Before the study, the heart was stored at a temperature of +5 °C.

Figure 2 shows the dependence of the heart muscle thickness h_s between the electrodes of the electric welding unit on P. The sizes of the heart muscle fragment are the following: thickness $m_s = 6.9$ mm, width $l_h = 35$ mm and depth $d_h = 25$ mm. The area of the heart muscle fragment is $S_f = 875$ mm^2.

Simultaneously with the measurement of $h_s = (P)$, the electrical resistance of the heart muscle fragment $R_f(P)$ was measured at a constant voltage $U_s = 6.9$ V through the resistance $R = 1$ kOhm. The voltage at the electrodes U_{ind} was measured. There are many schemes for measuring the resistance of SBT and a common problem for them is the inaccuracy of maintaining the sizes of the specimens. However, in our case the measurement of the same specimen is carried out, but at a different local compression of the tissue. Therefore, under the condition $S_f >> S_e$, the set initial inaccuracy of the sizes of the heart muscle fragment is neglected.

The resistance R_f of the heart muscle fragment is calculated by the formula:

$$R_f = \frac{U_{ind} R}{U_s - U_{ind}}.$$

The results of the experiments are shown in Table, where $h_1 = h_s/m_s$.

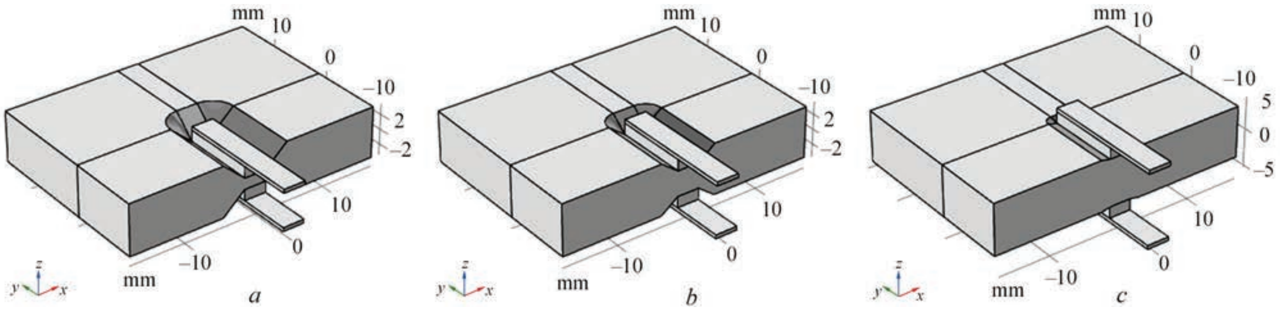

Figure 3. Geometric model of experiment at different values h_s: *a* — $h_s = 1.52$ mm, $h_1 = 0.2203$; *b* — $h_s = 3.43$ mm, $h_1 = 0.4971$; *c* — $h_s = 6,37$ mm, $h_1 = 0.9232$

Mathematical modeling. The mathematical model of the experiment was built using the package COMSOL multiphysics 5.3a. The model includes the modules («Physics») «Electric Currents» and «Heat Transfer in Solids» with the solver «Multiphysics/Electromagnetic Heating», which allows combining these different physics for solving problems of the model. Figure 3 shows a geometric model under different conditions for compression SBT. As materials used in the model, copper and pig's heart muscle are accepted. The main approach to modeling was to provide the best conformity of a geometric part of the model to geometric parameters of the physical experiment. It was necessary to use physical properties of SBT, which correspond to the pig's heart muscle. Based on the theory of similarity [14], such approach will determine the desired values of a specific electrical conductivity of the tissue applying the method of successive approximations, taking into account the data in Table and those calculated on the mathematical model.

In the model for simulating the force of SBT compression, a functional dependence between the compression force and the distance between the compression electrodes $P(h_s)$ is introduced, the inverse dependence of that is obtained experimentally (Figure 2).

The calculated component for «electrical conductivity» $\sigma(x)$ is a graphical interpretation of change in the specific conductivity σ from the coordinate x of the model and the specific intermediate conductivity G_{inter}, where G_{inter} is the value of $\sigma(x)$ at $x = 0$ (Figure 4, *a*). G_{inter} is called intermediate because its value is between the desired minimum value G_{min} and the maximum G_{max} value of the specific electrical conductivity of the tissue. At h_{1min} $G_{inter} = G_{min,}$ at h_{1max} $G_{inter} = G_{max.}$ In Figure 4, *a* the values $G_{max,}$ G_{inter} and G_{min} are taken arbitrarily for clarity of presentation.

Results of experiments

Number	P, kPa	h_s, mm	h_1, rel. un.	R_f(0.3 kHz), Ohm
1	0	6.90	0.9999	778
2	16.4	6.37	0.9232	760
3	146.2	4.20	0.6087	635
4	271.2	3.43	0.4971	586
5	422.1	2.86	0.4145	568
6	557.9	2.53	0.3667	551
7	691.0	2.27	0.3290	551
8	825.0	2.06	0.2986	547
9	960.9	1.65	0.2391	546
10	1091.4	1.52	0.2203	542

Modeling in COMSOL multiphysics applying the method of similarity of geometric parameters of physical and mathematical models allowed determining ASEC in the zone of a local compression of SBT (Figure 4, *b*). As is seen from this diagram, the specific electroconductivity of the pig's heart muscle approximately twice decreases with a decrease in a

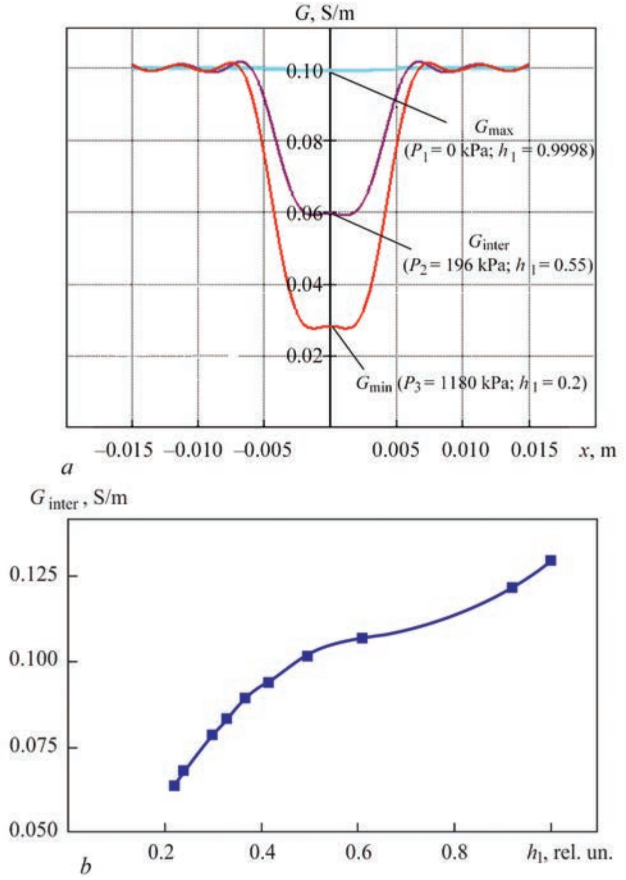

Figure 4. Graphical interpretation of change in specific electrical conductivity $\sigma(x)$ at the maximum value h_{1max}, intermediate value h_{1iner} and the minimum value h_{1min} (*a*) and ASEC at SBT compression (*b*)

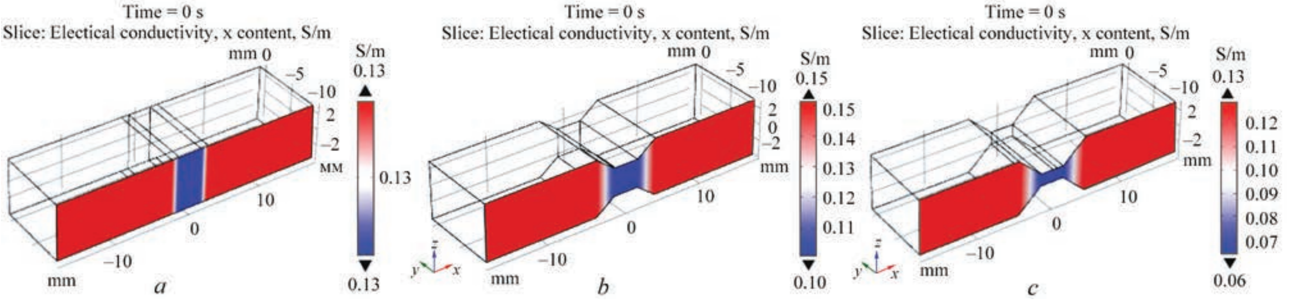

Figure 5. Distribution of specific conductivity in SBT fragment at different values of local compression by electrodes of the pig's heart muscle: *a* — $h_1 = 0.999$; *b* — 0.497; *c* — 0.22

relative compression of SBT. All the published data on specific resistance are obtained for uncompressed biological tissues and are not suitable for using in calculations and mathematical modeling of bipolar welding processes.

Figure 5 shows diagrams of the distribution of specific conductivity in the SBT fragment at different values of local compression. The diagrams show how specific conductivity decreases during compression at the place of local compression of SBT by the electrodes and how it increases at a distance from the place of a local compression of SBT.

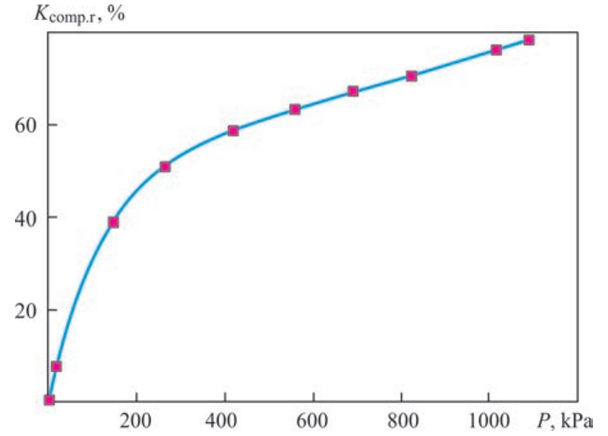

Figure 6. Dependence of compression ratio $K_{\text{comp.r}}$ on the pressure value during compression P

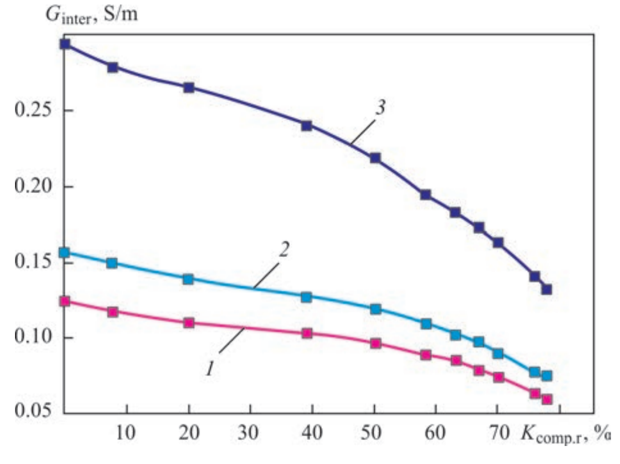

Figure 7. Dependence of specific conductivity of the pig's heart muscle G_{inter} on compression ratio $K_{\text{comp.r}}$ for the frequencies of 0.3 (*1*), 30 (*2*) and 300 (*3*) kHz

As a result of experimental investigations in the laboratory conditions, the dependence of the degree of compression of the biological tissue $K_{\text{comp.r}}$ on the value of the load P during compression was obtained (Figure 6). The compression ratio is calculated by the formula

$$K_{\text{comp.r}} = \left(1 - \frac{h_s}{m_h}\right)\cdot 100\,\%.$$

Figure 7 shows diagrams of dependence of a specific electroconductivity G_{inter} in the zone of a local compression of SBTs on the compression ratio $K_{\text{comp.r}}$ for different frequencies of the applied voltage of 0.3, 30 and 300 kHz. G_{inter} decreases with an increase both in $K_{\text{comp.r}}$ as well as in the frequency of voltage.

Comparison of results. Calculation of complete resistance. Based on the experimentally measured resistances of the SBT fragment of the pig's heart muscle, on the model the resistances with and without taking into account ASEC for different degrees of compression ratio at a frequency of 0.3 kHz were calculated (Figure 8). From this diagram we see that the measurement data, obtained during the experiment coincide with the results of calculations on the model obtained taking into account ASEC. The values of resistances calculated without taking into account ASEC differ from those obtained experimentally in the range of 0–50 %.

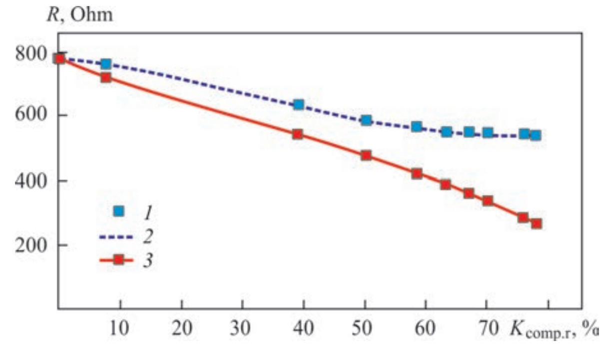

Figure 8. Results of SBT fragment resistance measurements obtained experimentally and calculated on the model taking and without taking into account ASEC: *1* — physical experiment; *2* — model taking into account ASEC; *3* — model without taking into account ASEC

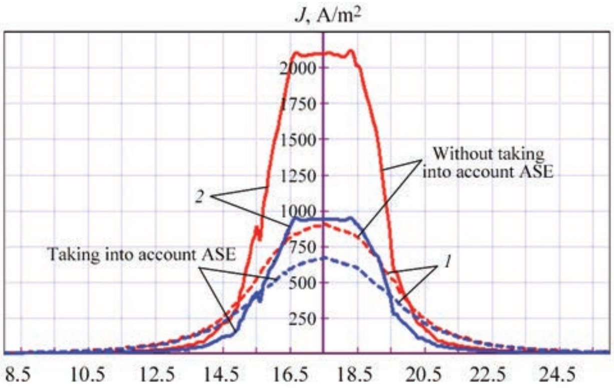

Figure 9. Distribution of current density *J* according to the coordinate x of the model at different $K_{comp.r}$ at a frequency of 0.3 kHz, calculated taking and without taking into account ASEC: *1* — $K_{comp.r}$ = 50.3 %; *2* — 78 %

Calculation of current density. The current density *J* along the coordinate $x = 0$ of the model, which is calculated without taking into account ASEC at $K_{comp.r}$ = 78 %, is twice higher than that calculated taking into account ASEC (Figure 9).

Calculation of impedance dispersion. The resistance of the tissue was determined by the voltmeter-ammeter method during passing a low stable current of different frequency through the tissue. As is seen from Figure 10, the resistance of the tissue to a greater or lesser extent depends on the frequency. For living tissues, this property, called impedance dispersion, is well known. As a result of a physical experiment, the resistance of the simulated fragment of a pig's heart muscle was measured at frequencies of 0.3, 1, 3, 10, 30, 100 and 300 kHz. The calculations of $R(F)$ on the model taking and without taking into account ASEC at the maximum compression of SBTs being 1100 kPa showed that the results obtained taking into account ASEC, coincide with those obtained experimentally. But the results of calculating $R(F)$, obtained without taking into account ASEC, differ from the results obtained experimentally, twice.

Conclusions

1. The adequacy of the results of experimental studies of SBT resistance and the results of calculating SBT resistance obtained on the mathematical model taking into account ASEC is shown.

2. Comparison of the results of calculations without and taking into account ASEC showed, that the relative error of calculations of electrical parameters, such as the total resistance of SBT, current density and impedance dispersion can reach 50–100 %.

1. Shved, O.E. (2008) *Substantiation of new surgical method of hemostasis (experimental-clinical investigation)*: Syn. of Thesis for Cand. of Med. Sci. Degree [in Ukrainian].

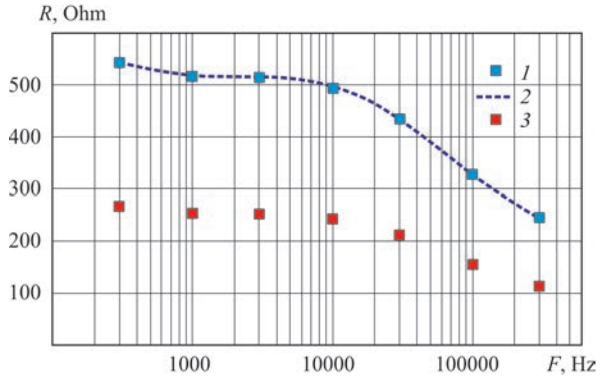

Figure 10. Calculations of resistance of SBT fragment, obtained experimentally on a mathematical model, taking and without taking into account ASEC: *1* — physical experiment; *2* — model taking into account ASEC; *3* — model without taking into account ASEC

2. Chekan, E.G., Davison, M.A., Singleton, D.W. et al. (2015) Consistency and sealing of advanced bipolar tissue sealers. Medical Devices, *Evidence and Research*, **8**, 193–199.
3. Zuev, A.L., Mishlanov, V.Yu., Sudakov, A.I., Shakirov, N.V. (2010) Experimental modeling of rheographic diagnostics of biological fluids. *Rossijskij Zhurnal Biomekhaniki*, 14, **3**(49), 68–78 [in Russian].
4. Khlusov, I.A., Pichugin, V.F., Ryabtseva, M.A. (2007) *Fundamentals of biomechanics of biocompatible materials and biological tissues*: Manual. Tomsk. PU [in Russian].
5. Lamberton, G.R., His, R.S., Jin, D.H. et al. (2008) Prospective comparison of four laparocopic vessel ligation devices. *J. Endourol.*, **22**, 2307–12.
6. *Mara Natascha* Szyrach, Pascal Paschenda, Mamdouh Afify et al. (2012) Evaluation of the novel bipolar vessel sealing and cutting device BiCision® in a porcine model. *Minimaly Invasive Therapy*, 29, 21(**6**), 402–7.
7. Arrese, D., Mazrahi, B., Kalady, M. et al. (2012) Technological advancements in tissue-sealing devices. Special report. *General Surgery News*. Sept.
8. *Gregory W.* Hruby, Franzo C. Marruffo, Evren Durak et al. (2008) Evaluation of surgical energy devices for vessel sealing and peripheral energy spread in a porcine model. *The J. of Urology*, 1, 178(**6**), 2689–93.
9. Eick, S., Loudermilk, B., Walberg, E., et al. (2013) Rationale, bench testing and in vivo evaluation of a novel 5 mm laparoscopic vessel sealing device with homogeneous pressure distribution in long instrument jaws. *Ann. Surg. Innov. Res.*, **7**, 15.
10. Lankin, Yu.N., Sushy, L.F., Bajshtruk, E.N. (2014) System for measurement of temperature of biological tissues in bipolar high-frequency welding. *The Paton Welding J.*, **11**, 32–35.
11. Smolyaninov, V.V. (1980) *Mathematical models of biological tissues*. Moscow, Nauka [in Russian].
12. Lebedev, A.V., Dubko, A.G., Lopatkina, K.G. (2012) Peculiarities of application of theory for resistance welding of metal to welding of live tissues. *Tekhn. Elektrodynamika. Tem. Vypusk*, 187–192 [in Russian].
13. Zuev, A.L., Mishlanov, V.Yu., Sudakov, A.I. et al. (2012) Equivalent electric models of biological objects. *Rossijskij Zhurnal Biomekhaniki*, 16, 55(**1**), 110–120 [in Russian].
14. Gukhman, A.A. (1973) *Introduction to similarity theory*. 2nd Ed. Moscow, Vysshaya Shkola [in Russian].

Received 23.11.2020

https://doi.org/10.37434/tpwj2021.01.08

SIMULATION OF ELECTROMAGNETIC AND THERMAL FIELDS IN THE PROCESS OF INDUCTION HEATING ON SMALL SPECIMENS WITH THE PRESENCE OF WELDED JOINT OF HIGH-STRENGTH RAILWAY RAILS

R.S. Hubatyuk, S.V. Rymar, O.S. Prokofiev, V.A. Kostin, O.V. Didkovskyi and **O.F. Muzhychenko**
E.O. Paton Electric Welding Institute of the NAS of Ukraine
11 Kazymyr Malevych Str., 03150, Kyiv, Ukraine. E-mail: office@paton.kiev.ua

Selection of heating mode, which provides an optimal combination of technological parameters to obtain the necessary structural and phase transformations of welded butt of high-strength railway rails, which is subjected to heat treatment, is a complex process that requires carrying out a large number of experiments with a significant consumption of time, labor, power and financial resources. To solve this type of problem, it is rational to use methods of mathematical and physical modeling, which are based on the use of mathematical models, numerical calculation methods and experimental data of physical modeling in determining key parameters of heat treatment process. For this purpose, based on the theory of similarity, a mathematical model of the process of heat treatment of small specimens was proposed, taking into account the interrelated properties and physical phenomena with the original study. A simplified model of the specimen is considered, on which the optimal heating conditions are tested and the properties of the weld metal subjected to heat treatment are investigated, after which the transition to specifying the conditions of heat treatment of the real welded butt of high-strength railway rails is carried out. This approach makes it possible to significantly reduce the resources in determining the optimal conditions of heating products of high-strength carbon steels, including butt welded joints of railway rails. 13 Ref., 5 Figures.

Keywords: induction heating, heat treatment, weld of railway rails, mathematical modeling, physical modeling, small specimens

When laying a continuous railway track, high-strength rails are used made of new generation steels with an increased carbon content. The base metal and welded rail joints [1, 2] should provide high mechanical characteristics, which are predetermined by an increased axial load and speed of the rolling stock.

To remove residual stresses and normalize the metal of welded joint of rails, heat treatment (HT) is used [3].

One of the most efficient methods of heating during HT process is the method of induction heating using a high frequency (HF) current, which has a number of advantages over other methods. These are contactless heating, high energy density in a specific area of the object subjected to heating, achieving high temperatures, ability to control the temperature field of the object, ability to heat the object in different media, environmental safety of HT process [4]. In connection with the abovementioned, the further investigation and studying the features of phase transformations in welded rail joints after HT process are important [5, 6]. The process of performing induction HT of bodies of a complex shape, which include rails of high-carbon steel, is characterized by a large number of interdependent parameters. Selection of the heating mode, which provides the optimal coincidence of technological parameters to obtain the necessary structural and phase transformations of welded butt of the rail, which is subjected to HT, is a complex process that requires a large number of experiments with significant time, labor, energy and financial resources.

To solve this type of a problem, it is rational to use methods of mathematical and physical modeling, based on the use of mathematical models [6, 7], numerical calculation methods and experimental data of physical modeling in determining key parameters of HT process. For this purpose, based on the theory of similarity, a mathematical model of HT process was proposed, taking into account the interrelated properties and physical phenomena with the original — the real object of investigation. Thus, at first, a small and simplified model of the specimen was considered, on which the optimal heating conditions were tested and the properties of the weld metal were investigated, which was subjected to HT, and then the transition to specifying the conditions of HT of the real welded butt of railway rails are specified.

R.S. Hubatyuk — https://orcid.org/0000-0002-0851-743X, S.V. Rymar — https://orcid.org/0000-0003-0490-4608,
O.S. Prokofiev — https://orcid.org/0000-0003-4643-6611, V.A. Kostin — https://orcid.org/0000-0002-2677-4667,
O.V. Didkovskyi — https://orcid.org/0000-0001-5268-5599, O.F. Muzhychenko — https://orcid.org/0000-0002-4870-3659

In this paper, the principles of mathematical modeling of electromagnetic and thermal fields in the process of induction heating of small specimens in the form of solid round rods at the presence of a transverse weld are considered. Methods of mathematical and subsequent physical modeling should be closely related. The calculated parameters obtained at the stage of mathematical modeling should be the basis for physical modeling, where on small specimens with a weld a real HT process occurs.

After recalculation according to the theory of similarity of the optimal parameters obtained at the stage of physical modeling, a transition to the study of HT of the weld of the real butt and the selection of its heating conditions occurs. In this way the search for optimal conditions of HT of a weld of railway rails is simplified.

To determine the basic parameters of the physical model of the «inductor-product» system, the development of a mathematical model was performed, which reflects the process of HF induction heating of a specimen of high-carbon rail steel with simulation of the welded joint zone. This allows calculating the basic electrical parameters of the system, as well as obtaining the space-time distribution of the temperature field during the process of HT performance. To solve this type of problem, it is possible to use software packages based on the finite element method. The following main elements of the axisymmetric model (Figure 1) were determined:

- a solid rod of a cylindrical shape with a diameter of 8.5 mm and a length of 110.0 mm with the properties and factors inherent in high-carbon steel and with the simulation of the welded joint zone in its center;
- three-turn water cooling inductor with a current of 200 A and a frequency of 130 kHz;
- airspace, bounded by the inner surface of the sphere surrounding the studied system.

The induction heating process is described by a nonlinear interconnected system of Maxwell and Fourier equations, respectively, for the electromagnetic and thermal fields with the corresponding boundary conditions [8].

To obtain the solution of the electromagnetic problem, the system of Maxwell equations is presented in the following differential form:

$$\mathrm{rot}\boldsymbol{H} = \boldsymbol{J} + \frac{\partial \boldsymbol{D}}{\partial t};\ \mathrm{rot}\boldsymbol{E} = \frac{\partial \boldsymbol{B}}{\partial t};$$
$$\mathrm{div}\boldsymbol{D} = p;\ \mathrm{div}\boldsymbol{B} = 0,$$

where $\boldsymbol{H}$, $\boldsymbol{E}$ are the vectors of magnetic and electric field strength; $\boldsymbol{D}$, $\boldsymbol{B}$ are the vectors of electrical and magnetic induction; $\boldsymbol{J}$ is the conduction current density vector; $\boldsymbol{J} = \sigma\boldsymbol{E}$ is the conductivity current density; ρ is the density of a foreign electric charge; σ is the specific conductivity of the substance.

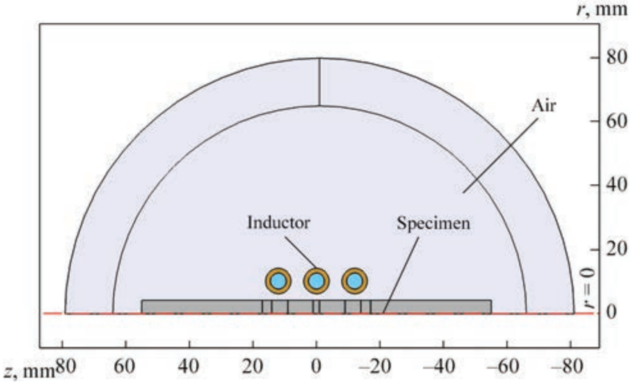

Figure 1. Axisymmetric model of induction system

These equations are supplemented by the equations of the relationship between magnetic field strength and magnetic induction, electric displacement and electric field strength, which characterize the electrical and magnetic properties of the medium:

$$B = \mu_0\mu_r\boldsymbol{H};\ \boldsymbol{D} = \varepsilon_0\varepsilon_r\boldsymbol{E}.$$

where μ_0, μ_r are the absolute and relative magnetic permeability of the medium; ε_0, ε_r are the absolute and relative dielectric permeability of the substance.

With respect to the axisymmetric state, the mathematical model is presented in a two-dimensional cylindrical coordinate system $r0z$.

Since in the axisymmetric model the currents have a direction normal to the plane of the geometric model, than the vector magnetic potential A_φ has one component (0, <φ, 0), in contrast to the fields $\boldsymbol{H}$ and $\boldsymbol{B}$, which have two components (r, z) in this plane.

The mathematical model of the induction system is featured by the presence of the dependence of the electrophysical properties of materials on temperature.

To take into account the dependences of such physical parameters of steel as electrical resistivity $\rho_{st}(T)$, heat capacity $C_{p,st}(T)$ and thermal conductivity $\lambda_{st}(T)$ on the temperature T in the process of heating the specimen, they were set in the form of approximation functions based on data regarding high-carbon steels [9].

The nonlinear dependence of the magnetic permeability of steel on temperature and the loss of magnetic properties in the specimen under study when the temperature of the Curie point is exceeded, which changes the depth of magnetic field permeability into the steel, were also taken into account.

When modeling the induction heating process, as boundary conditions for the electromagnetic part of the model on the symmetry axis $0z$, the absence of the

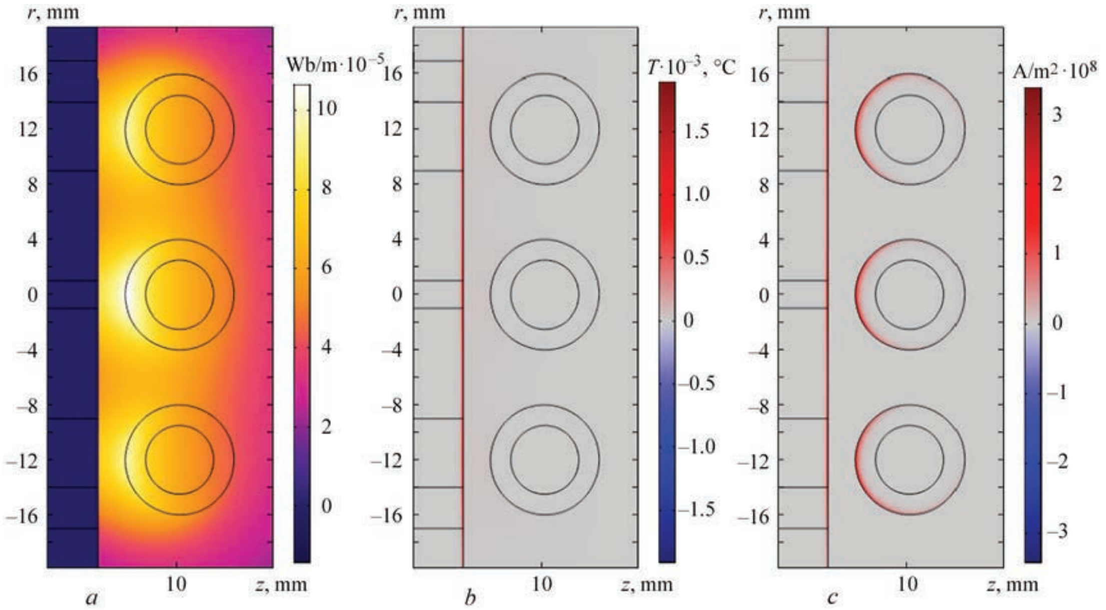

Figure 2. Distribution of magnetic potential A_φ (*a*); magnetic induction *B* (*b*); current density *J* (*c*)

tangential component of the magnetic field intensity and the presence of magnetic insulation at the boundary of the sphere were assumed (see Figure 1).

The mathematical model of the nonstationary thermal problem in the time domain includes the Fourier differential equation, which describes the distribution of the temperature field in the workpiece subjected to heating, in space and time:

$$P_{st}C_{pst}\frac{\partial T}{\partial r}-\nabla\lambda_{st}\nabla T=Q,$$

where Q is the specific power of the heat source.

To take into account heat losses in the mathematical model, the boundary conditions of the third kind in the form of heat exchange with the surrounding medium by convection and radiation from the surface of the specimen, which was subjected to heating, were set.

The condition of a constant temperature of 40 °C in the turns of the inductor in view of its cooling was accepted. On the axis of symmetry 0*z*, the Neumann boundary condition was accepted

$$\frac{\partial T}{\partial r}=0.$$

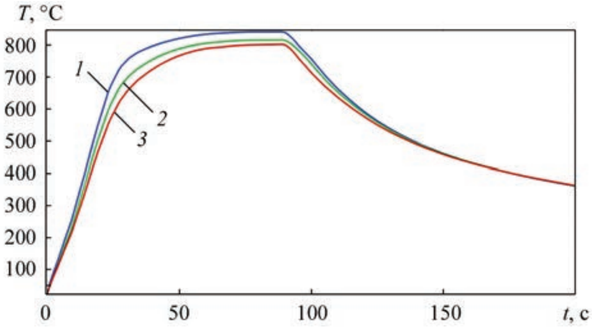

Figure 3. Change in temperature over time on the surface of the specimen along its length during heating: *1* — specimen center; *2* — 6 mm from the center; *3* — 11 mm from the center

As initial data, the amplitude value of current in the inductor and its frequency were taken. The calculation was performed in the following sequence:

electromagnetic — thermal calculation, taking into account the set density of a computational grid, properties of materials and boundary conditions.

During modeling the following physical processes were taken into account:

- current flow in the inductor taking into account the skin effect, ring effect and effect of proximity with the specimen;
- passage of the electromagnetic field and induction of eddy currents in the specimen taking into account the skin effect and effect of proximity to the inductor;
- heating of the specimen metal by eddy currents;
- losses of magnetic properties of the specimen metal after exceeding the temperature of the Curie point;
- thermal conductivity processes in the volume of the specimen metal;
- heat losses due to radiation and convective heat exchange.

In the process of solving the problem, the results concerning distribution of the magnetic potential A_φ (Figure 2, *a*), magnetic induction *B* (Figure 3, *b*) and current density *J* (Figure 3, *c*) were obtained.

According to the results of electromagnetic calculation, the influence of the skin effect, ring and surface effects in the inductor conductors is seen. The current is distributed nonuniformly along the cross-section of the conductors and it is concentrated on the surface of the inductor conductors, which are close to the specimen. A similar distribution is observed with the eddy current passing through the outer surface of the specimen under the inductor – along the perimeter of the specimen.

The purpose of thermal calculation is to determine the conditions of heating, providing a uniform distribution of thermal field on the surface of the specimen over time in the area, simulating the weld, to produce a homogeneous metal structure in the heating spot. In this case, the temperature should be higher than the phase transformation point A_{c3} and be in the range of 750–950 °C. A sufficiently uniform temperature distribution along the length of the specimen under the inductor (at a distance of up to 8 mm from the heating center) in the control points on the surface of the specimen was obtained (Figure 3).

Within 30 s from the start of heating an intensive growth in the temperature of the specimen occurs. During this period of time, the specimen has ferromagnetic properties, the depth of the skin layer is small and the density of the induced current in it is large, which provides a high level of heating power, which is generated in the specimen. After 30 s at the same values of current, the heating rate decreases due to a gradual loss of magnetic properties by the specimen metal and a decrease in the density of the induced current and, respectively, a reduction in thermal power, released in the specimen metal. As a result, the heating intensity decreases. After 50 and up to 90 s of the heating process, a forced temperature holding is carried out to normalize the metal of the weld and the near-weld zone (8–10 mm from the weld center) by regulating current in the inductor and specific power embedded in the specimen metal. After 90 s, the heating is stopped and the specimen is cooled naturally. Mathematical modeling of the induction heating process allows calculating and determining the required conditions of heating depending on configuration and geometric dimensions of the specimen and inductor at set thermophysical parameters of the specimen metal and energy parameter set to determine distribution of electromagnetic and thermal fields in the «inductor-product» system. After numerical calculation of heating conditions, the physical modeling of the process of heat treatment of welded joint of a small specimen is carried out in compliance with the conditions obtained by calculations and with their subsequent specification. Next, the hardness of the metal is investigated and the structural transformations formed in the metal are analyzed. If characteristics of the metal of the specimen, subjected to heat treatment, meet the necessary requirements, than having performed recalculation of the parameters of the heat treatment process according to the theory of similarity, it is necessary to proceed to studying the process of induction heating during heat treatment of the metal of the weld and near-weld zone of railway rails, at the same time maintaining the heating conditions obtained by the method of calculations and specifying them, and also correcting the inductor configuration [10–13].

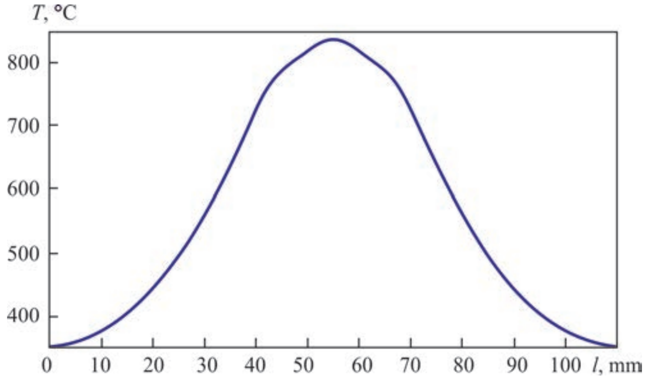

Figure 4. Temperature distribution on the surface of the specimen along its length at the end of heating process

Figure 4 shows the temperature distribution on the surface of the specimen along its length at the end of the heating process (90th second), and Figure 5 shows the temperature field distribution in the specimen (70th second) of the heating process.

Therefore, small specimens allow determining the optimal conditions of induction heating, which are initial when studying and selecting optimal conditions

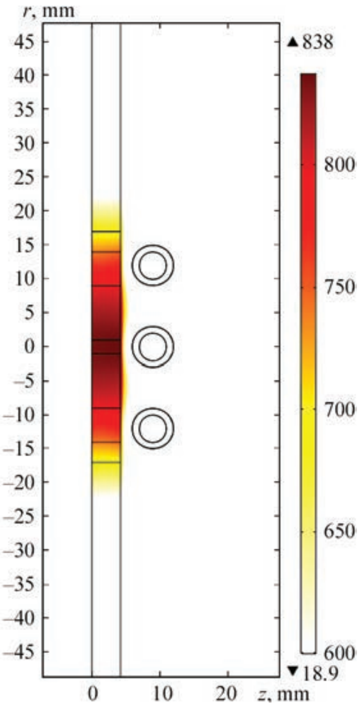

Figure 5. Temperature field distribution in the specimen

of induction heating to perform HT of welded butts of railway rails of high-strength steels.

Such an approach can significantly reduce the time, labor, energy and financial resources in determining the optimal conditions of heating high-strength carbon steel products, such as butt welds of railway rails.

Before performing physical heating of the weld of railway rails according to determined parameters of the heat treatment process, it is also rational to perform mathematical modeling of the process of heating the weld by the inductor that covers the weld and has a complex shape close to a complex cross-section of the railway rail itself. Performing mathematical modeling of the «inductor–measurement» system is possible in a three-dimensional 3D model using a computer of the required power, which is necessary to calculate the energy parameters of the inductor and its geometric dimensions. Performing mathematical modeling of the «inductor–measurement» system to calculate the energy parameters of the inductor and its geometric dimensions is the last and important stage of modeling, which is based on a large array of data and requires additional investigation.

Conclusions

1. The selection of heating conditions, which provides an optimal combination of technological parameters of the heat treatment process to obtain the necessary structural and phase transformations in the butt weld of high-strength railway rails is a complex process, that requires carrying out a large number of experiments, significant time, power, labor and financial costs. To solve this type of problem, it is more rational to use methods of mathematical and physical modeling, based on the use of mathematical models, numerical calculation methods and obtained experimental data of physical modeling in determining key parameters of the heat treatment process on small specimens with the subsequent transition according to the theory of similarity to determination of conditions of heat treatment of real welded butts of railway rails.

2. The use of small specimens allows selecting and determining optimal conditions of induction heating, which are the basis during further investigations and selection of optimal conditions of induction heating when performing heat treatment of real welded butts of railway rails of high-strength steels. Also, the use of mathematical models, numerical calculation methods and the obtained experimental data of physical modeling in determining key parameters of heat treatment process on small specimens allow determining energy parameters of the inductor and its geometric dimensions, as well as capacity of the power source and other induction equipment with a subsequent transition according to the theory of similarity.

1. Kuchuk-Yatsenko, S.I., Krivenko, V.G., Didkovsky, A.V. et al. (2012) Technology and new generation of equipment for flash-butt welding of advanced high-strength rails for construction and reconstruction of high-speed railway lines. *The Paton Welding J.*, **6**, 22–26.
2. Kuchuk-Yatsenko, S.I., Didkovsky, A.V., Shvets, V.I. et al. (2016) Flash-butt welding of high-strength rails of nowadays production. *Ibid.*, **5–6**, 4–12. DOI: https://doi.org/10.15407/tpwj2016.06.01
3. Gubatyuk, R.S. (2019) Heat treatment of welded joints of high-strength railway rails (Review). *Ibid.*, **2**, 41–48. DOI:https://doi.org/10.15407/tpwj2019.02.07
4. Rudnev, V., Loveless, D., Cook, R., Black, M. (2003) *Handbook of induction heating*. Marcel Dekker Inc., New York, USA.
5. Panteleymonov, E.A. (2018) On the problem of heat treatment of welded joints of railway rails. *The Paton Welding J.*, **3**, 36–39. DOI: https://doi.org/10.15407/tpwj2018.03.08
6. Pleshivtseva, Yu.E., Popov, A.V., Popova, M.A., Derevyanov, M.Yu. (2019) Optimal design of inductor for surface hardening of cylindrical billets on the base of numerical 2D model. *Vestnik Astrakh. GTU. Seriya: Upravlenie*, *Vychislitelnaya Tekhnika i Informatika*, **1**, 40–50 [in Russian].
7. Kucheryavaya, I.N. (2015) Application of multiphysical modeling in solution of problems of electrical engineering. *Pratsi IED NANU*, 42, 112–122 [in Russian].
8. Landau, L.D., Lifshits, E.M. (2006) *Field theory. Theoretical physics.* Vol. 2. Moscow, Fizmatlit [in Russian].
9. Chirkin, V.S. (1959) *Thermophysical properties of materials.* Moscow, Fizmatlit [in Russian].
10. Prokofiev, O.S., Gubatyuk, R.S., Pismennyi, O.S. et al. (2020) Development of inductors for bulk and surface heat treatment of welded butt joints of railway rails. *The Paton Welding J.*, **5**, 41–48. DOI: https://doi.org/10.37434/tpwj2020.05.07
11. Prokof'iev, O., Gubatyuk, R., Rymar, S. et al. (2020) Inductor for uniform bulk heat treatment of welded butt joints of railway rails. *Solid State Phenomena*, **313**, 72–81.
12. Pysmennyi, O.S., Panteleimonov, E.O., Rymar, S.V., Gubatiuk, R.S. (2016) *Induction device for heat treatment of welded joints of railway rails.* Pat. Ukraine on utility model UA 116086 U, Int. Cl. (2006.01) C21D 1/10. Fill. 03.11.2016; Publ. 10.05.2017 [in Ukrainian].
13. Panteleimonov, E.O., Gubatiuk, R.S. (2016) *Induction device for heat treatment of welded joints of railway rails.* Pat. Ukraine on utility model. UA 109123 U, Int. Cl. C21D1/10. Fill. 29.02.2016; Publ. 10.08.2016 [in Ukrainian].

Received 14.12.2020

https://doi.org/10.37434/tpwj2021.01.09

MATHEMATICAL MODELS OF THE DEPENDENCE OF MECHANICAL PROPERTIES ON CHEMICAL COMPOSITION OF STEELS FOR ESW

S.V. Egorova, O.V. Makhnenko, G.Yu. Saprykina and **D.P. Syneok**
E.O. Paton Electric Welding Institute of the NAS of Ukraine
11 Kazymyr Malevych Str., 03150, Kyiv, Ukraine. E-mail: office@paton.kiev.ua

The paper deals with the possibility of constructing mathematical models of the dependence of mechanical properties of silicon-manganese steels designed for ESW, which have high brittle fracture resistance in the HAZ, as well as of the overheated zone, on chemical composition. Data on mechanical properties of these steels were obtained as a result of studying the influence of additional alloying (microalloying) of silicon-manganese steel by manganese, chromium, vanadium, boron, cerium and zirconium, on overheating resistance at electroslag welding. The method of multiple linear regression was used for construction of mathematical models. Mathematical models were constructed for the following set of base metal mechanical properties: impact toughness for temperatures of (+20, –40, –60, –70 °C), yield limit, ultimate strength, relative elongation and reduction in area. For overheated zone at electroslag welding mathematical models were constructed for impact toughness (*KCU* and *KCV*) for temperatures of +20, –60, –70 °C. Initial validation of the constructed models was performed. 9 Ref., 12 Tables, 2 Figures.

Keywords: silicon-manganese steels, chemical composition, microalloying, mechanical properties, mathematical models, electroslag welding

Investigations conducted at PWI of the influence of chemical composition on the mechanical properties of silicon-manganese steels produced by the method of induction remelting and designed for electroslag welding (ESW), which have a high brittle fracture resistance [1], provided experimental data on the composition and mechanical properties of the base material (Tables 1, 2) and overheated zone (of the HAZ) (Table 3) for 55 experimental melts of low-alloy steels. This information was used to plot the mathematical models for prediction of the mechanical properties of base metal and overheated zone metal at ESW, depending on the chemical composition of steels. Derived models can find effective use at development of new silicon-manganese steels for determination of optimum alloying with the purpose of obtaining the specified mechanical properties and required level of brittle fracture resistance in the HAZ of welded joints produced with ESW application.

General information on construction of regression models. The mathematical models by the available experimental data on mechanical properties and chemical composition of the experimental steels were constructed with application of the method of multiple linear regression, which is designed for modeling the dependence between one dependent variable and several independent variables [2, 3]. Such a relation can be theoretically described by a linear dependence of the following form:

$$Y = b_1 x_1 + b_2 x_2 + \ldots + b_k x_k + u,$$

where Y is the dependent variable — regressand; U is the random component of the model; x_k are the independent variables — regressors.

The coefficients of the model of multiple linear regression are found by the least-squares method.

The least-squares method [4] allows finding such values of the coefficients, for which the sum of squares of deviations will be minimal. The following system of normal equations is solved to determine the coefficients:

$$\begin{cases} nb_0 + b_1\sum x_1 + \ldots b_p \sum x_p = \sum y \\ b_0 \sum x_1 + b_1 \sum x_1^2 + \ldots b_p \sum x_1 x_p = \sum x_1 y \\ \ldots \quad \ldots \quad \ldots \quad \ldots \quad \ldots \quad \ldots \\ b_0 \sum x_p + b_1 \sum x_1 x_p + \ldots b_p \sum x_p x_p = \sum x_p y \end{cases}.$$

Solution of the system can be derived, for instance, by Cramer's method:

$$b_0 = \frac{\Delta b_0}{\Delta}, \quad b_1 = \frac{\Delta b_1}{\Delta}, \ \ldots, \ b_p = \frac{\Delta b_p}{\Delta}.$$

System determinant is written as follows:

O.V. Makhnenko — https://orcid.org/0000-0002-8583-016, G.Yu. Saprykina — https://orcid.org/0000-0003-1534-7253

Table 1. Chemical composition of experimental steels, wt.%

No.	Alloying system	Experimental melt number	C	Mn	Si	S	P	Cr	Ni	V	Al	Ce	B	Zr
1	Mn–Si–Al	20	0.069	1.550	0.530	0.031	0.012	0.150	0.630	–	0.100	0.050	–	–
2	Mn–Si–Ce–Al	25	0.065	1.550	0.770	0.021	0.012	0.200	0.100	–	0.130	0.033	–	–
3	Mn–Si–Al–B	26	0.060	1.350	0.600	0.024	0.012	0.160	0.300	–	0.200	–	0.006	–
4	Mn–Si–Al–B	33	0.091	1.580	0.650	0.021	0.013	0.170	0.140	–	0.330	–	0.005	–
5	Mn–Si–Al	37	0.038	2.350	0.320	0.028	0.040	–	–	–	0.200	–	–	–
6	Mn–Si–Ce–Al	38	0.065	2.300	0.190	0.018	0.012	0.290	0.200	–	0.067	0.075	–	–
7	Mn–Si–Al–Ce–B	82	0.120	2.700	0.500	–	–	–	–	–	0.100	0.065	0.008	–
8	Mn–Si–Ce–Al–Cr–Ni	99	0.080	0.315	–	–	1.000	1.100	–	0.110	0.290	–	–	–
9	Mn–Si–Al–Ce–B	100	0.062	1.860	0.280	0.021	0.012	0.450	0.350	–	0.110	0.029	0.005	–
10	Mn–Si–Al–Ce–Zr–B	133	0.053	2.300	0.520	0.017	0.009	0.080	0.100	–	0.185	0.024	0.004	0.017
11	Mn–Si–Ce–Al–Zr–V–P–Cr	152	0.076	1.260	0.038	0.068	0.009	1.450	0.320	0.035	0.070	0.069	0.003	0.015
12	Mn–Si–Al–Ce–Zr–B–V	153	0.082	1.950	0.580	0.012	0.110	0.320	0.185	0.275	0.160	0.140	0.022	0.200
13	Mn–Si–Al–Ce–Zr–B	156	0.069	2.400	0.550	0.018	0.009	0.060	0.180	–	0.240	0.093	0.003	0.040
14	Mn–Si–Ce–Al–Zr–V–P–Cr	157	0.056	1.600	0.400	0.002	0.009	1.400	0.130	0.032	0.100	0.064	0.004	0.035
15	Mn–Si–Al–Ce–Zr–B–V	163	0.072	1.500	0.500	0.020	0.012	0.080	0.180	0.210	0.140	0.004	0.003	0.075
16	Mn–Si–Al–Ce–Zr	164	0.058	2.400	0.550	0.083	0.015	0.090	0.165	–	0.125	0.100	–	0.086
17	Mn–Si–Al–Ce–B–V	165	0.058	2.500	0.560	0.020	0.013	0.095	0.110	0.200	0.089	0.090	0.005	–
18	Mn–Si–Al–Ce–Zr–B–V	167	0.073	2.350	0.820	0.019	0.018	0.083	0.100	0.130	0.190	0.090	0.004	0.100
19	Mn–Si–Ce–Al–Zr–B–Cr	177	0.068	2.250	0.630	0.014	0.011	2.850	0.100	–	0.220	0.100	0.003	0.045
20	Mn–Si–Ce–Al–Zr–V–P–Cr	203	0.051	1.600	0.050	0.018	0.011	1.500	0.100	0.022	0.110	0.066	0.004	0.020
21	Mn–Si–Ce–Al–Cr	205	0.080	1.280	0.690	0.015	0.010	2.700	0.100	–	0.290	0.072	–	–
22	Mn–Si–Ai–Ce–B	206	0.045	1.280	0.210	0.008	0.013	0.500	–	–	0.038	0.040	0.003	–
23	Mn–Si–Al–Ce–B–V	207	0.052	1.600	0.820	0.016	0.013	0.190	–	0.210	0.075	0.110	0.006	–
24	Mn–Si	410	0.120	1.900	0.380	–	–	–	–	–	–	–	–	–
25	Mn–Si	411	0.130	1.180	0.140	–	–	–	–	–	–	–	–	–
26	Mn–Si	412	0.100	1.400	0.430	–	–	–	–	–	–	–	–	–
27	Mn–Si	413	0.120	2.600	0.570	–	–	–	–	–	–	–	–	–
28	Mn–Si–Al–Ce–V	432	0.080	1.300	0.440	–	–	–	0.100	0.200	0.100	0.160	–	–
29	Mn–Si–Ce–Al–Zr–Cr	433	0.085	1.400	0.800	–	–	2.200	–	–	0.065	0.018	–	0.060
30	Mn–Si–Ce–Al–V–Cr	434	0.085	1.350	0.650	–	–	2.400	0.075	0.051	0.045	0.040	–	–
31	Mn–Si–Ce–Al–Zr–B–Cr	435	0.080	1.420	0.680	–	–	2.350	0.080	–	0.150	0.130	0.004	0.023
32	Mn–Si–Ce–Al–Zr–V–P–Cr	436	0.080	2.100	0.550	–	–	2.600	0.070	0.010	0.185	0.075	0.008	0.020
33	Mn–Si–Ce–Al–Zr–V–B–Cr	437	0.083	2.000	0.490	–	–	2.300	0.070	0.190	0.110	0.085	0.006	–

Table 1 (cont.)

34	Mn–Si–Ce–Al–Zr–V–Cr	438	0.115	2.500	0.670	–	–	2.900	0.100	0.275	0.115	0.080	–	0.040
35	Mn–Si–Al–Ce–V	458	0.080	1.100	0.220	–	–	0.450	0.085	0.010	0.160	0.035	–	–
36	Mn–Si–Al–Ce–Zr–V	459	0.090	2.350	0.760	–	–	0.080	0.140	0.050	0.087	0.150	–	0.017
37	Mn–Si–Ce–Al–Zr–V–Cr	460	0.070	1.700	0.600	–	–	2.600	0.130	0.155	0.095	0.300	–	0.030
38	Mn–Si–Ce–Al–Zr–Cr	505	0.075	1.850	0.770	–	–	1.720	0.170	–	0.130	0.200	–	0.030
39	Mn–Si–Ce–Al–Zr–V–Cr	506	0.080	1.900	0.490	–	–	1.750	–	0.180	0.080	0.110	–	0.010
40	Mn–Si–Ce–Al–Zr–V–B–Cr	507	0.100	1.850	0.680	–	–	1.400	–	0.032	0.070	0.080	0.004	–
41	Mn–Si–Ce–Al–Mo	530	0.050	1.900	0.030	0.030	0.011	0.044	0.070	–	0.068	0.060	–	–
42	Mn–Si–Ce–Al	531	0.065	2.050	0.600	0.014	0.015	0.053	0.110	–	0.063	0.085	–	–
43	Mn–Si	597	0.200	1.100	0.240	–	–	0.140	–	–	–	–	–	–
44	Mn–Si	598	0.190	1.000	0.120	–	–	0.160	–	–	–	–	–	–
45	Mn–Si–Ce–Al–Cr	718	0.090	2.300	0.450	–	–	1.100	–	–	0.040	–	–	–
46	Mn–Si–Ce–Al–Cr	727	0.080	1.200	0.500	–	–	0.650	0.120	–	0.085	–	–	–
47	Mn–Si–Ce–B	728	0.080	2.050	0.600	–	–	0.240	0.090	–	0.042	0.009	0.005	–
48	Mn–Si–Ce–Al–Cr	881	0.063	1.600	0.630	–	–	0.440	0.190	–	0.048	–	–	–
49	Mn–Si–Ce–B	882	0.080	1.750	0.640	–	–	0.160	0.100	–	0.033	0.029	0.006	–
50	Mn–Si–Ce–Al	883	0.065	1.650	0.680	–	–	0.100	0.165	–	0.050	0.085	–	–
51	Mn–Si–Ce–B	894	0.075	1.600	0.650	–	–	0.165	0.145	–	0.032	0.040	0.005	–
52	Mn–Si–Ce–Al	895	0.089	2.250	0.250	–	–	0.080	–	–	0.034	–	–	–
53	Mn–Si–Ce–B	896	0.070	1.230	0.540	–	–	0.040	–	–	0.010	0.046	0.003	–
54	Mn–Si–Ce	127-2	0.120	2.800	0.300	–	–	–	–	–	–	0.060	–	–

Table 2. Mechanical properties of experimental steels (base metal)

No.	Alloying system	Melt number	σ_y, MPa	σ_t, MPa	δ, %	ξ, %	Impact toughness (*KCU*), J/cm^2			
							+20 °C	–40 °C	–60 °C	–70 °C
1	Mn–Si–Al	20	314	444	32.8	65.4	131.5	92.5	89.0	73.5
2	Mn–Si–Ce–Al	25	298	434	34.5	75.0	35.0	343.0	298.0	270.5
3	Mn–Si–Al–B	26	302	447	27.8	75.1	–	44.0	31.0	–
4	Mn–Si–Al–B	33	258	404	36.6	75.0	172.0	130.0	114.5	90.0
5	Mn–Si–Al	37	258	430	39.3	60.9	116.0	37.0	47.5	53.5
6	Mn–Si–Ce–Al	38	270	411	38.5	78.2	236.0	147.0	159.5	140.5
7	Mn–Si–Al–Ce–B	82	441	561	27.3	71.6	–	132.5	125.0	116.0
8	Mn–Si–Ce–Al–Cr–Ni	99	413	523	30.0	71.5	237.0	147.5	121.5	117.0
9	Mn–Si–Al–Ce–B	100	284	410	36.2	79.0	225.5	116.0	156.0	75.0
10	Mn–Si–Al–Ce–Zr–B	133	378	498	31.8	78.2	298.0	184.5	211.5	208.5
11	Mn–Si–Ce–Al–Zr–V–P–Cr	152	488	616	24.2	66.0	220.0	192.0	70.0	11.0
12	Mn–Si–Al–Ce–Zr–B–V	153	760	820	18.6	55.6	–	–	5.5	6.5
13	Mn–Si–Al–Ce–Zr–B	156	417	544	31.3	73.3	150.0	72.0	–	147.0
14	Mn–Si–Ce–Al–Zr–V–P–Cr	157	394	484	28.5	66.9	–	196.0	8.0	7.0
15	Mn–Si–Al–Ce–Zr–B–V	163	378	519	26.9	75.0	202.0	8.0	4.5	4.5
16	Mn–Si–Al–Ce–Zr	164	503	592	18.8	51.0	68.0	9.5	6.0	6.0
17	Mn–Si–Al–Ce–B–V	165	419	535	24.2	66.0	75.0	14.5	–	9.0
18	Mn–Si–Al–Ce–Zr–B–V	167	407	566	–	–	–	16.0	6.0	–
19	Mn–Si–Ce–Al–Zr–B–Cr	177	399	517	18.8	66.0	–	6.0	4.5	–
20	Mn–Si–Ce–Al–Zr–V–P–Cr	203	259	394	–	–	212.0	189.5	167.0	43.0

Table 2 (cont.)

21	Mn–Si–Ce–Al–Cr	205	389	495	27.2	75.0	97.5	29.0	10.5	6.0
22	Mn–Si–Ai–Ce–B	206	268	415	36.5	73.5	246.7	97.0	8.0	5.5
23	Mn–Si–Al–Ce–B–V	207	340	478	32.9	75.0	218.5	112.5	73.5	5.5
24	Mn–Si	410	380	516	32.0	70.8	350.5	196.5	105.0	–
25	Mn–Si	411	303	460	30.8	69.5	197.5	15.0	6.500	–
26	Mn–Si	412	336	432	28.8	70.7	353.0	–	179.5	10.5
27	Mn–Si	413	403	536	28.5	72.1	214.5	–	144.0	162.0
28	Mn–Si–Al–Ce–V	432	293	447	34.2	77.4	325.0	256.0	244.0	252.5
29	Mn–Si–Ce–Al–Zr–Cr	433	376	570	30.0	70.2	–	58.5	7.5	–
30	Mn–Si–Ce–Al–V–Cr	434	424	590	28.5	70.2	121.0	25.0	–	–
31	Mn–Si–Ce–Al–Zr–B–Cr	435	304	425	24.7	44.9	250.0	119.0	2.5	–
32	Mn–Si–Ce–Al–Zr–V–P–Cr	436	633	690	20.0	67.5	63.5	7.0	–	–
33	Mn–Si–Ce–Al–Zr–V–B–Cr	437	507	625	23.8	75.0	5.0	3.5	–	–
34	Mn–Si–Ce–Al–Zr–V–Cr	438	607	714	21.1	66.0	5.5	4.0	–	–
35	Mn–Si–Al–Ce–V	458	602	684	22.8	70.7	3.0	3.0	–	–
36	Mn–Si–Al–Ce–Zr–V	459	455	572	21. 5	62.7	75.0	32.0	–	–
37	Mn–Si–Ce–Al–Zr–V–Cr	460	454	577	27.2	70.5	141.0	15.0	–	–
38	Mn–Si–Ce–Al–Zr–Cr	505	752	669	12.8	37.2	58.5	29.5	–	–
39	Mn–Si–Ce–Al–Zr–V–Cr	506	735	832	18.5	-	34.0	7.0	–	–
40	Mn–Si–Ce–Al–Zr–V–B–Cr	507	401	575	29.5	75.0	75.0	44.5	–	–
41	Mn–Si–Ce–Al–Mo	530	298	443	33.7	77.5	350.0	324.0	–	254.0
42	Mn–Si–Ce–Al	531	323	500	34.9	75.0	295.5	243.0	–	200.0
43	Mn–Si	597	400	487	31.0	68.5	136.0	–	–	–
44	Mn–Si	598	390	492	31.0	38.5	142.5	–	–	–
45	Mn–Si–Ce–Al–Cr	718	386	561	26.2	73.3	–	142.5	126.0	108.5
46	Mn–Si–Ce–Al–Cr	727	245	406	39.2	79.8	–	101.5	–	12.9
47	Mn–Si–Ce–B	728	288	431	36.8	80.5	–	188.2	183.3	33.2
48	Mn–Si–Ce–Al–Cr	881	318	469	–	–	–	274.0	–	224.5
49	Mn–Si–Ce–B	882	385	517	28.7	64.9	–	195.0	–	204.0
50	Mn–Si–Ce–Al	883	–	–	–	–	–	269.5	133.0	98.0
51	Mn–Si–Ce–B	894	318	493	30.7	68.9	–	297.5	–	184.5
52	Mn–Si–Ce–Al	895	319	491	30.3	66.0	–	223.0	–	191.0
53	Mn–Si–Ce–B	896	305	488	26.9	64.9	–	268.0	–	242.5
54	Mn–Si–Ce	127-2	500	637	25.0	69.8	–	131.0	100.0	108.5
53	Mn–Si–Ce–B	896	305	488	26.9	64.9	0.0	268.0	0.0	242.5
54	Mn–Si–Ce	127-2	500	637	25.0	69.8	0.0	131.0	100.0	108.5

Table 3. Mechanical properties of overheated zone

No.	Alloying system	Melt number	Impact toughness (*KCU*), J/cm^2			Impact toughness (*KCV*), J/cm^2		
			+20 °C	–40 °C	–70 °C	+20 °C	–40 °C	–70 °C
1	Mn–Si–Al	20	–	–	142.0	53.5	11.0	–
2	Mn–Si–Ce–Al	25	165.5	–	–	206.0	118.5	41.0
3	Mn–Si–Al–B	26	183.0	–	99.0	–	–	90.5
4	Mn–Si–Al–B	33	191.5	–	–	111.0	73.5	17.5
5	Mn–Si–Al	37	134.5	–	–	81.0	52.5	29.5
6	Mn–Si–Ce–Al	38	187.5	–	–	56.5	66.0	22.5
7	Mn–Si–Al–Ce–B	82	–	121.0	–	108.5	108.5	68.5
8	Mn–Si–Ce–Al–Cr–Ni	99	–	–	–	128.0	116.5	109.5
9	Mn–Si–Al–Ce–B	100	106.5	–	83.5	62.5	66.0	32.5
10	Mn–Si–Al–Ce–Zr–B	133	–	–	–	160.5	148.5	6.5
11	Mn–Si–Ce–Al–Zr–V–P–Cr	152	–	127.5	–	6.0	–	4.0
12	Mn–Si–Al–Ce–Zr–B–V	153	–	8.0	–	405.0	–	4.0
13	Mn–Si–Al–Ce–Zr–B	156	–	167.0	–	5.0	–	5.5
14	Mn–Si–Ce–Al–Zr–V–P–Cr	157	–	19.5	–	5.0	–	4.0
15	Mn–Si–Al–Ce–Zr–B–V	163	–	6.0	–	–	–	4.0
16	Mn–Si–Al–Ce–Zr	164	–	5.0	–	4.5	–	4.0
17	Mn–Si–Al–Ce–B–V	165	–	63.5	–	–	14.5	–

Table 3 (cont.)

18	Mn–Si–Al–Ce–Zr–B–V	167	–	–	–	4.0	–	–
19	Mn–Si–Ce–Al–Zr–B–Cr	177	–	–	–	4.0	–	–
20	Mn–Si–Ce–Al–Zr–V–P–Cr	203	–	49.5	–	17.0	–	6.0
21	Mn–Si–Ce–Al–Cr	205	–	9.5	–	7.0	–	6.0
22	Mn–Si–Ai–Ce–B	206	–	–	–	104.5	7.5	7.0
23	Mn–Si–Al–Ce–B–V	207	–	–	–	7.5	–	4.0
24	Mn–Si	410	266.0	237.5	133.0	103.0	12.5	–
25	Mn–Si	411	172.5	100.5	72.5	–	–	–
26	Mn–Si	412	308.0	232.0	–	185.0	10.5	–
27	Mn–Si	413	152.0	66.5	56.0	35.0	–	–
28	Mn–Si–Al–Ce–V	432	18.5	3.5	–	4.5	–	–
29	Mn–Si–Ce–Al–Zr–Cr	433	82.0	4.5	–	4.5	–	–
30	Mn–Si–Ce–Al–V–Cr	434	28.5	6.0	–	5.0	–	–
31	Mn–Si–Ce–Al–Zr–B–Cr	435	36.0	5.5	–	3.5	–	–
32	Mn–Si–Ce–Al–Zr–V–P–Cr	436	53.5	13.0	–	15.0	–	–
33	Mn–Si–Ce–Al–Zr–V–B–Cr	437	28.0	5.0	–	5.0	–	–
34	Mn–Si–Ce–Al–Zr–V–Cr	438	2.0	3.5	–	3.0	–	–
35	Mn–Si–Al–Ce–V	458	5.0	5.0	–	3.0	–	–
36	Mn–Si–Al–Ce–Zr–V	459	26.5	4.5	–	7.0	–	–
37	Mn–Si–Ce–Al–Zr–V–Cr	460	11.0	3.0	–	4.0	–	–
38	Mn–Si–Ce–Al–Zr–Cr	505	3.0	3.0	–	3.5	–	–
39	Mn–Si–Ce–Al–Zr–V–Cr	506	13.0	4.5	–	9.5	–	–
40	Mn–Si–Ce–Al–Zr–V–B–Cr	507	–	46.0	–	20.5	–	–
41	Mn–Si–Ce–Al–Mo	530	–	–	–	216.5	171.0	103.5
42	Mn–Si–Ce–Al	531	–	–	149.0	170.0	46.0	9.5
43	Mn–Si	597	150.5	106.5	59.5	17.5	–	–
44	Mn–Si	598	157.5	72.5	67.0	25.0	–	–
45	Mn–Si–Ce–Al–Cr	718	–	–	–	108.5	73.5	60.0
46	Mn–Si–Ce–Al–Cr	727	–	–	–	–	11.5	16.5
47	Mn–Si–Ce–B	728	–	203.5	194.0	–	–	187.0
48	Mn–Si–Ce–Al–Cr	881	–	–	–	95.0	207.5	9.5
49	Mn–Si–Ce–B	882	–	–	–	156.0	–	143.5
50	Mn–Si–Ce–Al	883	–	–	201.5	105.0	6.0	–
51	Mn–Si–Ce–B	894	–	–	–	208.0	22.0	8.5
52	Mn–Si–Ce–Al	895	–	–	–	108.5	-	165.5
53	Mn–Si–Ce–B	896	–	–	–	103.5	52.0	76.5
54	Mn–Si–Ce	127-2	–	103.5	–	96.5	74.5	75.0

$$\Delta = \begin{vmatrix} n & \sum x_1 \cdots & \sum x_p \\ \sum x_1 & \sum x_1^2 \cdots & \sum x_1 x_p \\ \cdots & \cdots \cdots & \cdots \\ \sum x_p & \sum x_1 x_p \cdots & \sum x_p x_p \end{vmatrix}.$$

The data of observations and coefficients of multiple regression equation can be presented in the form of the following matrices:

$$Y = \begin{pmatrix} y_1 \\ y_2 \\ \cdots \\ y_n \end{pmatrix}, X = \begin{pmatrix} 1 & x_{11} & x_{12} & \cdots & x_{1m} \\ 1 & x_{21} & x_{22} & \cdots & x_{2m} \\ \cdots & \cdots & \cdots & \cdots & \cdots \\ 1 & x_{n1} & x_{n2} & \cdots & x_{nm} \end{pmatrix},$$

$$b = \begin{pmatrix} b_0 \\ b_1 \\ \cdots \\ b_m \end{pmatrix}, \quad e = \begin{pmatrix} e_1 \\ e_2 \\ \cdots \\ e_n \end{pmatrix}.$$

The formula of the coefficients of multiple linear regression in the matrix form is as follows:

$$b = (X^T X)^{-1} X^T Y,$$

where X^T is the matrix which is transposed to matrix X; $(X^T X)^{-1}$ is the matrix inverted to matrix $X^T X$.

Solving this equation, we obtain column-matrix b, the elements of which are exactly the coefficients of the equation of multiple linear regression.

An important index of the constructed model quality is the coefficient of determination or approximation confidence value which determines the level of prediction accuracy. This index is a statistical measure, consistency which allows establishing the extent to which the regression equation corresponds to the real data.

The coefficient of determination R^2 is the square of the correlation coefficient (Pearson coefficient) [5, 6]:

$$R = \frac{\sum \left(x_i - \bar{x}\right)\left(y_i - \bar{y}\right)}{\sqrt{\sum \left(x_i - \bar{x}\right)^2 \sum \left(y_i - \bar{y}\right)^2}},$$

where x_i is the value of variable X; y_1 is the value of variable Y; $\overline{x}$ is the arithmetic mean for variable X; $\overline{y}$ is the arithmetic mean for variable Y.

The coefficient of determination varies in the range from 0 to 1. If it is equal to zero, it means that the connection between the regression model variables is absent, and simple mean value may just as well used instead of it for evaluation of the initial variable value. Contrarily, if the coefficient of determination is equal to 1, it corresponds to an ideal model, when all the points of observation are located exactly on the regression line, i.e. the sum of squares of their deviation is equal to 0.

In practice, if the coefficient of determination is close to a unity, it shows that the model works well (has a high significance), and if it is close to zero, it means that the input variable poorly determines the behaviour of the output variable, i.e., there is no linear dependence between them. Evidently, such a model will have a low efficiency.

Depending on the level of the coefficient of determination, the models are usually divided into three groups:

- at $0.8 < R^2 < 1$ we obtain a model of good quality;
- at $0.5 < R^2 < 0.8$ — the model will be of acceptable quality;

at $0 > R^2 < 0.5$ – its quality will be poor.

Also at construction of a regression model, it is possible to assess the influence (contribution) of each predictor variable on the values of a dependent variable, and in some cases to essentially reduce the number of independent variables.

An important parameter at testing the statistic hypothesis is *p*-value [7–9]. The *p*-value is usually equal to the probability of a random quantity with this distribution taking a value, which is not smaller than the actual value of test statistics, and which is expressed by a number from 0 to 1. It should be determined whether the obtained experimental result is random. A result with *p*-value equal to the level of significance or below it, is considered significant. This is usually denoted as follows: $p \leq 0.05$.

In the case of a regression model, such a method as stepwise regression is quite well-established. Stepwise regression is a method to construct a model by adding or removing predictor variables. There are several approaches to performance of stepwise regression: forward step regression and backward step regression. At forward step regression the equations first contain no predictors. Then they are added one by one. In backward step regression first all the predictors are included into the regression equation, and then they are removed from the equation in turn.

Construction of mathematical models «composition-properties» for experimental samples of base material of steels and overheated zone at ESW. We will show construction of mathematical models of the dependence of mechanical properties on the composition of base material of the studied steels, as well as for the overheated zone at ESW of the studied steels after high-temperature tempering in the case of a model of *KCU* impact toughness at the temperature of –40 °C.

We will perform the following actions: First, we remove from experimental data for 55 experimental melts those, for which KCU_{-40} values are absent: 598, 153, 597, 412, 413.

When a matrix for 49 experimental steels was used (Table 4), a regression model of a poor quality was obtained, as the values of the coefficient of determination were below 0.5, namely $R^2 = 0.44$.

Having analyzed the diagram of comparison of the experimental and predicted data, we remove another 12 melts (Nos 458, 438, 165, 411, 37, 206, 33, 156, 410, 432, 881, 25), as the predicted (calculated) KCU_{-40} values for these experimental melts differ markedly from the general trend. We will obtain a matrix from 37 variants of steels (Table 5, Figure 1). And the regression model of a good quality was constructed exactly on this matrix ($R^2 = 0.84$):

$$KCU_{-40} = 556.89 - 2726.72\,\mathrm{C} + 2788.66\,\mathrm{B} - 375.29\,\mathrm{Al} + 134.424\,\mathrm{Ce} - 45.61\,\mathrm{Cr} - 28.27\,\mathrm{Mn} - 219.65\,\mathrm{Ni} + 45.25\,\mathrm{P} - 1790.66\,\mathrm{S} - 97.17\,\mathrm{Si} - 616.70\,\mathrm{V} - 345.55\,\mathrm{Zr}.$$

For a reduced model with a smaller number of independent variables (chemical elements) we will remove those elements which do not have any significant influence on impact toughness value at the tem-

Table 4. Correspondence of experimental melt number to melt number in the matrix

Melt number	1	2	3	4	5	6	7	8	9	10	11	12	13	14	15
Experimental melt number	458	437	438	177	436	506	163	164	165	411	460	167	434	205	505
Melt number	16	17	18	19	20	21	22	23	24	25	26	27	28	29	30
Experimental melt number	459	37	26	507	433	156	20	206	727	207	100	435	33	127-2	82
Melt number	31	32	33	34	35	36	37	38	39	40	41	42	43	44	45
Experimental melt number	718	38	99	133	728	203	152	882	157	410	895	531	432	896	883
Melt number	46	47	48	49											
Experimental melt number	881	894	530	25											

Table 5. Correspondence of experimental melt number to melt number

Melt number	1	2	3	4	5	6	7	8	9	10	11	12	13	14	15
Experimental melt number	437	177	436	506	163	164	460	167	434	205	505	459	26	507	433

Melt number	16	17	18	19	20	21	22	23	24	25	25	27	28	29	30
Experimental melt number	156	20	727	207	100	435	127-2	82	718	38	99	133	728	203	882

Melt number	31	32	33	34	35	36	37
Experimental melt number	157	895	531	896	883	894	530

Table 6. Correspondence of experimental melt number to melt number

Melt number	1	2	3	4	5	6	7	8	9	10	11	12	13	14	15
Experimental melt number	177	436	506	164	460	434	505	459	507	433	156	20	207	100	127

Melt number	16	17	18	19	20	21	22	23	24	25	25	27	28
Experimental melt number	82	718	38	99	133	728	203	882	157	895	531	896	530

perature of –40 °C. At forward direction of stepwise regression a good model was obtained ($R^2 = 0.81$):

$$KCU_{-40} = 549.75 - 302.65\ \mathrm{Al} - 3101.87\ \mathrm{Cr} - 44.03\ \mathrm{Cr} - 193.84\ \mathrm{Ni} - 2639.73\ \mathrm{S} - 117.84\ \mathrm{Si} - 569{,}92\ \mathrm{V}.$$

In this model the following independent variables are removed: Mn, P, Ce, B, Zr. Figure 1 shows the results.

Once can see from Figure 1 that some calculated KCU_{-40} values for steels Nos 437, 163, 167, 205, 26, 727, 435, 883, 894 by the constructed model differ essentially from the specified line, so we remove them from the matrix of experimental values (correspondence of experimental melts and melt numbers from Figure 1, are given in Table 6).

We obtain a matrix from 28 observations (experimental steels), and construct a regression model with coefficient of determination $R^2 = 0.91$:

$$KCU_{-40} = 568.53 - 2732.83\ \mathrm{C} - 28.39\ \mathrm{Mn} - 119.04\ \mathrm{Si} - 1638.39\ \mathrm{S} + 38.66\ \mathrm{P} - 47.68\ \mathrm{Cr} - 205.94\ \mathrm{Ni} - 619.31\ \mathrm{V} - 382.65\ \mathrm{Al} + 75.81\ \mathrm{Ce} + 2442.99\ \mathrm{B} - 439.62\ \mathrm{Zr}.$$

We can also reduce the number of chemical elements (we remove P, Ce, B, Zr) which are used in the model, considering that p-value ≤ 0.05 for these elements. As a result, we obtain the following regression model:

$$KCU_{-40} = 584.09 - 326.71\ \mathrm{Al} - 2647.62\ \mathrm{Cr} - 53.90\ \mathrm{Cr} - 32.83\ \mathrm{Mn} - 192.39\ \mathrm{Ni} - 2099.09\ \mathrm{Si} - 132.66\ \mathrm{Si} - 542.62\ \mathrm{V}$$

and coefficient of determination $R^2 = 0.91$.

Calculation shows that in this case there are several KCU_{-40} values which differ markedly from the general line. We remove them: melts Nos 177, 506, 436, 164, 460.

We derive the following model:

$$KCU_{-40} = 573.52 - 362.89\ \mathrm{Al} - 2020.46\ \mathrm{Cr} - 64.01\ \mathrm{Cr} - 56.39\ \mathrm{Mn} - 276.03\ \mathrm{Ni} - 117.59\ \mathrm{Si} - 108.44\ \mathrm{Si} - 662.79\ \mathrm{V}.$$

The coefficient of determination is $R^2 = 0.90$ that points to a good quality of the model.

Comparison of experimental and calculated KCU_{-40} values is given in Figure 2.

Thus, processing the entire amount of experimental data for 55 experimental melts of steels designed for ESW (Table 1) resulted in construction of a mathematical models «Chemical composition – Mechanical properties» (impact toughness, yield limit, ultimate strength, relative elongation and reduction in area) based on application of the method of multiple (multifactorial) regression.

All the plotted models are characterized by a high value of the coefficient of determination ($R^2 > 0.8$) that defines a sufficient level of prediction accuracy.

The method of stepwise regression was used to create a reduced mathematical model, and p-value was applied to reduce the number of independent variables.

In the derived regression models such elements as Mn, Cr, Zr have the greatest impact on the mechanical properties of base material (steel), designed for ESW. Si, P, Al, V, Ce have less influence on the mechanical

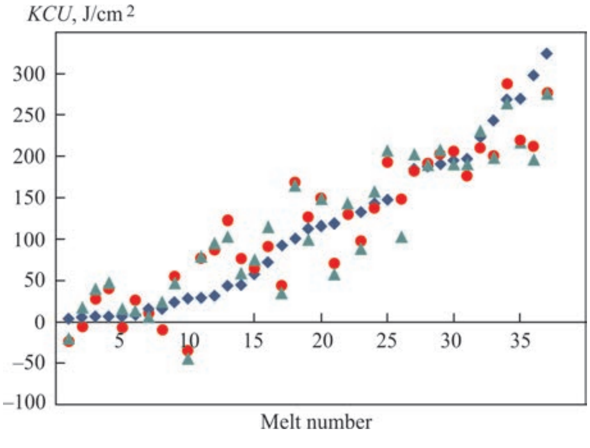

Figure 1. Comparison of experimental (♦) and calculated KCU_{-40} values for 37 experimental melts ($R^2 = 0.84$), taking into account all the independent parameters (●) and for a reduced number of independent parameters (▲) ($R^2 = 0.81$)

Table 7. Chemical composition of steels for testing

Steel	C	Mn	Si	S	P	Cr	Ni	V	Al	Ce	B	Zr	Mo	Cu
09KhG2SYuCh	0.09	2.00	0.45	0.01	0.015	1	0	0	0.05	0.004	0	0	–	–
10Kh2GNM	0.10	1.10	0.33	0.022	0.023	2.15	0.52	0	0.052	0	0	0	–	–
10Kh2GNMA-A	0.10	0.96	0.27	0.007	0.006	2.09	0.2	0	0.005	0	0	0	–	–
12KhM	0.12	0.55	0.30	0.018	0.016	0.5	0.25	0	0.055	0	0	0	0.5	0.2
10KhG2MCh	0.10	2.10	0.30	0.018	0.016	1.2	0.15	0	0.055	0.018	0	0	–	–
10Kh2GM	0.10	0.93	0.30	0.018	0.016	2.3	0.66	0	0.055	0	0	0	–	–

properties. Ni, S and B have practically no impact in the plotted models.

For the overheated zone at ESW, such chemical elements (by increase of the degree of impact) as P, C, Mn, S, Cr, Ni, V, B have the greatest influence on the metal mechanical properties, while the impact of Si, Ce and Zr elements is small, judging from the regression models.

Testing the constructed mathematical models. Developed models (regression equations) for determination of mechanical properties of steels designed for ESW, were tested on 6 steel grades (Table 7), for which the respective experimental data are available [7–9].

For the overheated zone (of the HAZ, after tempering, without normalizing) a comparison was performed with experimental data of the calculation results by the complete and reduced models for KCV_{+20}, KCV_{-60}, KCU_{-60}, KCU_{-70}.

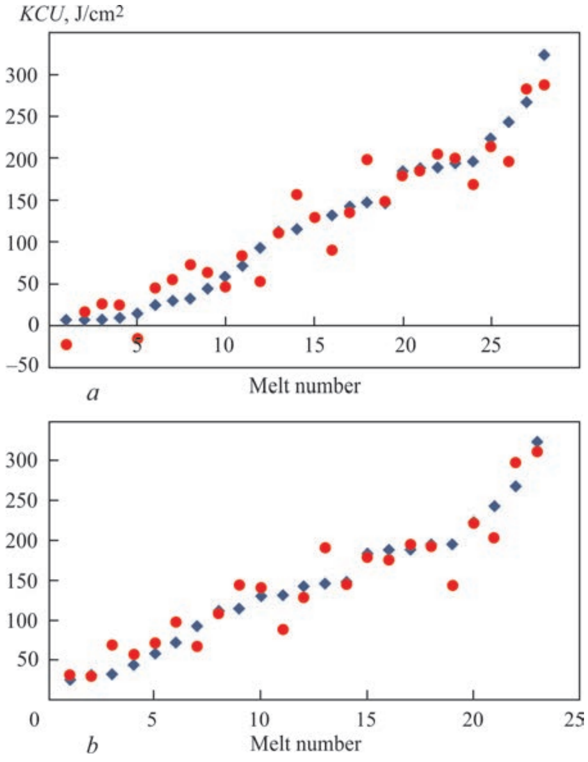

Figure 2. Comparison of experimental (♦) and calculated (●) KCU_{-40} values: *a* — for 28 experimental steels and full number of independent parameters ($R^2 = 0.91$); *b* — for 23 experimental steels and reduced number of independent parameters ($R^2 = 0.90$)

The constructed models for prediction of KCV_{-60}, KCU_{-60}, KCU_{-70} yield quite adequate values, compared to experimental data. The models for KCV_{+20} give considerably underestimated values (Table 8).

For the base metal (after normalizing or hardening and tempering), a comparison of experimental data and results of calculation by the complete and reduced models was performed for KCU_{-40}, KCU_{-60}, yield limit σ_y, ultimate strength σ_t, relative elongation δ and reduction in area ψ.

The models for prediction of KCU_{-40} yield adequate values, models for KCU_{-60} in some cases give underestimated, but rather close values, compared to experimental data (Table 9). The models for yield limit σ_y, ultimate strength σ_t, and reduction in area ψ yield adequate values, and models for relative elongation δ give somewhat overestimated values.

In order to improve (increase the accuracy) of the models, the procedure of construction of the regression models was repeated, based on an expanded scope of experimental data from 55 experimental melts of low-alloy steels up to 61 steel by complimenting the experimental data [7–9]. It allowed to noticeably improve the calculated and experimental data (Tables 10–12), for impact toughness *KCV* (at –70 °C) in the overheated zone, for impact tough-

Table 8. Overheated zone (HAZ, after tempering, without normalizing)

Steel	KCV_{+20}^{1}, J/cm²		KCV_{-60}^{2}, J/cm²	
	Model	Exp.	Model	Exp.
09KhG2SYuCh	111	–	79	–
10Kh2GNM	61	142–161	36	12–21
10Kh2GNMA-A	79	181–209	82	16–102
12KhM	197	–	1	–
10KhG2MCh	73	–	87	102–137
10Kh2GM	54	–	10	44–60
09KhG2SYuCh	95	87–163	20	13–25
10Kh2GNM	141	100–120	106	–
10Kh2GNMA-A	94	86–90	27	–
12KhM	111	–	171	–
10KhG2MCh	118	–	–53	–
10Kh2GM	137	–	109	–

Notes. [1]Models give underestimated values and require optimizing. [2]Models yield adequate values.

Table 9. Base metal (after normalizing or hardening and tempering)

Steel	$KCU_{-40}{}^1$, J/cm^2			$KCU_{-60}{}^2$, J/cm^2		
	Model	Red. model	Exp.	Model	Red. model	Exp.
09KhG2SYuCh	120.31	133.71	–	117.05	115.88	84–188
10Kh2GNM	139.17	124.78	94–192	131.98	87.64	100–107
10Kh2GNMA-A	97.30	155.57	155–163	94.73	89.11	117–142
12KhM	341.69	356.50	–	93.09	128.16	–
10KhG2MCh	104.88	113.12	–	120.27	110.97	–
10Kh2GM	155.01	130.20	–	144.46	83.95	–
	$\sigma_y{}^2$, MPa			$\sigma_t{}^3$, MPa		
Steel	Model	Red. model	Exp.	Model	Red. model	Exp.
09KhG2SYuCh	341.01	347.55	360–395	490.04	492.99	560–600
10Kh2GNM	469.92	458.26	460–503	585.36	570.97	565–610
10Kh2GNMA-A	433.56	433.90	460–503	576.89	581.01	565–610
12KhM	318.00	323.13	318	491.00	491.00	491
10KhG2MCh	459.32	455.76	467–550	591.47	588.24	662–689
10Kh2GM	470.30	448.05	437–487	588.90	569.29	578–604
Steel	δ^4. %			ψ^3. %		
	Model	Red. model	Exp.	Model	Red. model	Exp.
09KhG2SYuCh	30.13	30.79	22–28	71.255	70.64	49–80
10Kh2GNM	24.46	23.68	15–20	64.080	66.62	55–67
10Kh2GNMA-A	23.60	23.85	15–20	64.494	65.57	55–67
12KhM	23.00	26.73	23	67.599	69.82	–
10KhG2MCh	25.04	26.44	20–26	68.368	68.49	–
10Kh2GM	25.38	23.24	21–26.6	64.067	66.41	–

Note. [1]Models give individual underestimated values and require optimizing. [2]Models give close values. [3]Models yield adequate values. [4]Models yield close but somewhat overestimated values and require optimizing.

ness *KCU* (at –40 °C) of the base metal and for relative elongation δ (base metal).

Thus, the most rational way to improve the constructed models consists in expanding the experimental data base.

We give the final form of the mathematical models, taking into account their optimization.

Impact toughness (KCV and *KCU*) *for the overheated zone* (*of the HAZ after tempering without normalizing):*

$KCV_{+20} = 181.00 - 819.95\,C + 4.88\,Mn + 83.96\,Si + 173.93\,P - 605.91\,S - 20.15\,Cr - 199.17\,V - 364.01\,Al - 520.19\,Ce + 3931.41\,B - 430.55\,Zr + 248.89\,Mo$;

$KCV_{-60} = 2.52 + 132.21\,C + 14.62\,Mn - 70.94\,Si + 953.25\,S + 81.4186\,P + 50.21\,Cr - 205.99\,Ni - 541.64\,V + 74.96\,Al + 544.33\,Ce + 11371.4\,B + 4090.56\,Zr$;

$KCU_{-60} = 23.47 + 364.76\,C + 17.48\,Mn - 11.36\,Si + 912.35\,S + 1047.04\,P - 2.91\,Cr +$

Table 10. Comparison of model results for KCV_{-70} for overheated zone (HAZ, after tempering, without normalizing)

Steel	First variant[1]		Improved variant[2]	
	Model	Exp.	Model	Exp.
09KhG2SYuCh	520	13–25	20	13–25
10Kh2GNM	829	–	106	–
10Kh2GNMA-A	1167	–	27	–
12KhM	350	–	171	–
10KhG2MCh	521	–	–53	–
10Kh2GM	802	–	109	–

Notes. [1]Models yield underestimated values and require optimizing. [2]Models yield adequate values.

Table 11. Comparison of model results for KCU_{-40} for base metal (after normalizing or hardening and tempering)

Steel	First variant[1]			Improved variant[2]		
	Model	Red. model	Exp.	Model	Red. Model	Exp.
09KhG2SYuCh	130	147	–	120.31	133.71	–
10Kh2GNM	0	–29	94–192	139.17	124.78	94–192
10Kh2GNMA-A	82	96	155–163	97.30	155.57	155–163
12KhM	64	144	–	341.69	356.50	–
10KhG2MCh	63	80	–	104.88	113.12	–
10Kh2GM	0	–65	–	155.01	130.20	–

Notes. [1]Models yield underestimated values and require optimizing. [2]Models yield adequate values, but require optimizing in some cases.

Table 12. Comparison of model results for relative elongation δ for base metal (after normalizing or hardening and tempering)

Steel	First variant[1]			Improved variant[2]		
	Model	Red. model	Exp.	Model	Red. Model	Exp.
09KhG2SYuCh	28	33	22–28	30.13	30.79	22–28
10Kh2GNM	28	31	15–20	24.46	23.68	15–20
10Kh2GNMA-A	29	31	15–20	23.60	23.85	15–20
12KhM	34	34	23	23.00	26.73	23
10KhG2MCh	26	33	20–26	25.04	26.44	20–26
10Kh2GM	29	30	21–26.6	25.38	23.24	21–26.6

Notes. [1]Models yield underestimated values and require optimizing. [2]Models yield adequate values.

$+ 77.23\,\mathrm{Ni} - 131.98\,\mathrm{V} - 244.51\,\mathrm{Al} - 147.71\,\mathrm{Ce} + 254.12\,\mathrm{B} - 610.58\,\mathrm{Zr}$;

$KCU_{-70} = 258.07 - 665.22\,\mathrm{C} - 89.57\,\mathrm{Mn} + 226.31\,\mathrm{Si} - 6870.75\,\mathrm{S} + 8430.52\,\mathrm{P} - 95.4137\,\mathrm{Cr} + 319.41\,\mathrm{Ni} - 1259.5\,\mathrm{Al} + 18087.1\,\mathrm{B}$.

Base metal after normalizing or hardening and tempering:

1. Yield limit:

$\sigma_y = 127.77 + 982.92\,\mathrm{C} + 74.1854\,\mathrm{Mn} - 50.5011\,\mathrm{Si} + 1075.06\,\mathrm{S} + 202.153\,\mathrm{P} + 62.2906\,\mathrm{Cr} + 62.5862\,\mathrm{Ni} + 28.1904\,\mathrm{V} - 304.692\,\mathrm{Al} + 147.574\,\mathrm{Ce} + 8400.33\,\mathrm{B} + 933.64\,\mathrm{Zr} - 76.7431\,\mathrm{Mo} + 161.927\,\mathrm{Cu}$.

2. Ultimate strength:

$\sigma_t = 376.487 + 197.733\,\mathrm{B36} + 74.597\,\mathrm{C36} - 80.1669\,\mathrm{Si} - 51.6227\,\mathrm{S} + 170.066\,\mathrm{P} + 58.1997\,\mathrm{Cr} + 52.2038\,\mathrm{Ni} - 62.8523\,\mathrm{V} - 414.44\,\mathrm{Al} + 330.174\,\mathrm{Ce} + 5461.85\,\mathrm{B} + 991.499\,\mathrm{Zr} - 130.434\,\mathrm{Mo} + 589.374\,\mathrm{Cu}$.

3. Relative elongation:

$\delta = 38.5232 - 46.8034\,\mathrm{B36} - 2.12612\,\mathrm{C36} - 0.0489085\,\mathrm{Si} - 75.0961\,\mathrm{S} - 4.93551\,\mathrm{P} - 4.2477\,\mathrm{Cr} + 5.78539\,\mathrm{Ni} + 7.0119\,\mathrm{V} + 16.5739\,\mathrm{Al} + 23.3941\,\mathrm{Ce} - 278.698\,\mathrm{B} - 64.3938\,\mathrm{Zr} - 26.2339\,\mathrm{Mo} + 27.954\,\mathrm{Cu}$.

4. Reduction in area:

$\psi = 77.5019 - 87.8572\,\mathrm{B36} + 2.24134\,\mathrm{C36} - 7.31298\,\mathrm{Si} - 86.2487\,\mathrm{S} - 11.5188\,\mathrm{P} - 1.78764\,\mathrm{Cr} - 0.778479\,\mathrm{Ni} + 39.5843\,\mathrm{V} + 33.1262\,\mathrm{Al} - 38.0401\,\mathrm{Ce} + 110.365\,\mathrm{B} - 129.132\,\mathrm{Zr} + 5.208\,\mathrm{Mo}$.

Conclusions

1. Proceeding from earlier results of experimental studies we constructed mathematical models of the dependence of mechanical properties of silicon-manganese steels, designed for electroslag welding and characterized by high brittle fracture resistance in the HAZ, as well as of the overheated zones, on the chemical composition of these steels.

2. The mathematical models were constructed with application of the method of multiple linear regression. Mathematical models were constructed for a set of mechanical properties of base metal: impact toughness for temperatures of (+20, –40, –60, –70 °C), yield limit, ultimate strength, relative elongation and reduction in area. For the overheated zone at electroslag welding mathematical models were constructed for impact toughness (*KCU* and *KCV*) for temperatures of +20, –60, –70 °C.

3. Initial validation of the constructed models was performed. Its results showed that the constructed models for the overheated zone (of the HAZ, after tempering, without normalizing) and for the base metal (after normalizing or hardening and tempering), mostly give quite adequate values, compared to experimental data, but, in some cases, they essentially underestimate or overestimate the mechanical property values. It is shown that the most rational way to improve the constructed models consists in expanding the experimental data base.

1. Egorova, S.V. (1988) *Alloying of steel and its weldability in electroslag welding without subsequent normalizing.* Kiev, AS USSR, National Welding Committee [in Russian].
2. Demidenko, E.Z. (1981) *Linear and nonlinear regression*. Moscow, Finansy i Statistika [in Russian].
3. Seber, G. (1980) *Linear regression analysis. Moscow*, Mir [in Russian].
4. Linnik, Yu.V. (1962) *Least squares method and fundamentals of mathematical-statistical theory of processing observations.* 2nd Ed. Moscow, Fizmatgiz [in Russian].
5. Gmurman, V.E. (2004) *Probability theory and mathematical statistics.* In: Manual for higher education inst. 10th Ed. Moscow, Vysshaya Shkola [in Russian].
6. Eliseeva, I.I., Yuzbashev, M.M. (2002) *General theory of statistics:* Manual. 4th Ed. Ed. by I.I. Eliseeva. Moscow, Finansy i Statistika [in Russian].
7. Egorova, S.V., Sterenbogen, Yu.A., Yurchishin, A.V. et al. (1980) New structural steels not requiring normalizing after electroslag welding. *Avtomatich. Svarka*, 332(**11**), 44–46, 59 [in Russian].
8. Egorova, S.V., Yurchishin, A.V., Solina, E.N. et al. (1991) Cold-resistant steel 09KhG2SYuCh of higher strength for pressure vessels. *Ibid*., 465(**12**), 37–42 [in Russian].
9. Egorova, S.V., Lyashchuk, Yu.S., Krendelyova, A.I. et al. (1992) Investigation of resistance to temper brittleness of welded joints produced by electroslag welding without normalizing. *Ibid*., 467(**2**), 8–10 [in Russian].

Received 10.12.2020